DIFFERENTIAL CROSS SECTIONS FOR THE ELASTIC SCATTERING OF NEGATIVE KAONS BY PROTONS

by John Harvey

A thesis submitted to the University of Southampton for the degree of Doctor of Philosophy

May 1979

UNIVERSITY OF SOUTHAMPTON

ABSTRACT

FACULTY OF SCIENCE

PHYSICS

Doctor of Philosophy

DIFFERENTIAL CROSS SECTIONS FOR THE ELASTIC SCATTERING OF NEGATIVE KAONS BY PROTONS

by John Harvey

Elastic K^- proton differential cross sections have been measured at twentythree different momenta in the range 1000 MeV/c to 1933 MeV/c. The experiment was motivated by the need to resolve ambiguities in the partial wave analysis of $\bar{K}N$ scattering.

Proportional chambers were used to measure the trajectories of kaons in the incident beam and spark chambers to locate particles emerging from a liquid hydrogen target. The experiment used a magnetic spectrometer for the forward scattered particle and thus covered a wide angular range.

Preliminary results have been obtained at five of the momenta. Agreement with existing differential cross section measurements is good apart from a small discrepancy in the normalisation. External checks on the normalisation confirm this discrepancy and have been used to renormalise the data.

CONTENTS

CHAPTER 1

Introduction to the $\bar{K}N$ System

The study of meson-nucleon scattering has made an important contribution to the investigation of the properties of the strong interaction.

At low energies (ie. less than 3 Gev) the total cross sections for these reactions exhibit peaks which are attributed to the formation of short lived resonant states with well defined quantum numbers. The position of the peak gives the mass of the resonance and its width is related through the uncertainty principle to the lifetime.

The spin and parity of the resonances may be determined from experiments measuring the angular distribution of the decay products. The results of these experiments are usually subjected to a partial wave analysis , the resonances being identified from the behaviour of the solutions. In this way it has been shown that a single peak in the total cross section may correspond to several resonances, each in a different angular momentum - parity state.

At present there is no fundamental theory giving a quantitative description of these phenomena. However the

strong interaction is associated with various internal symmetries which lead to the conservation of other quantum numbers eg. isospin and strangeness. The classification of strongly interacting particles and resonances according to these quantities has brought a qualitative understanding to the spectrum of hadron states. In this respect the quark model , based on unitary symmetry, has been particularly successful.

These topics, as they relate to the $\bar{K}N$ system, will be briefly discussed in this chapter.

1.1 Total Cross Sections

The conservation of isospin in strong interactions leads to relations between the total cross sections for particles belonging to the same multiplet. In the $\bar{K}N$ system they are related to the two independent cross sections σ_o and σ_1 in the pure isospin states I=0 ,1 :

$$\sigma_t(K^- p) = 1/2\ (\sigma_o + \sigma_1)$$

$$\sigma_t(K^- n) = \sigma_t(\bar{K}^o p) = \sigma_1$$

$$\sigma_t(\bar{K}^o n) = 1/2\ (\sigma_1 - \sigma_o)$$

The independent cross sections can therefore be determined from measurements of at least two reactions. The study of K^- p scattering is straightforward since both K^- beams and proton targets are available, whereas measurement of a second reaction presents difficulties

since neither $\bar{K}^o$ beams nor neutron targets exist. The free neutron cross section can, however, be extracted with limited accuracy from hydrogen and deuterium data.

Accurate K^- total cross section measurements have been made in hydrogen and deuterium for kaon laboratory momenta from 400 Mev/c to 3.4 Gev/c.[1] The I=0 and I=1 total cross sections have been derived from these results and are shown in Figure 1.1. They exhibit structures which decrease in amplitude as the momentum increases, clearly demonstrating the strong resonance behaviour of the $\bar{K}N$ system.

It is usually assumed that the shape of a resonance as a function of the total energy , E, in the centre of mass is describable by a Breit-Wigner formula:

$$\sigma_t = \frac{4\pi}{k^2} \frac{(J+1/2)x}{(\varepsilon^2+1)} \quad ; \quad \varepsilon = 2 \frac{(E_r - E)}{\Gamma}$$

where k , is the centre of mass momentum

J, E_r, Γ ,are the angular momentum, resonant energy, and full width at half height respectively, of the resonace

x , is the elasticity ie. $x = \Gamma_{el}/\Gamma_t$

At resonance:

$$\sigma_r = \frac{4\pi}{k^2} (J+1/2)x$$

The many peaks observed in the pure isospin total

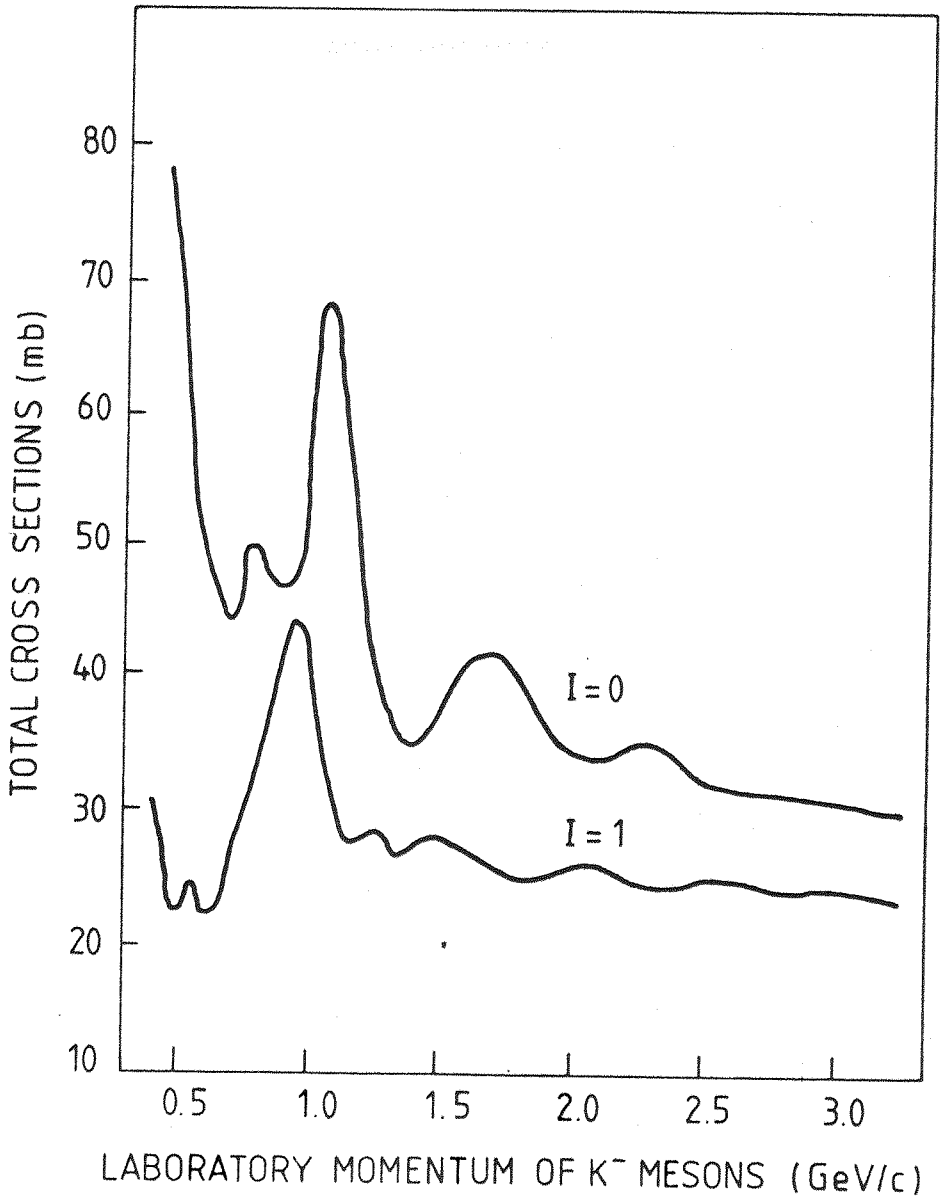

FIG. 1.1. Total cross sections for the I = 0 and I = 1 isotopic spin states, for the $\bar{K}N$ system.

cross sections can be fitted by a superposition of Breit-Wigner formulae plus a smooth background. From such fits precise values for E_r, Γ and σ_r are obtained. The value of σ_r gives a good indication of the spin of a resonance, providing the background and elasticity can be reliably estimated.

However this analysis is misleading since a single bump in the total cross section does not necessarily signify a unique resonant state. To obtain an accurate picture of the resonance spectrum it is necessary to examine the partial waves that contribute to the scattering. The information required to complete this analysis is obtained from experiments measuring the angular distributon of the decay products of the resonance ie. the so-called 'formation' experiments.

1.2 Partial Wave Analysis

In the past, the partial wave analysis of kaon - nucleon elastic scattering experiments has been one of the most fruitful means of discovery of new resonances. In this section the formalism of the partial wave decomposition will be summarised and methods of finding a solution discussed.

For the interaction of spinless particles the principle of conservation of angular momentum applies to

the orbital angular momentum ,l. It is therefore convenient to represent the initial and final states by a sum of angular momentum eigenfunctions, each term in the sum being called a partial wave. The effect of the interaction is to alter the phase and amplitude of those waves taking part in the reaction. The behaviour of the phase shifts as a function of energy then yields valuable information concerning the form of the interaction.

Thus the scattering amplitude can be written in the form :

$$f(\theta) = \frac{1}{k} \sum_{l=0}^{\infty} (2l+1)\, T_l\, P_l(\cos\theta)$$

where $P_l(\cos\theta)$ is the lth Legendre Polynomial

T_l are the partial wave amplitudes :

$$T_l = \frac{\eta_l \exp(2i\delta_l) - 1}{2i}$$

where δ_l are the phase shifts of the scattered waves with respect to the incoming wave

and η_l are the absorption coefficients ($0 \leqslant \eta_l \leqslant 1$).

For the scattering of a spinless meson from a nucleon (spin 1/2) every partial wave has two possible values of total spin ,j ie. $j = l \pm 1/2$. Since j is conserved it is necessary to define a phase shift in each state : δ_{l+} , δ_{l-} . Also, during a collision it is possible for the spin orientation of the nucleon to

change, in which case the scattering amplitude is written :

$$f(\theta) = g(\theta) + i\,\underline{\sigma}.\underline{n}\,h(\theta)$$

where $g(\theta)$ and $h(\theta)$ are the spin non-flip and spin flip amplitudes respectively.

$\underline{\sigma}$ is the Pauli spin matrix

$\underline{n}$ is the normal to the scattering plane.

$g(\theta)$ and $h(\theta)$ are expressed in terms of the partial wave scattering amplitudes $T_l^{\pm}$, for $j=l+1/2$, by :

$$g(\theta) = \frac{1}{k}\sum_l [(l+1)T_l^{+} + lT_l^{-}]\,P_l(\cos\theta)$$

$$h(\theta) = \frac{1}{k}\sum_l [T_l^{+} - T_l^{-}]\,P_l^{1}(\cos\theta)$$

where $P_l^{1}(\cos\theta)$ are the first associated Legendre Polynomials.

The problem of partial wave analysis lies in determining the partial wave amplitudes from the data. The information to be obtained from scattering experiments may be summarised as follows.

The differential cross section for the scattering of kaons from an unpolarised target is related to $g(\theta)$ and $h(\theta)$ by :

$$\frac{d\sigma}{d\Omega}(\theta) = |g(\theta)|^2 + |h(\theta)|^2$$

The transverse polarization, $P(\theta)$, of the recoil proton is given by :

$$P(\theta) = 2\,\frac{\mathrm{Im}\,[g(\theta)h(\theta)^*]}{|g(\theta)|^2 + |h(\theta)|^2}$$

and may be determined by re-scattering the proton off a second target. Alternatively, this information may be obtained by measuring the asymmetry produced in a single scattering from a target containing polarised protons.

It is also possible to consider experiments in which the initial proton is polarized and the final proton polarization is measured. This introduces two more parameters (R and A) which are related to $\mathrm{Re}[g(\theta)h(\theta)^*]$ and $|g(\theta)|^2 - |h(\theta)|^2$. Measurement of the differential cross section and the three polarization quantities (P,A,R) therefore determine the moduli of the amplitudes and the phase angle between them.

There exists, however,an overall phase ambiguity since the observables are invariant when $g(\theta)$ and $h(\theta)$ are multiplied by the same phase factor eg. $\exp(i\Phi(\cos\theta))$. In the forward direction ($\cos\theta=1$) this absolute phase can be determined by use of the optical theorem :

$$\mathrm{Im}\; g(0) = \frac{k}{4\pi}\,\sigma_t$$

and forward dispersion relations to determine the $g(0)$. Away from this region the angular dependece of $\Phi(\cos\theta)$ is not known. The problem can be resolved in pratice by

considering only a finite number of partial waves, motivated by the finite range of the interaction. With such an assumption the partial wave amplitudes and their relative phases can be determined.

In practice further ambiguities exist due to the lack of polarization data. For example, the differential cross section is invariant under the change of parity of all the states involved (Minami ambiguity):

$$T^{-}_{l+1} \rightarrow T^{+}_{l} \; ; \; T^{+}_{l-1} \rightarrow T^{-}_{l}$$

This ambiguity can be resolved by a measurement of P which has opposite sign for the two solutions. The more general ambiguity:

$$T^{-}_{l+1} \rightarrow -T^{+*}_{l} \; ; \; T^{+}_{l-1} \rightarrow -T^{-*}_{l}$$

leaves both $d\sigma/d\Omega$ and P unaltered but is resolved by a measurement of either A or R.

These ambiguities can be eliminated by imposing smooth energy behaviour on the partial wave amplitudes. There are two distinct methods of imposing smoothness. In the "energy dependent" approach some energy dependent parameterisation of the amplitudes is assumed which is generally taken to be a sum of a rapidly varying resonance contribution and a slowly varying background. This method is particularly suitable when the data are of poor quality and at widely spaced values of momentum.

When the data are closely spaced in energy and cover the differential cross section and polarisations then the energy independent method is used. In this approach a number of solutions are found at each energy, each solution corresponding to a satisfactory fit of the partial wave amplitudes to the data. A unique set of phase shifts can then be found by imposing continuity with energy, providing a single solution exists at one energy at least. If the multiplicity of solutions away from the starting point becomes too great, it is necessary to use extra information. In the $\bar{K}N$ system several resonance states are well established and so solutions only containing these need be considered.

The variation of the phase shifts with energy is governed by the nature of the scattering potential. If the potential is positive, corresponding to a repulsive force, then the phase shift is negative, i.e. the scattered wave is advanced in time with respect to the unscattered wave. The rate of decrease of the phase shifts with energy is, therefore limited by causality (Wigner condition). For an attractive potential the phase shift is positive, i.e. the scattered wave is retarded with respect to the unscattered wave. If the time delay is sufficient the intermediate state is interpreted as a resonance, or unstable particle, which lives briefly before decaying into the final state. The

energy dependence of the elastic partial wave amplitude near the resonance energy can be derived using a Taylor series expansion:

$$T_l = \frac{1/2\ \Gamma_{el}}{(E_r - E) - \frac{1}{2} i \Gamma_t}$$

This is the simplest version of a Breit-Wigner form for a resonance of mass E_r with full width at half height of Γ_t.

When plotted as a function of energy on an Argand diagram T_l moves rapidly in an anti-clockwise direction as the energy is increased (Fig. 1.2a). A purely elastic amplitude lies on the unitary circle, the phase passing through 90° at the resonant energy (E_r).

Above the inelastic threshold similar behaviour is observed for the elastic amplitude, although the circle it describes lies completely within the unitary circle (Fig.1.2b). The resonance position is associated with a minimum in the absorption coefficient and with a phase of 0 or $\pi/2$ according to the magnitude of Γ_{el}/Γ_t. In this case a further complication is introduced, however, due to the possibility of non resonant (background) scattering occuring together with resonance scattering in the same partial wave. Providing the background varies slowly with energy the resonant amplitude still describes a circle although this may be

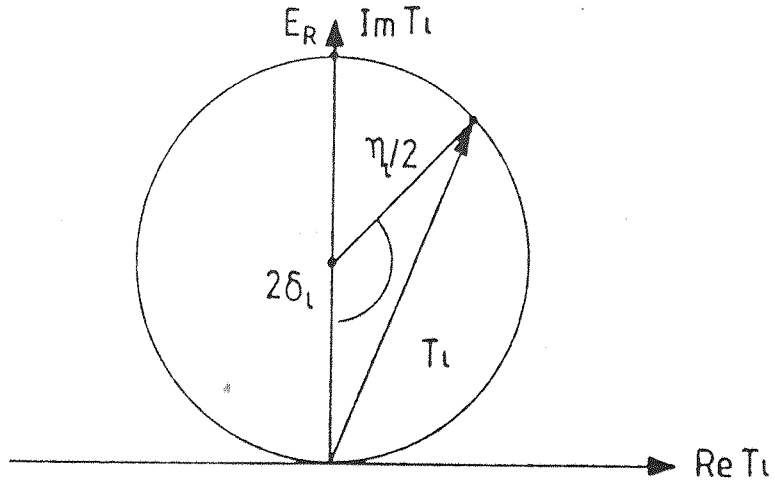

(a) An elastic resonance

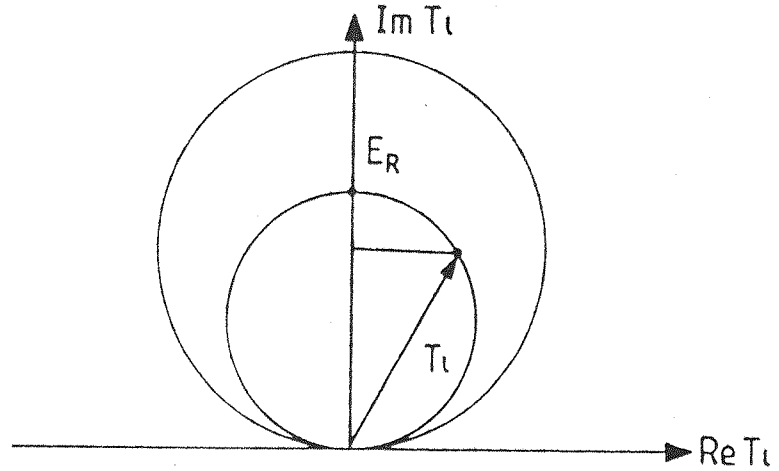

(b) An inelastic resonance with $\Gamma_{el} > 1/2\ \Gamma_{tot}$

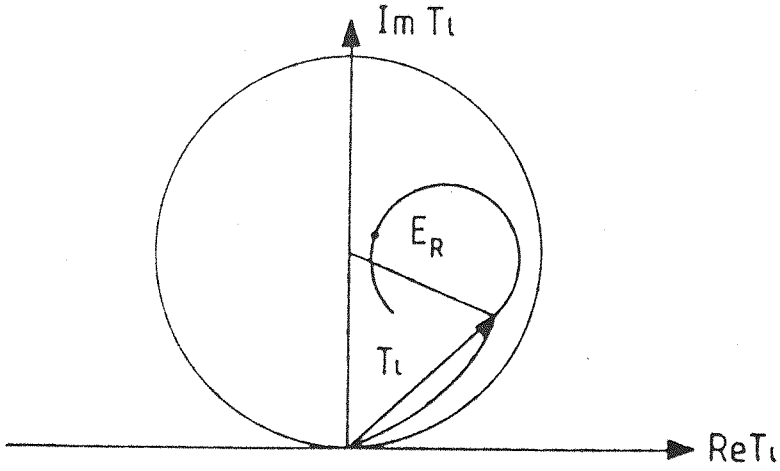

(c) An inelastic resonance in the presence of an attractive, non-resonant background

FIG. 1.2. Behaviour of resonant amplitudes in the Argand diagram.

displaced to any region within the unitary circle and rotated by an arbitary phase (Fig. 1.2c). For these cases it is difficult to establish the parameters of the resonance since different assumptions on the background yield considerably different values. The quantity which is usually examined is the speed, $|dT/dE|$, which has a maximum at the resonance energy for a Breit-Wigner form.

1.3 Review Of $\bar{K}N$ Data And Analyses

The technique of partial wave analysis has been applied to the study of resonance formation processes in both the πN and $\bar{K}N$ systems. However there is a large difference in quality between our understanding of these systems for the following reasons.

a) As already mentioned the different reactions in each system are related through conservation of isospin and more than one process must be measured to determine the independent cross sections. In πN they can be determined from studies of the $\pi^{\pm}$ proton elastic and charge exchange reactions, which are relatively simple to measure. In the elastic $\bar{K}N$ system they are given by:

$$\sigma_1 = \sigma(K^- n \to K^- n) = \sigma(\bar{K}^0 p \to \bar{K}^0 p)$$

$$\sigma_0 = 2\sigma(K^- p \to K^- p) + 2\sigma(K^- p \to \bar{K}^0 n) - \sigma_1$$

However $K^- n$ scattering requires a deuteron target and $\bar{K}^0$

scattering must be studied with K_L^o beams. In both cases the reaction of interest can be extracted only with limited accuracy.

b) In πN inelastic channels are only weakly coupled and analysis of the elastic channel seems to be sufficient for a study of the resonance spectrum. In contrast, $\bar{K}N$ analyses are complicated by two body inelastic channels ($\Lambda\pi, \Sigma\pi, \ldots\ldots$) that couple strongly at all energies above threshold. Data from all these processes are desirable so that a coupled analysis can use unitarity to constrain the partial wave solutions.

In practice, the inelastic channels have been studied extensively with the bubble chamber and the quality of the data compares favourably with that from the elastic channel. In particular there is the advantage that polarizations can be obtained directly from the decay asymmetries of the hyperons. Experiments using wire chambers are particularly suited to making high statistics measurements of simple reactions and recent contributions have had an important bearing on the $\bar{K}N$ channel.

The energy region covered by the present experiment has been investigated by several previous experiments as indicated in Figure 1.3. However, the following brief review shows the existing analyses to be

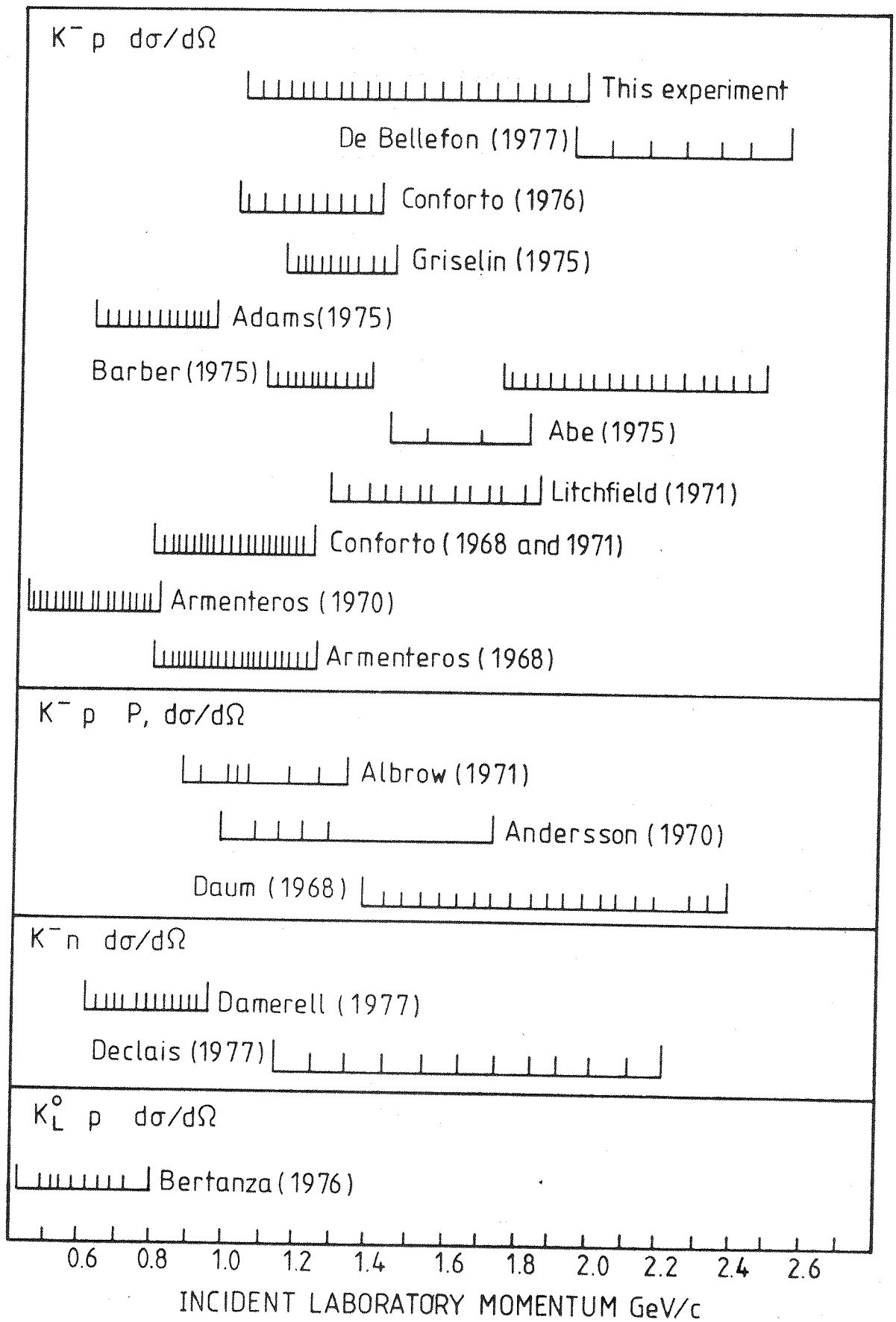

FIG.1.3. $\bar{K}N$ Scattering Experiments

inconclusive in many respects and this has motivated the need for new high statistics data.

Prior to 1974 the most accurate measurements came from a study of K^- proton collisions in the 81cm Saclay bubble chamber at the CERN proton synchrotron. Data were taken at intervals of 20 MeV/c in two exposures covering the momentum regions 0.44 to 0.8 GeV/c [2] and 0.78 to 1.22 GeV/c [3] . A total of about 5,000 events were analysed at each momentum from which angular distributions were determined for the $\bar{K}N$, $\Sigma\pi$ and $\Lambda\pi$ channels. In addition polarizations were obtained from the decay of the Λ Σ^+ and Σ° hyperons.

In the elastic channel accurate asymmetry measurements were only obtained after the introduction of polarized targets. At CERN, data were reported from a series of measurements covering the momentum range 0.8 to 2.4 GeV/c [4] . In this experiment the scattered particles were detected by arrays of scintillation counters, elastic events being identified from the angular correlation between the kaon and recoil proton. Consequently the angular region covered by the experiment was limited in the forward direction ($\cos\theta^* < 0.8$) due to the loss of slow, large angle protons in the target assembly.

These measurements motivated the first attempts at

a combined analysis of the KN, $\Sigma\pi$ and $\Lambda\pi$ channels using a multi-channel formalism.[5] In the analysis of Langebin and Wagner an energy independent approach was adopted. However the amplitudes were discontinuous in their energy dependence and the well established resonances were poorly represented. In view of these results more recent analyses have consistently used the energy dependent approach.

Above 1.2 Gev/c cross sections and angular distributons from a bubble chamber measurement of the reactions $K^-p \rightarrow K^-p$ and $K^-p \rightarrow \bar{K}^0n$ were used in an energy dependent analysis of the $\bar{K}N$ channel.[6] The data, taken at 50 Mev/c intervals in the range 1.26 to 1.84 GeV/c, were combined with polarization measurements and total cross sections in the same energy interval. The partial wave parameterization included Breit-Wigner forms for the well established resonances $\Sigma(2030)$ and $\Lambda(2100)$. Structures were observed in several partial waves although the evidence for their existence was marginal. Subsquently this analysis was repeated but incorporating new bubble chamber data in the same energy region.[7] A good fit to the experimental data was obtained without the requirement of these marginal resonances.[8]

More recently the precision of data in the elastic channel has been improved by several contributions from

spark chamber experiments. At low energies, 0.61 to 0.94 GeV/c, K^- scattering in both hydrogen and deuterium has been studied using sonic spark chambers and elastic differential cross sections presented for K^-p[9] and K^-n[10] reactions. This experiment included a magnetic spectrometer for the forward particle and hence covered a wide angular range. At higher energies two experiments using correlation type arrangements of wire spark chambers have measured the elastic $K\bar{p}$ reaction. At the Rutherford Laboratory measurements were taken at closely spaced momentum intervals within the regions 1.1 to 1.4 GeV/c[11] and 1.7 to 2.4 GeV/c.[12] The statistical precision of each data point was approximately 13%. At Argonne 20,000 events were obtained at each of four momenta from within the region 1.4 to 1.9 GeV/c.[13] The statistical errors were typically 7%.

Of the recent bubble chamber studies, high statistics measurements of all final states of $K\bar{p}$ collisions have been reported in the momentum region 0.96 to 1.36 GeV/c.[14] Also reactions involving K°_L beams have been measured at low energies (300 MeV/c to 800 MeV/c) and have provided useful data on the pure isospin reaction, $K^\circ_L p \rightarrow \pi^+\Sigma^\circ$[15]. These measurements were included with other data, selected from the existing high statistics experiments, in a coupled analysis of $\bar{K}N, \Sigma\pi$ and $\Lambda\pi$ channels.[16] This remains the most complete

analysis performed to date, the energy range 0.3 to 2.0 GeV/c being wider than any previous study. By imposing simple energy continuity and consistent resonance structure in each channel a unique solution was obtained.

At present several single channel analyses exist which are noteworthy since they include high precision data not incorporated in the above analysis. Results from a high statistics bubble chamber experiment covering the region 1.9 to 2.5 GeV/c, indicated fine structure in the bumps seen at 2250 MeV and 2300 MeV in the total cross section.[17] These structures were observed in separate analyses of the $K\bar{N}$, $\Sigma\pi$ and $\Lambda\omega$ channels. In addition, results from an electronic counter measurement of the K^-n elastic reaction have been subjected to an energy dependent analysis in combination with existing data in the same energy range, 1.1 to 2.0 GeV/c.[18] These results are particularly welcome in that they constitute the first extensive collection of data in the pure isospin 1 state. The partial wave solutions were found to differ from existing analyses, only in the form of the background amplitudes; the main features of the resonance structures were retained.

The present situation regarding the $\bar{K}N$ partial waves in the energy interval covered by the present

TABLE 1.1. Status of S = -1 Baryon States[a)]

Resonance	Partial Wave LI 2J	Status
Λ (1800)	P01	xx
Λ (1800)	G09	x
Λ (1815)	F05	xxxx
Λ (1830)	D05	xxxx
Λ (1860)	P03	xxx
Λ (1870)	S01	xxx
Λ (2010)		xx
Λ (2020)	F07	x
Λ (2100)	G07	xxxx
Σ (1840)	P13	x
Σ (1880)	P11	xx
Σ (1915)	F15	xxxx
Σ (1940)	D13	xxx
Σ (2000)	S11	x
Σ (2030)	F17	xxxx
Σ (2070)	F15	x
Σ (2080)	P13	xx
Σ (2100)	G17	x
Σ (2250)		xxxx

xxxx Good, clear and unmistakable
xxx Good, but in need of clarification
xx Needs confirmation
x Weak

a) Taken from the Review of Particle Properties, 1978

experiment is summarised in Table 1.1. Though there is broad agreement on the properties of the well established resonances, those recently proposed have small couplings to their two body decay channels and are therefore poorly determined; several states are still to be confirmed. New high statistics data over this energy region will clearly be extremely valuable in helping to resolve these descrepancies.

1.4 Classification Scheme

As already mentioned the strongly interacting particles can be grouped into isotopic spin multiplets. These multiplets may be regarded as representations of the special unitary group SU(2), with the members of a multiplet being linked by rotations in isotopic spin space. The symmetry is broken by Coulomb effects which give rise to small mass differences between the charged partners of a multiplet.

The classification scheme can be extended by considering the grouping of these multiplets into 'super-multiplets'. A succesful hypothesis is found by considering the collections of particles having the same spin, parity and baryon number but different strangeness and isospin. The particles then fall into representations of the higher symmetry SU(3). It is

apparant from the relatively large mass differences that this symmetry is much less accurate than the approximation of isospin conservation. However the masses are close enough to suggest that in the absence of some moderately strong symmetry breaking mechanism the members of the 'super-multiplets' would be degenerate.

The baryons are observed to occupy decuplets($\underline{10}$), octets($\underline{8}$) and singlets ($\underline{1}$) (Fig 1.4a), while the mesons occupy octets ($\underline{8}$) and singlets ($\underline{1}$) (Fig 1.4b). The quark model provides a formalism for the construction of these groupings from the basic representations $\underline{3}$ and $\bar{\underline{3}}$. The quantum numbers of the three quarks forming the $\underline{3}$ representation are given in Table 1.2.

Table 1.2 Quark quantum numbers

Quark	Q	B	I	Y
u	2/3	1/3	1/2	1/3
d	-1/3	1/3	-1/2	1/3
s	-1/3	1/3	0	-2/3

The higher multiplets are found by decomposing direct products of these representations into irreducible constituents. Hence in group theory

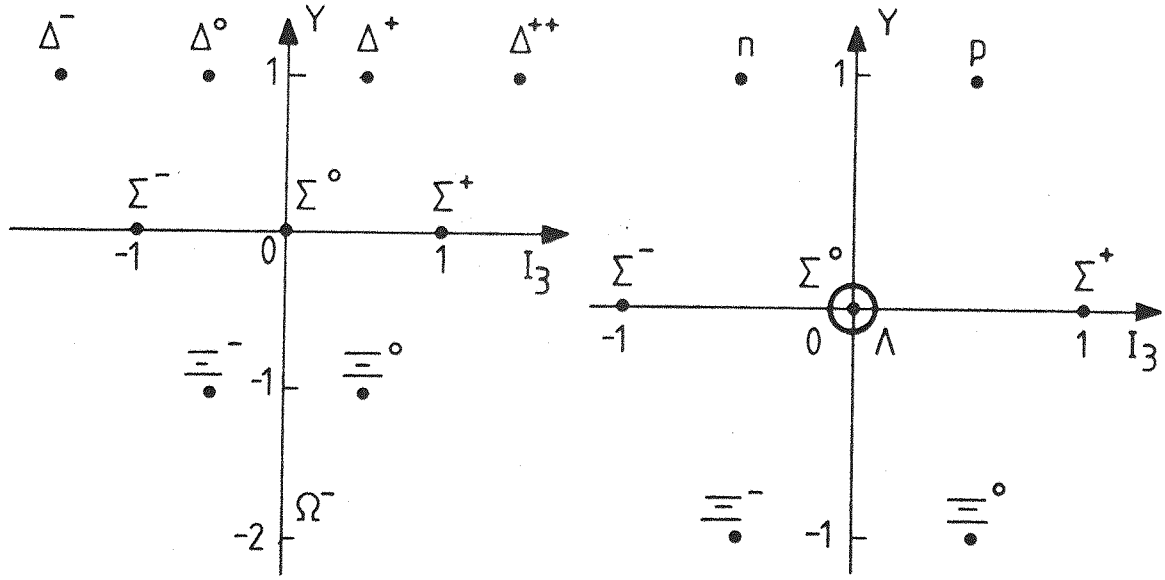

(a). The observed decuplet ($J^P = 3/2^+$) and octet ($J^P = 1/2^+$) of baryon states

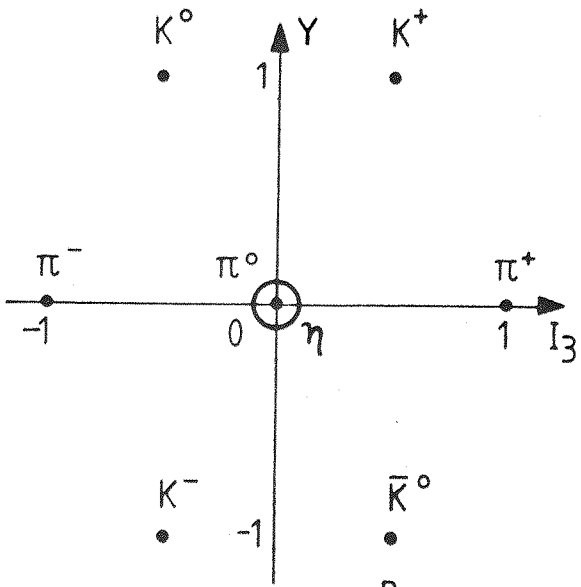

(b). The observed octet ($J^P = 0^-$) of meson states

FIG. 1.4. Supermultiplets of particles of the same spin, parity and baryon number

notation:

$$\underline{3} \times \underline{\bar{3}} = \underline{1} + \underline{8}$$

$$\underline{3} \times \underline{3} \times \underline{3} = \underline{1} + \underline{8} + \underline{8} + \underline{10}$$

These relations suggest that the baryon octet (1/2+) and decuplet(3/2+) be composed of three spin 1/2 particles (quarks), while the pseudoscalar and vector meson octets are made up from a quark-antiquark pair. Moreover the parity of a three fermion system is given by $(-1)^L$, where L is the orbital angular momentum, and for a fermion-antifermion system by $(-1)^{L+1}$. The lowest quark states correspond to L=0 producing positive parity baryons and negative parity mesons, as observed in practice.

The introduction of spin increases the number of possible quark states to six (ie. each quark can have spin up or spin down) and leads to a consideration of SU(6) symmetry. The result of combining three of these quarks is:

$$\underline{6} \times \underline{6} \times \underline{6} = \underline{56} + \underline{70} + \underline{70} + \underline{20}$$

The spin and unitary spin decompositions of these representations are:

$$\underline{56} = {}^4\underline{10} + {}^2\underline{8}$$

$$\underline{70} = {}^4\underline{8} + {}^2\underline{8} + {}^2\underline{10} + {}^2\underline{1}$$

$$\underline{20} = {}^2\underline{8} + {}^4\underline{1}$$

where the superscript is 2S+1, with S the quark spin. The 1/2+ octet and 3/2+ decuplet of baryons may now be easily accommodated in the $\underline{56}$ representation of SU(6).

The higher spin resonances can be interpreted as rotational excitations of the lowest lying quark states (ie SU(6)xO(3)). It is then found that the S and D wave negative parity resonances may all be assigned to a ($\underline{70}$:$L^P = 1^-$) representation. Similarly, at relatively higher masses, the P and F wave resonances can be assigned to a ($\underline{56}$:$L^P = 2^+$) multiplet.

The sucess of this model lies in its ability to accommodate all the well established resonances. Particles not belonging to these representations are called 'exotic' and so far no 'exotic' multiplets have definitely been observed. At present the spectrum of N^* and Δ resonances in the ($\underline{70}$,1^-) and ($\underline{56}$,2^+) multiplets is thought to be virtually complete, whereas for several predicted Σ and Λ states there are no experimental candidates.[19] In addition, the experimental status of several more Y^* resonances is poor and their assignment in the classification scheme only tentative. It is hoped that the results of this experiment will help to define the resonance states more precisely and hence clarify their assignment in the classification schemes.

CHAPTER 2

Experimental Method

The aim of the experiment was to measure the K^- proton elastic differential cross section with high precision and over a wide angular range. The design of the experiment was therefore directed towards these requirements.

2.1 Design Criteria

The experiment was performed by focusing a partially separated beam of kaons onto a target vessel containing liquid hydrogen. Trajectories were measured for both the incident kaon and the particles emerging from the target. These were used to determine scattering angles, from which elastic events were identified using kinematic constraints.

The range of scattering angles covered by the experiment depended on the arrangement of the detectors. Full coverage necessitated the use of two separate experimental modes. In the correlation mode (C), both scattered particles were detected. Elastic events were selected from the coplanarity of the measured tracks and the angular correlation between the reaction products. At small scattering angles; however, there was little

energy transferred to the target proton, which because of multiple scattering and energy loss did not produce a well defined trajectory. In addition, at backward angles the kaon had a high probability of decaying. For these regions, a magnetic spectrometer was used to determine the momentum of the forward particle. In this, the spectrometer mode (S), elastic scattering events were selected by momentum-angle correlation.

The total number of elastic events N_m, measured at a particular centre of mass scattering angle, θ^*, is related to the elastic differential cross section (Appendix 1) by:

$$N_m(\theta^*) = N_c\, 2\pi L_t\, \rho\, \frac{d\sigma}{d\Omega}(\theta^*) A(\theta^*) d\cos\theta^*$$

where ρ, represents the density of scattering centres (ie. protons) contained in a target of length L_t, and N_c the flux of kaons from which the scattered particles were removed. $A(\theta^*)$ is the acceptance of the apparatus, and is largely determined by the fraction of the scattering region covered by the detectors.

The statistical precision of the differential cross section measurement was optimised by using large detectors, capable of resolving the full flux of particles accepted into the experimental region.

2.2 K15A Beamline

The experiment took place at the Rutherford Laboratory using the 7GeV proton synchrotron NIMROD. Protons were extracted from the NIMROD ring, at peak energy, into the X3 beamline and focused onto a metal target. K15A was one of several beams derived from the secondary particles produced in this target. (PLATE 1)

The negatively charged component of the secondary beam was dominated by pions, the K^-/π^- production ratio being approximately 1%.[20] The flux of kaons was greatest in the momentum region 0.9 to 2.5 GeV/c; outside these limits the intensity fell rapidly. The function of the beamline, therefore, was to provide momentum dispersion to define a narrow momentum bite and velocity separation to reduce the background of unwanted particles. Since the decay length of the kaon is short (7m at 1 GeV/c), the length of the beamline was restricted as far as possible to preserve the kaon flux at the target. However, a 3-tank velocity separator was introduced, at the expense of overall length, to compensate for the small K^-/π^- ratio.

The layout of the K15A beam transport system is shown in Fig. 2.1 where the elements have been represented by analogy with their optical properties in the horizontal plane. The production of secondary

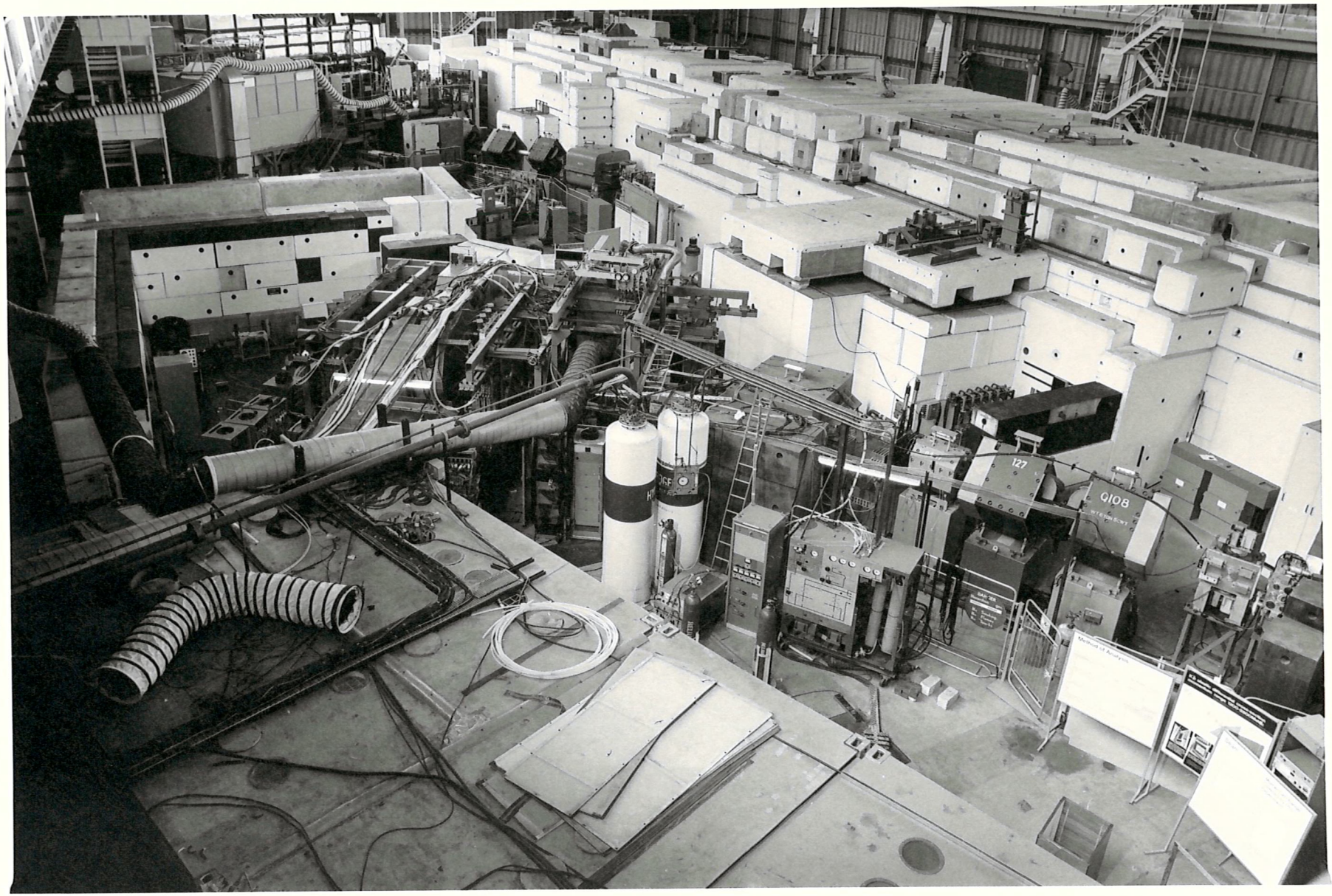

PLATE 1 View of the Experimental Area

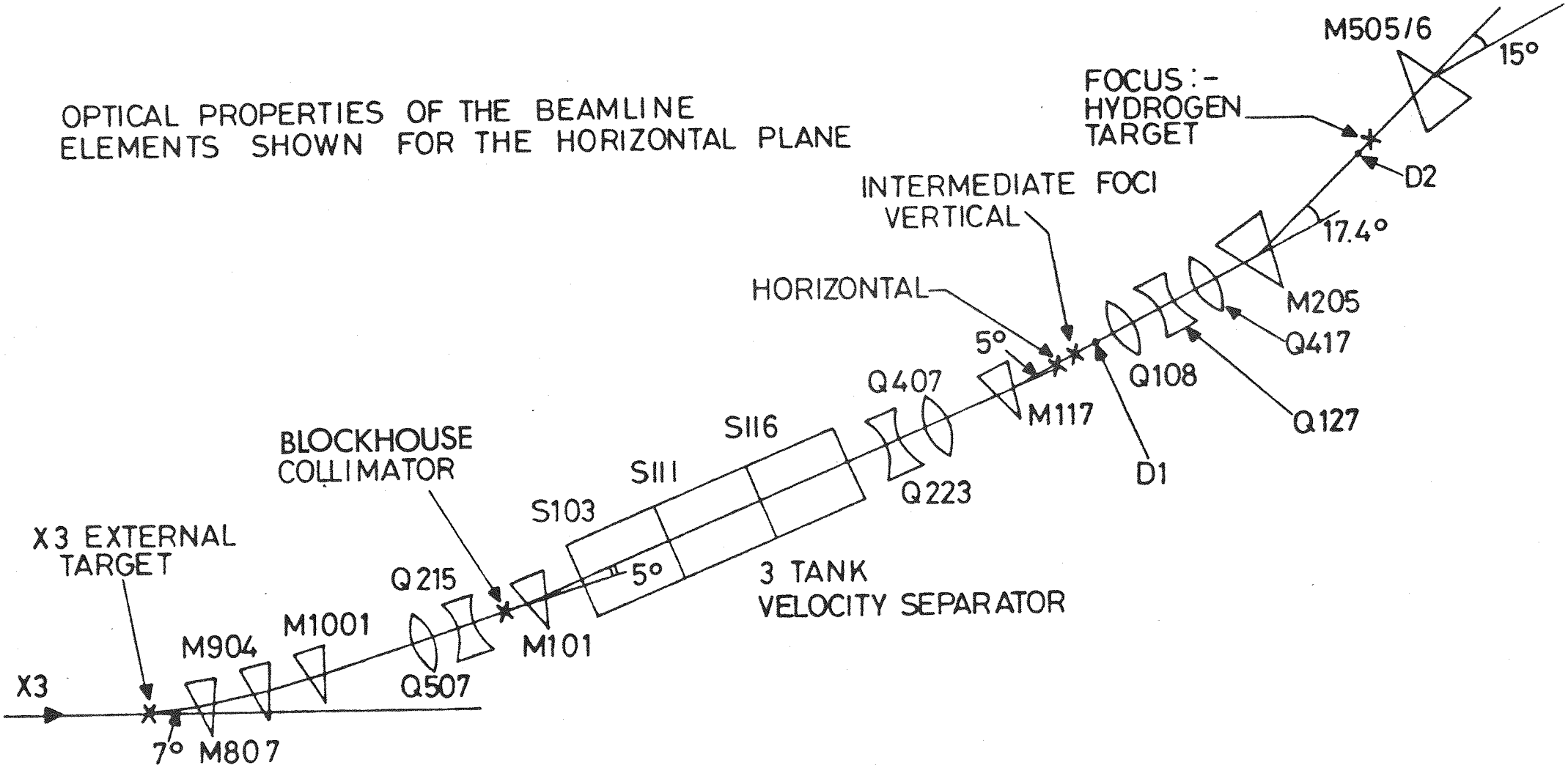

FIG.2.1 THE K15A BEAMLINE SHOWING THE BEAM TRANSPORT ELEMENTS

particles in long targets is peaked at small angles to the forward direction, because of reabsorption in the target, and so the first three septum magnets (M807, M904,M1001) were arranged to accept particles at 7° to the incident beam direction. The quadrupole magnets Q507 and Q215 formed a strong focusing doublet and produced a parallel beam for the separator. Each separator tank consisted of a combination of vertical electrostatic and horizontal magnetic fields. These were adjusted such that the required particles emerged undeviated. Unwanted particles suffered a nett deflection in the vertical plane. The Q223, Q407 doublet provided an intermediate focus, in both horizontal and vertical planes at the collimators. The vertical collimator intercepted those particles deflected by the separator. The M101 and M117 magnets provided momentum dispersion and thus enabled a narrow momentum bite to be selected by the horizontal collimator. The beam was then refocused at the hydrogen target by a quadruple triplet (Q108, Q127, Q417). The last bending magnet before the target, M205, was used in the momentum determination as well as providing momentum recombination of the beam.

The beam was transported to the intermediate focus in a vacuum pipe and helium bags were inserted in the remaining magnet apertures before the target. This reduced the multiple scattering and absorption of the

kaons.

For each beam momentum, the fields and field gradients required to focus the beam at the hydrogen target were determined using standard Rutherford Laboratory computer routines.[21] The operating currents corresponding to these fields were found from standard calibration curves. In this way, sets of beam element currents were calculated to span the momentum range 1.0 to 2.0 GeV/c in approximately 50 MeV/c intervals.

2.3 Beam Detectors

To optimise the statistical accuracy of the differential cross section measurement it was important to utilise the full flux of kaons accepted into the beamline. For this reason it was necessary for the beam detectors to have short resolution times. Scintillation counters and Cerenkov counters were used to measure the intensity of the kaon beam and multiwire proportional chambers recorded their trajectories. All these detectors were capable of resolving beam fluxes greater than 10^6 particles per second.

The arrangement of beam counters and wire proportional chambers is shown in Fig.2.2 . The beam was defined 'upstream' by the counter D1 and close to the

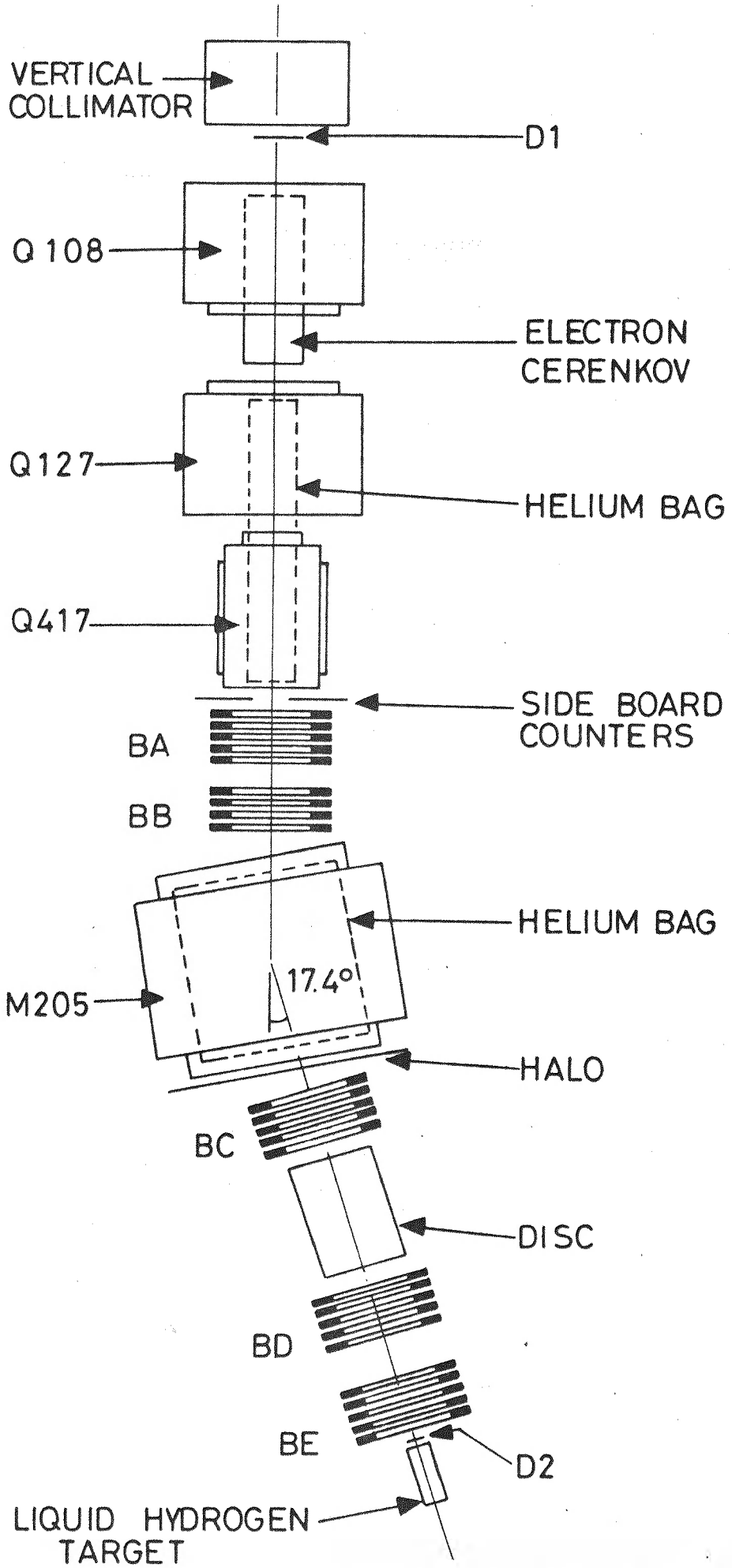

FIG. 2.2 BEAM DEFINING COUNTERS D1, D2, HALO AND WIRE PROPORTIONAL CHAMBERS BA. BB... BE

target by D2. The size and shape of these scintillators were chosen to match the profile of the beam (Fig. 2.3). The 'sideboard' (SB) and 'halo' (H) counters provided a veto to these particles passing outside the active area of the multiwire chambers.

The kaons were identified by a Differential Isochronous Self Collimating Cerenkov counter (DISC) which provided a method of differentiating between particles of different velocities (Fig. 2.4). Coherent radiation produced in the cell of the counter was reflected downstream by a spherical mirror to a perspex ring of triangular cross section, the axicon. This focused the light onto a ring of nine photomultiplier tubes through an annular slit ,the iris, in a diaphragm. The resolution of the counter was controlled by adjustment of the width of the iris. A range of Cerenkov angles, and hence velocities, could be accepted by moving the axicon parallel to the beam direction. Since the angle of Cerenkov light also depends on the refractive index of the radiating medium it was possible to cover a much larger range of velocities by interchanging cells.

Another feature of the beamline was a threshold Cerenkov counter (EC), which was used to veto electrons. It consisted of a metre long pipe containing Freon 12 at

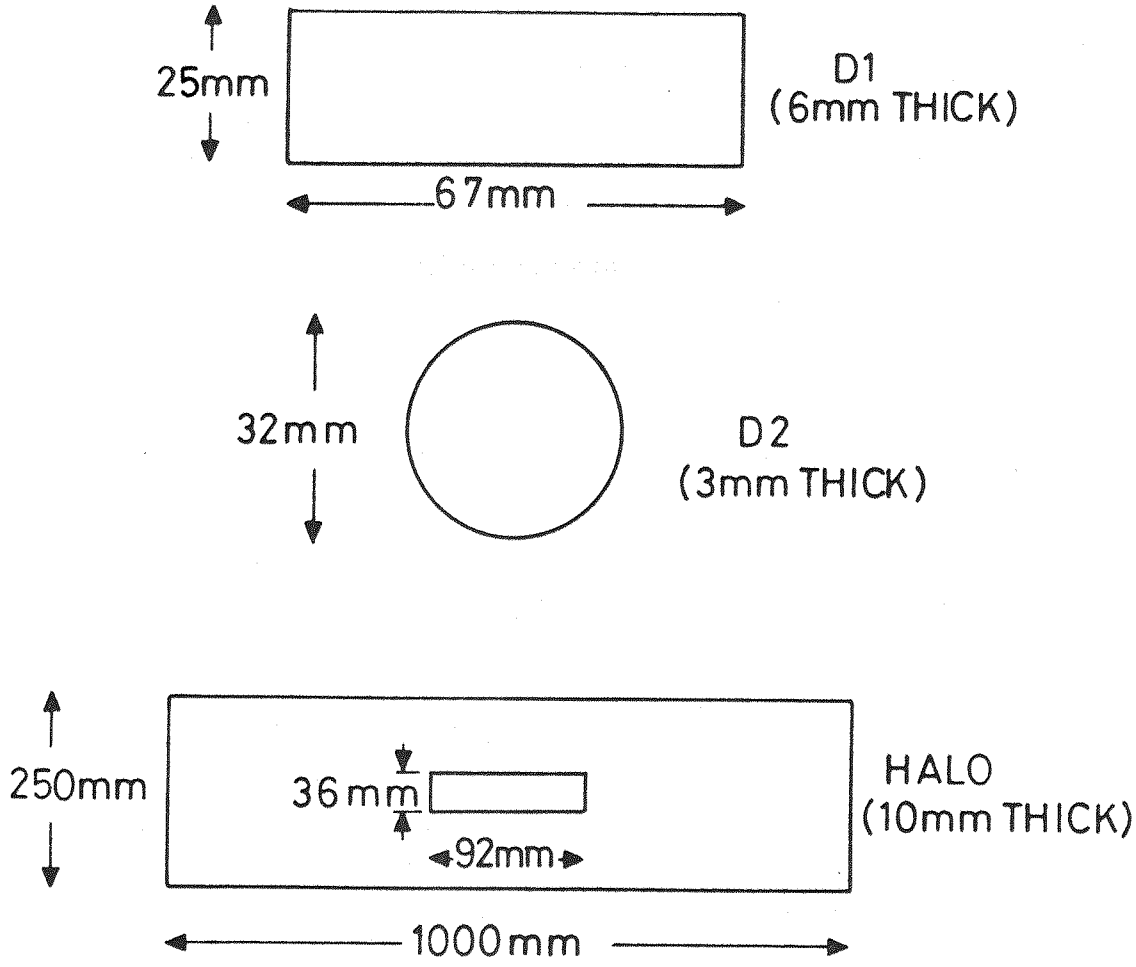

FIG. 2.3 DIMENSIONS OF THE BEAM DEFINING COUNTERS

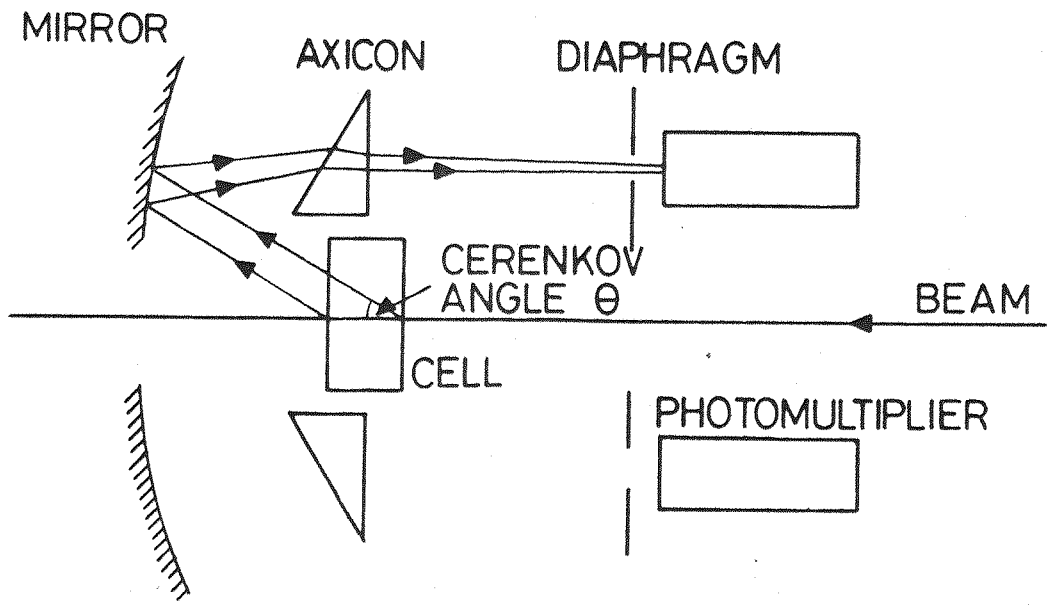

FIG. 2.4 OPTICAL ARRANGEMENT OF THE DISC ČERENKOV

atmospheric pressure as the radiating medium. Although this counter was operated throughout this experiment, it was primarily included for use with pion beams.

'CANDIDATES' for producing scattering events in the target were defined by the following coincidence:

$$CANDS = D1.D2.DISC.\ \overline{(H+SB)}.\overline{EC}$$

The proportional chambers were used to measure the momentum of the kaons, to record their trajectories into the target and to identify those scattered in the cell of the DISC counter. For this purpose they were positioned in the five groups, BA to BE (Fig.2.2). Each chamber was capable of measuring one coordinate, either horizontal (X) or vertical (Y), according to its orientation in the beamline. To optimise the track fitting they were arranged in each group according to the pattern XYXXY, except for BB which had only four chambers (XXXY). Fewer Y chambers were required since the M205 magnet deflected the beam only in the horizontal plane.

2.4 Scattered Particle Detectors

The scattered particle tracks were recorded by spark chambers, triggered by large arrays of scintillation counters (Fig.2.5). The individual

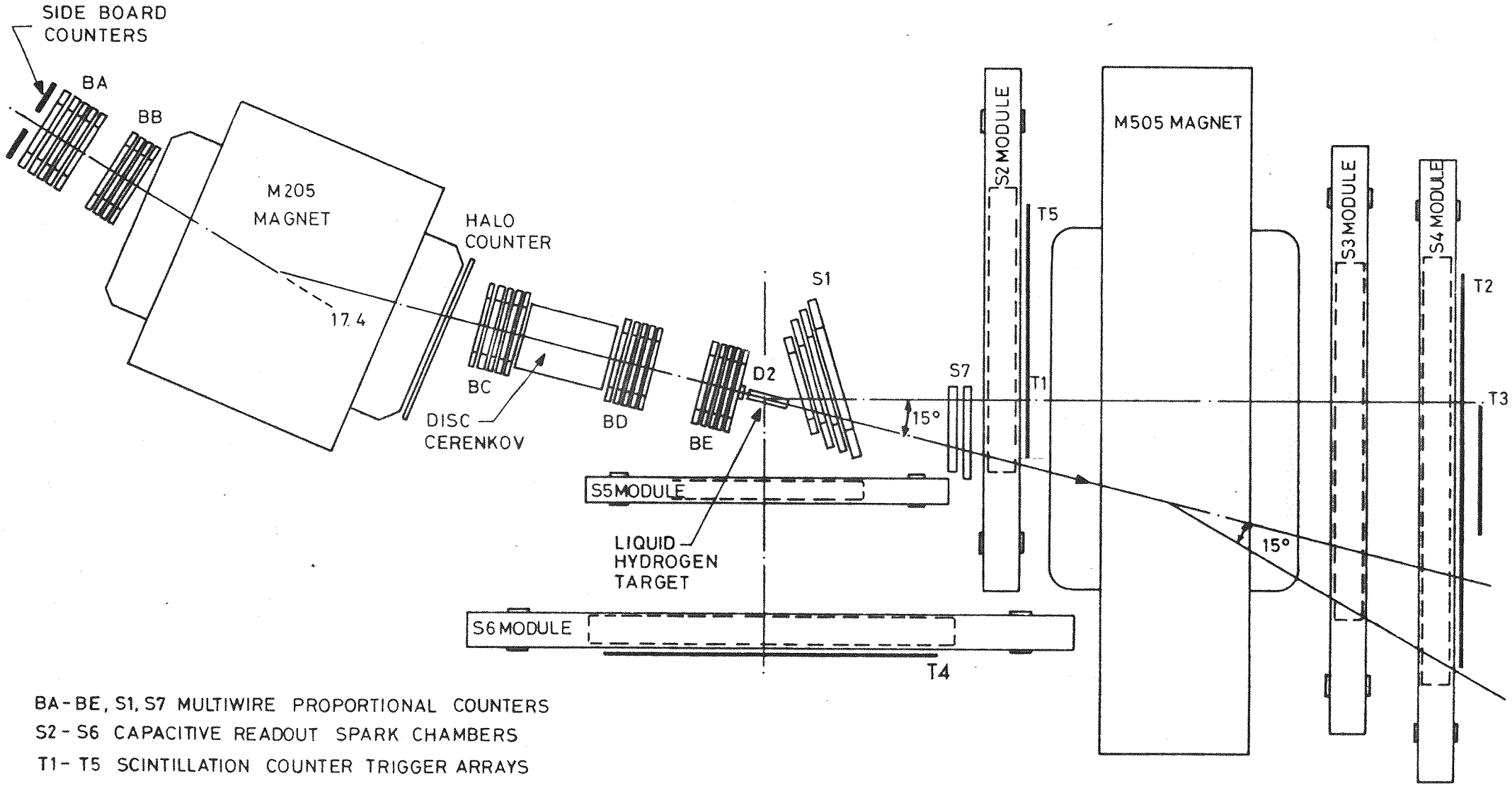

FIG. 2.5 ARRANGEMENT OF DETECTORS AROUND THE TARGET

elements of each hodoscope (T1 to T5) were supported side by side such that they overlapped slightly; the counter dimensions are given in Table 2.1. The scintillators gave a fast response which was used by the decision making logic to define the trigger.

The C-mode trigger required a coincidence between any T1 or any T5 counter, and any T4 counter:

C=CAND. (any T1 + any T5).(any T4)

The T4 hodoscope consisted of eight identical counters forming a large rectangular array. Kinematics required the left scattered particles, associated with those detected by T4, to lie in a limited angular region; the T1 and T5 counters were positioned to overlap this region (Fig.2.6). Thus the acceptance in the C-mode was determined by the dimensions of the T4 array (Fig.2.7).

At small scattering angles the recoil protons did not reach T4 and in the backward direction kaons were scattered behind T4. These angular regions were covered in the spectrometer mode of the experiment. The field of the M505 magnet was adjusted to deflect the beam through 15°. The edges of the T1 and T2 hodoscopes close to the beam were positioned to avoid unscattered beam particles, thus slightly limiting the angular coverage in the forward direction. The height of T1 and T2

TABLE 2.1 Scintillator Hodoscope Dimensions

Element	Height(cm)	Width(cm)	Thickness(cm)
T101	20.0	10.0	0.32
T102	24.0	10.0	0.32
T103	30.0	10.0	0.32
T104	44.0	15.0	0.32
T105	54.0	15.0	0.40
T106	64.0	15.0	0.40
T107	78.0	20.0	0.40
T108	90.0	20.0	0.40
T201	50.0	10.0	0.95
T202	50.0	10.0	0.95
T203	50.0	16.0	0.95
T204	50.0	20.0	0.95
T205	50.0	20.0	0.95
T206	50.0	20.o	0.95
T207	50.0	21.5	0.95
T208	50.0	27.0	0.95
T209	50.0	27.0	0.95
T210	50.0	27.0	0.95
T211	50.0	27.0	0.95
T212	50.0	27.0	0.95
T213	50.0	27.0	0.95
T301	50.0	27.0	0.95
T302	50.0	27.0	0.95
T303	50.0	27.0	0.95
T501	100.0	29.0	2.0
T502	100.0	29.0	2.0
T503	100.0	29.0	2.0
T401	100.0	32.5	2.0
T402	100.0	32.5	2.0
T403	100.0	32.5	2.0
T404	100.0	32.5	2.0
T405	100.0	32.5	2.0
T406	100.0	32.5	2.0
T407	100.0	32.5	2.0
T408	100.0	32.5	2.0

counters was sufficient to detect all particles emerging through the exit window of the M5 magnet (Figs.2.6&2.8). Thus the S-mode acceptance was limited by the aperture of M5.

S-mode triggers were formed mainly from coincidences between T1 and T2 counters. However, forward protons were deflected away from the beam direction by the magnet and so an extra hodosope, T3, was included to provide a trigger for those protons missing T1. Thus the full S-mode trigger was defined by:

$$S = CAND.\{(\text{any } T1.\text{any } T2) + (\text{any } T2.\text{any } T3)\}$$

Large spark chambers with electrodes consisting of arrays of parallel wires were used to locate scattered particle tracks. These chambers have the advantage of being robust and hence simple to construct. Since the beam flux was relatively low, the spark chamber recovery time (20 msec.) was not a serious limitation.

Each gap was designed to define the spark position precisely by combining electrodes with different wire orientations in the same chamber. The modules S2 to S6 (Fig.2.5) each contained three gaps and were positioned to cover the solid angles defined by the counter hodoscopes.

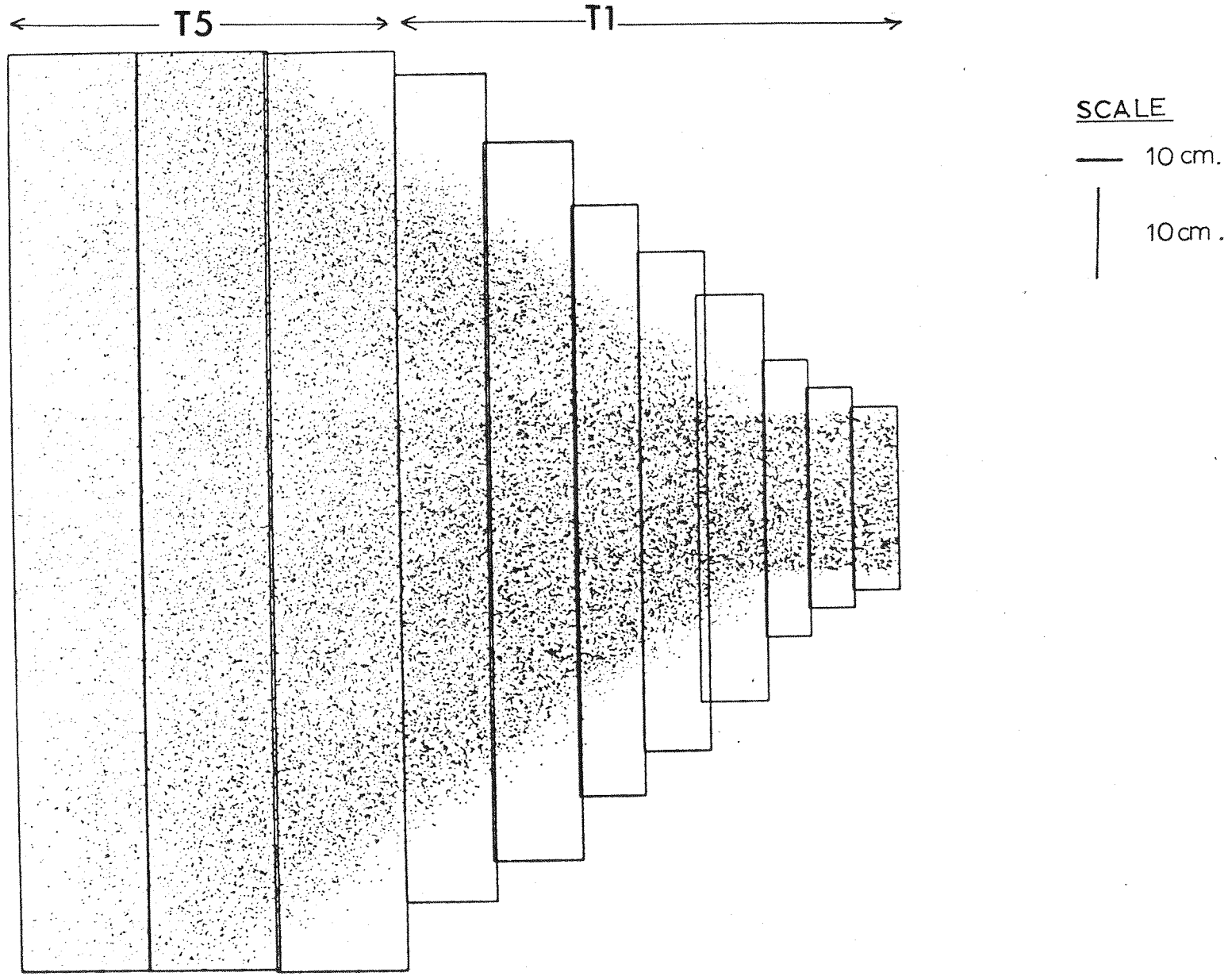

FIG. 2.6 T1/T5 STRUCK COUNTER POSITIONS FOR C&S-MODE EVENTS

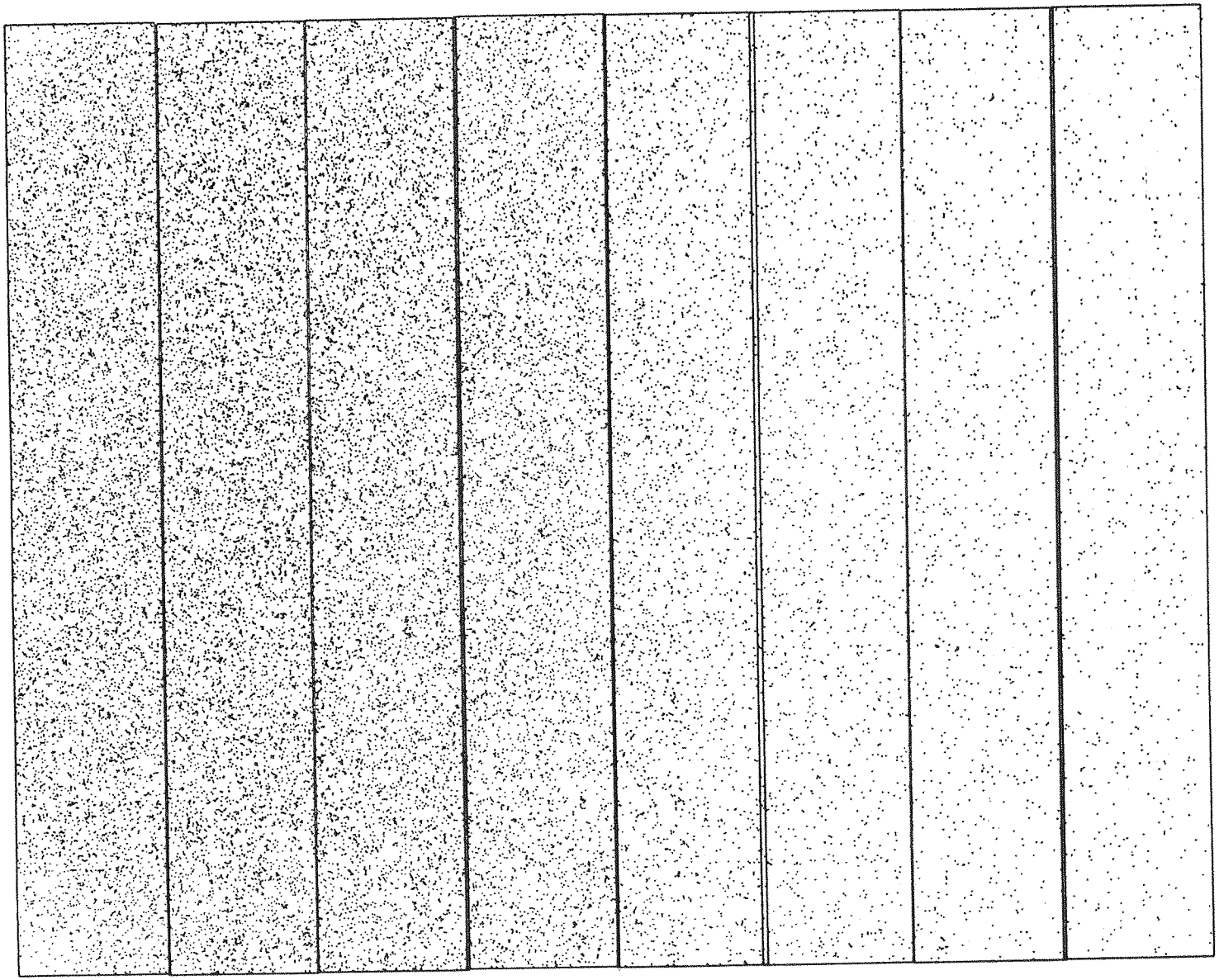

FIG. 2.7 T4 STRUCK COUNTER POSITIONS

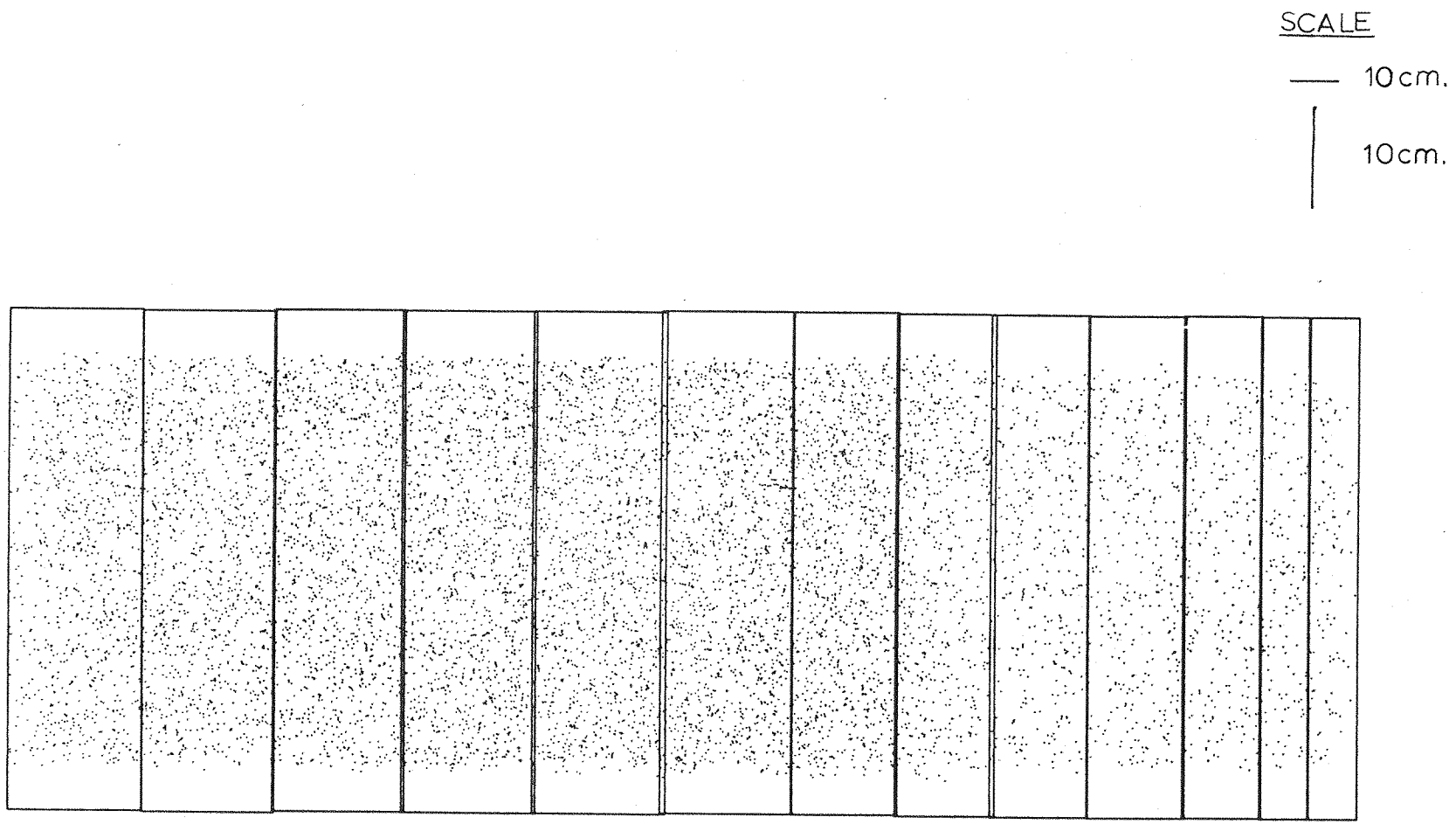

FIG. 2.8 T2 STRUCK COUNTER POSITIONS

An advantage of using wire spark chambers was their ability to resolve multiple tracks. This is an important feature since the 'memory time' of a spark chamber following the passage of a charged particle is relatively long (ie $\sim$1 μsec.). The proportional chambers S1 and S7 were introduced to help in the resolution of tracks close to the beam direction, where the instantaneous flux of particles was a maximum. Because of high cost and difficulty of manufacture of large proportional chambers their size was minimised by mounting them at 15° to the spectrometer axis (Fig.2.5).

A small counter, W1, was positioned behind T204 such that it intersected the beam when the M5 field was turned off. This counter was used to provide a trigger mode for recording particle trajectories straight through the system. The data was used to assess the relative alignment of the detectors.

2.5 Angular Coverage and Normalisation

The majority of S-mode triggers were produced by the charged decay products of the kaons. However, since the decay process is isotropic in the centre of mass and the decay length of the kaon is well known, these events were used to check the normalisation of the differential cross section in the region of the S-mode. Since the two

modes overlapped (Fig2.9), the overlap region provided a valuable check on the relative normalisation of the two modes.

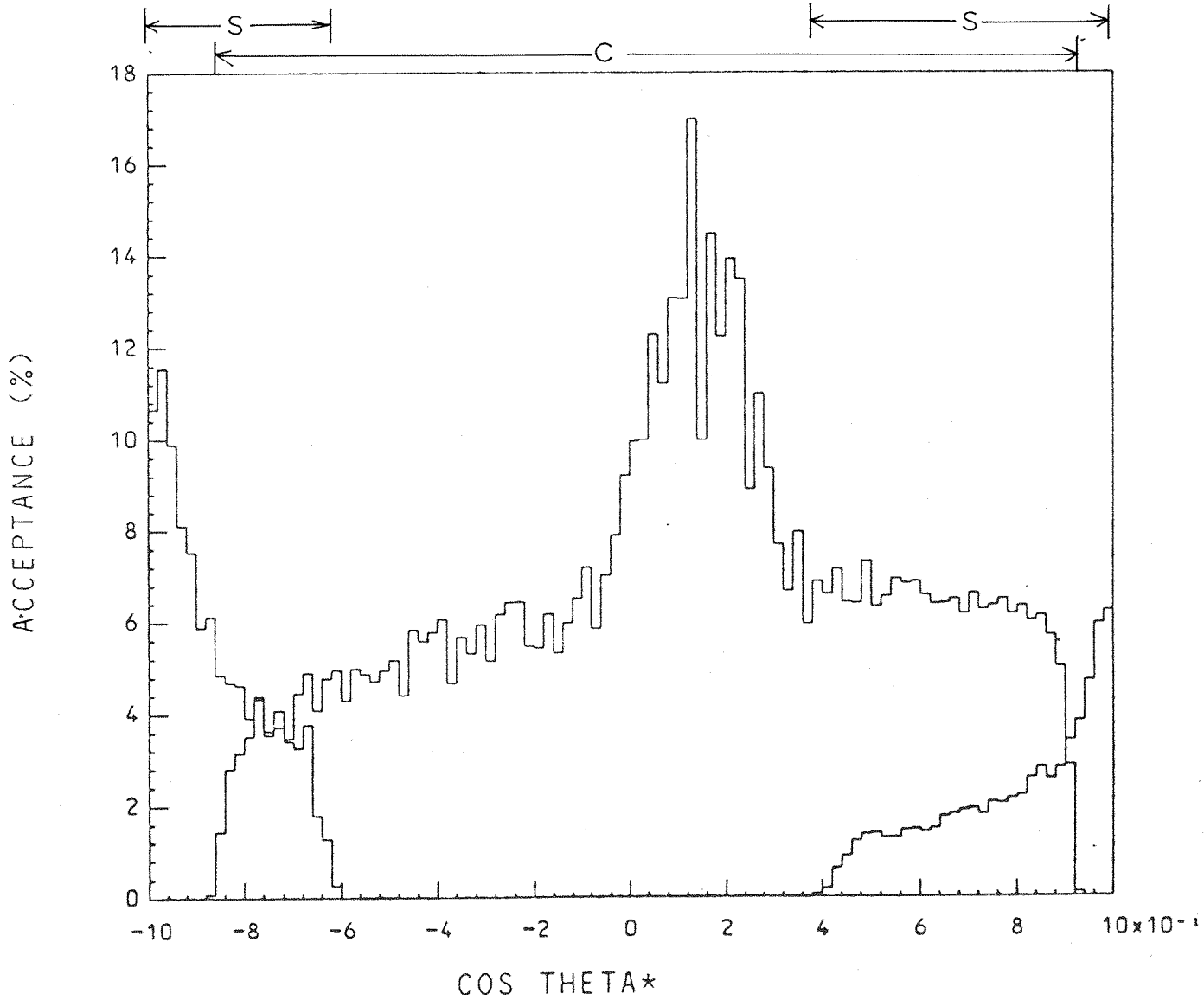

FIG. 2.9 THE ACCEPTANCE OF THE DETECTORS COMPUTED BY MONTE CARLO

CHAPTER 3

Multiwire Proportional Chambers

The multiwire proportional chamber[22] (M.W.P.C.) was developed from the properties of the cylindrical proportional counter, which consists of a fine sense wire (the anode) running along the axis of a cylindrical container (the cathode). As with spark chambers, the principle of detection is to exploit the primary ionization produced by a fast charged particle in the gas envelope of the counter. However in proportional counters the field is such that avalanches are produced close to the sense wire without breakdown of the gas. Thus, although the pulses detected are small and must be amplified, the recovery of the counter is rapid. This property is especially useful in regions of high particle flux, such as the beamline.

The multiwire proportional chamber consists of a plane of parallel sense wires sandwiched between two outer cathode planes. This arrangement reproduces the radial field around each sense wire, such that each wire behaves as an independent counter. Two chambers, mounted with their sense wires at right angles, can therefore be used to record the precise position of a particle.

In this experiment twenty four chambers were used

to track the beam particles through the M205 magnet and into the target. The orientation of their sense wires was either vertical (X chamber) or horizontal (Y chamber). Resolution of multiple tracks would have necessitated use of extra planes mounted at angles other than 90°. However, as the number of multiple tracks expected was small, because of the short resolution time of the chambers, it was decided to reconstruct only those events with single beam tracks. Thus the readout system incorporated encoders which stored only one wire address per chamber, together with information on the number of wires 'hit'. This greatly simplified the acquisition of the proportional chamber data.

3.1 Chamber Construction

Each chamber consisted of a gas tight container supporting three planes of fine parallel wires (Fig.3.1). The wires were supported under tension, and at a constant pitch of 2mm., on a printed circuit board secured with araldite to a fibreglass frame. On the sense plane the wires were electrically independent and made from gold plated tungsten, 20μm. in diameter. The cathode wires were made of Be/Cu alloy, 120μm. in diameter and were connected in parallel. Thicker wire was used for the end (guard) wires on both planes.

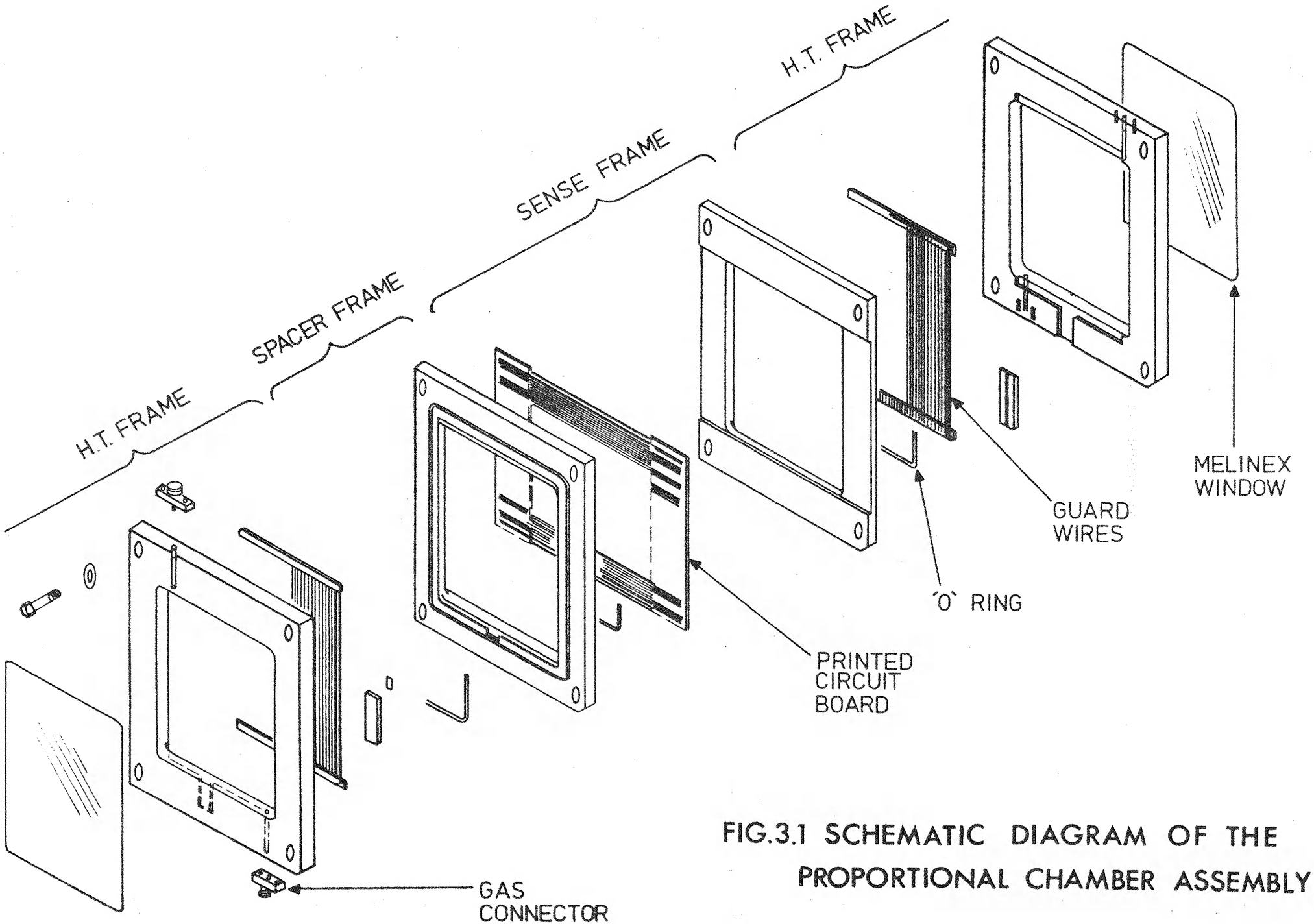

FIG.3.1 SCHEMATIC DIAGRAM OF THE PROPORTIONAL CHAMBER ASSEMBLY

Each chamber was assembled by bolting together a sense plane between two cathode planes, so that the sense wires ran orthogonally to the cathode wires. The frames were machined to provide a uniform gap of 8mm. between the wire planes. "O-rings" were fitted to make a gas tight seal and the chamber windows were closed with thin melinex sheet. Great care was taken in the construction of the chambers as displacements in the chamber geometry cause distortions in the field which can seriously effect the operation of the chamber.[23]

Each chamber had 100 sense wires although in practice the maximum number ever used was 64. The active area was determined by the beam size at the chamber's position in the beamline and those wires not used were connected to 'earth'. The chambers were then mounted on aluminium frames, which also supported the amplifiers (PLATE 2) . The frames were held in the beamline by aluminium cages and the entrance and exit windows of the cages were closed by thin aluminium foil, to screen the chambers from stray fields and so reduce the pickup of noise signals on the sense wires.

Spatial resolution was improved by staggering the chambers. The middle X chamber in each group was displaced by half a wire spacing relative to its neighbours using 1mm. spacers. Each alternate Y chamber

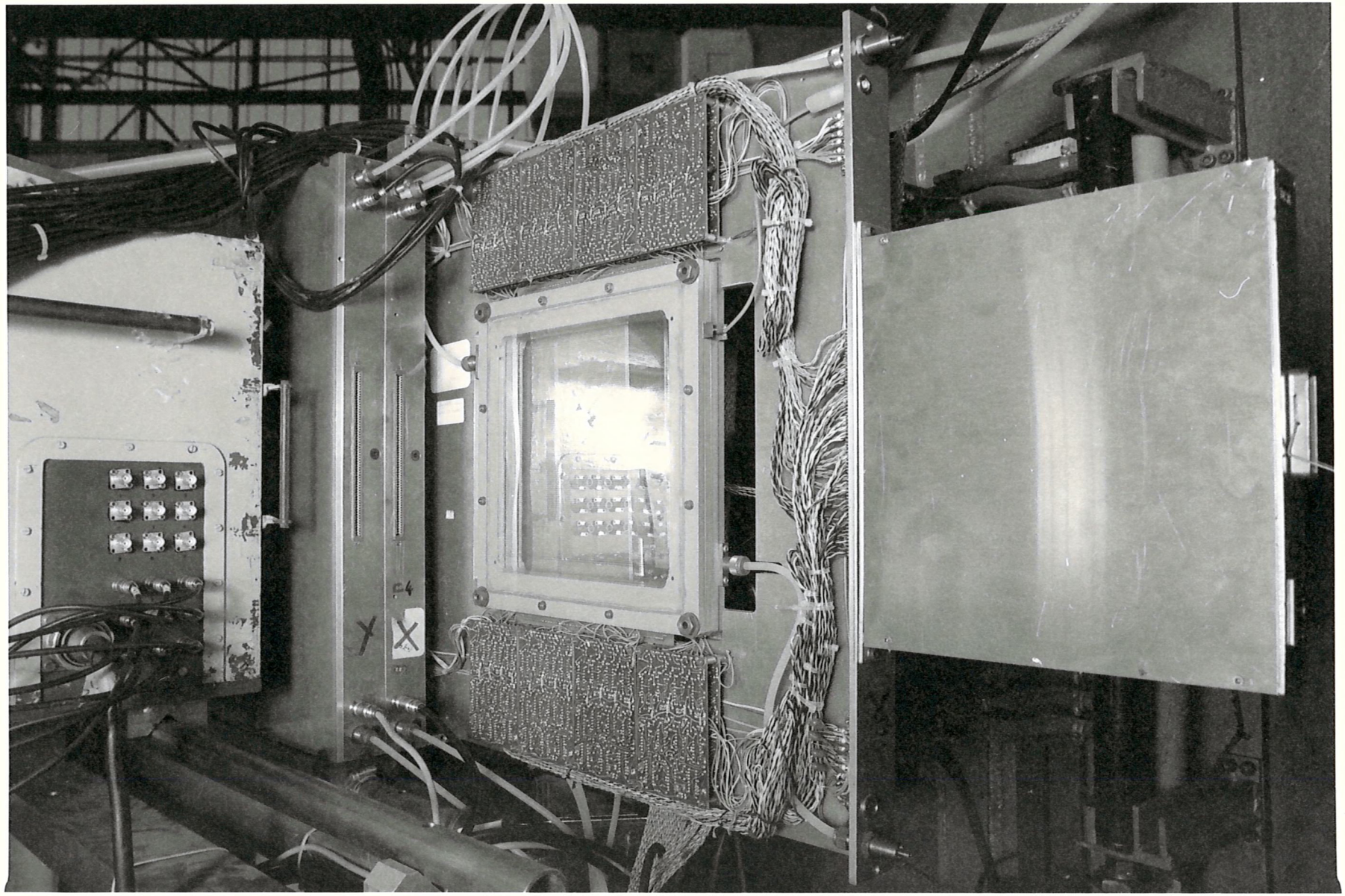

Plate 2 Beam M.W.P.C. and Support Cage

was displaced by machining 1mm. from its slot in the base of the cage.

3.2 Pulse Formation

Avalanches are produced when the primary electrons are accelerated to such energies that ionization of the gas medium results. The gas amplification varies exponentially with the field[24] and so the formation of avalanches is strongly dependent on the distribution of the field within the chamber. In the gaps between the wire planes the electrons drift steadily in a uniform field. The threshold for proportional amplification is only reached close to the sense wires where the field exhibits a $\frac{1}{r}$ dependence. Since the avalanche region is so close to the wires (e.g. half the ionization is produced in one mean free path which for argon is approximately 1 μm.) the electrons are collected immediately and the signal on the sense wire is almost entirely due to the movement of the positive ions towards the cathode. The movement of the positive charge induces smaller positive pulses on neighbouring sense wires. Thus providing the amplifiers are sensitive only to negative pulses each wire acts as an independent counter.

Because the field gradient at the wires is

determined by their diameter the sense wires used were as fine as the mechanical strength of the materials permitted. The cathode wires were much thicker as a high field gradient here is detrimental to chamber operation. Similarly the guard wires were used to reduce the field at the edge of the chamber and hence prevented edge breakdown.

The size of the output pulses is also affected by the gas mixture, which in this experiment consisted of 84.8% argon, 14.9% carbon dioxide and 0.3% freon 13B1. Argon was used as the basis of the mixture since it is inert and has a relatively good stopping power. However argon breaks down in relatively low fields due to photoionization. To obtain high gas amplification the photons must be absorbed without producing secondary ionization. This type of quenching effect is provided by molecules of carbon dioxide which absorb photons during dissociation. Carbon dioxide also has the advantage of possessing a high stopping power. Trace elements of an electronegative gas, freon 13B1, were included to capture low energy electrons in the drift region and particularly those originating from secondary effects at the cathode. This had the effect of reducing the sensitive volume around each sense wire, which improved the time resolution. For 100% efficiency there must be an overlap in the sensitive volumes of adjacent

wires and so the concentration of freon must be small. The freon, because of its complex molecular structure (CF_3Br), is also efficient at quenching photons.

3.3 Readout System

The organisation of the readout system is shown schematically in Figure 3.2. The chamber signals were amplified and discriminated close to the chamber to produce MECL pulses of well defined width. This information was sent to the logic racks as an eight bit code, generated by the chamber encoder, and was fed onto the CAMAC data highway via a MECL latch (RL406). The load pulse to the latches was formed from a D1.D2 coincidence (10 nsec long) delayed to coincide with the arrival of the chamber signals (100 nsec long). If the beam particle failed to produce a trigger a reset pulse was generated by the trigger circuitry to clear the latch for the next beam particle.

(a) Amplifiers

The total time required to collect all the charge on the sense wire is governed by the positive ion mobility and is typically 150 μsec. However the initial rise of the pulse is fast because of the enhanced ion

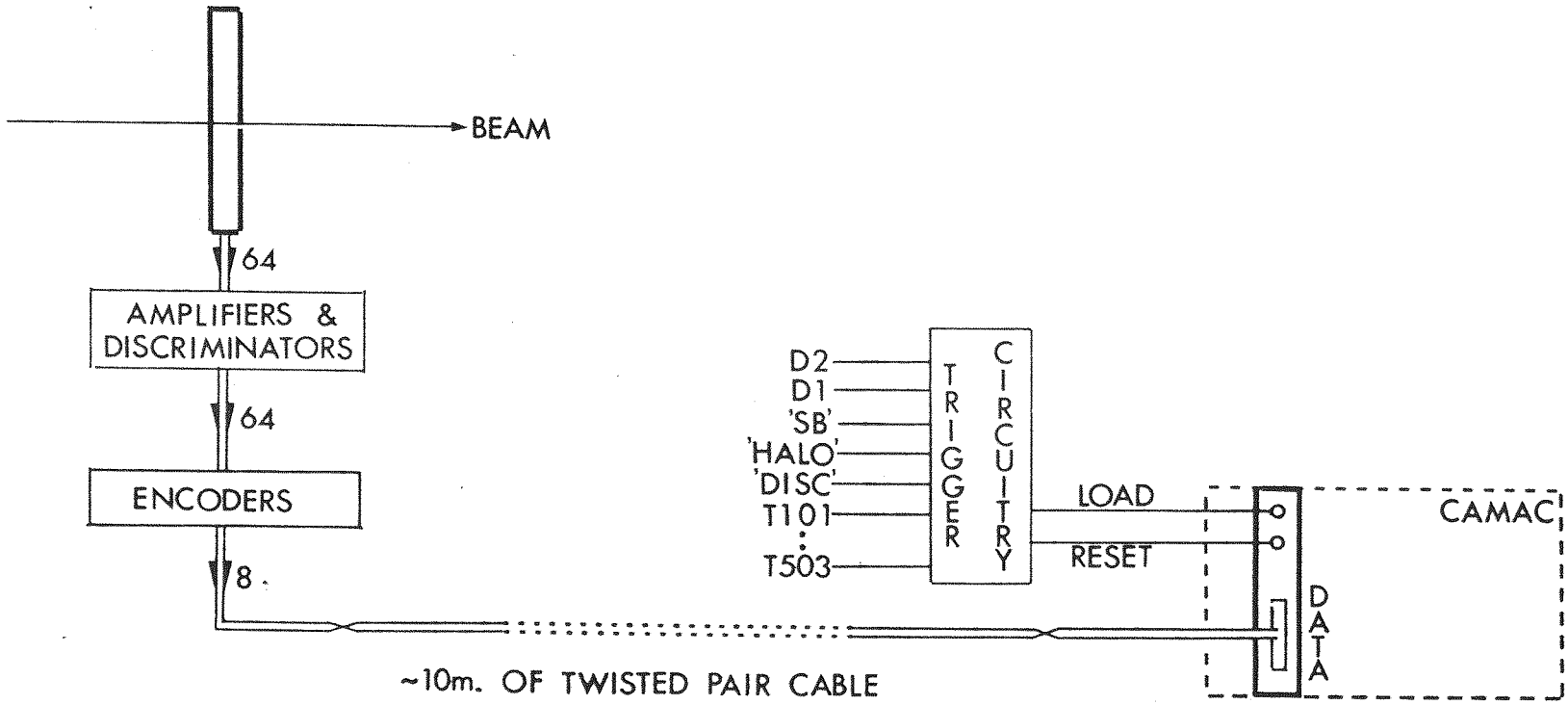

FIG. 3.2 SCHEMATIC DIAGRAM OF THE BEAM M.W.P.C. READOUT SYSTEM

mobility in the high field region close to the wire. It is the initial rise that must be exploited by the amplifiers for the chamber to have good time resolution. The amplifiers were therfore designed to have low input impedance (Fig.3.3), such that any stray wire capacitance was effectively short circuited and produced little integration of the sense wire signal. Limitation of the voltage signal on the driven wire by the input impedance also minimised crosstalk between adjacent wires.

The voltage pulse developed after the first stage was further amplified and then discriminated. The discriminator threshold was set as low as possible to provide maximum chamber sensitivity. A threshold of 6mV gave good performance under test conditions out of the beamline. The output from the discriminator was shaped by a short recovery time monostable to give an output pulse length of 50 nsecs. The pulse was also differentiated at various stages to ensure that the monostable did not become saturated. The signal and its complement were connected to encoders by twisted pair transmission lines.

Amplifier performance in the beamline was found to be less satisfactory than under test conditions. Each wire behaved as an aerial for noise signals which were

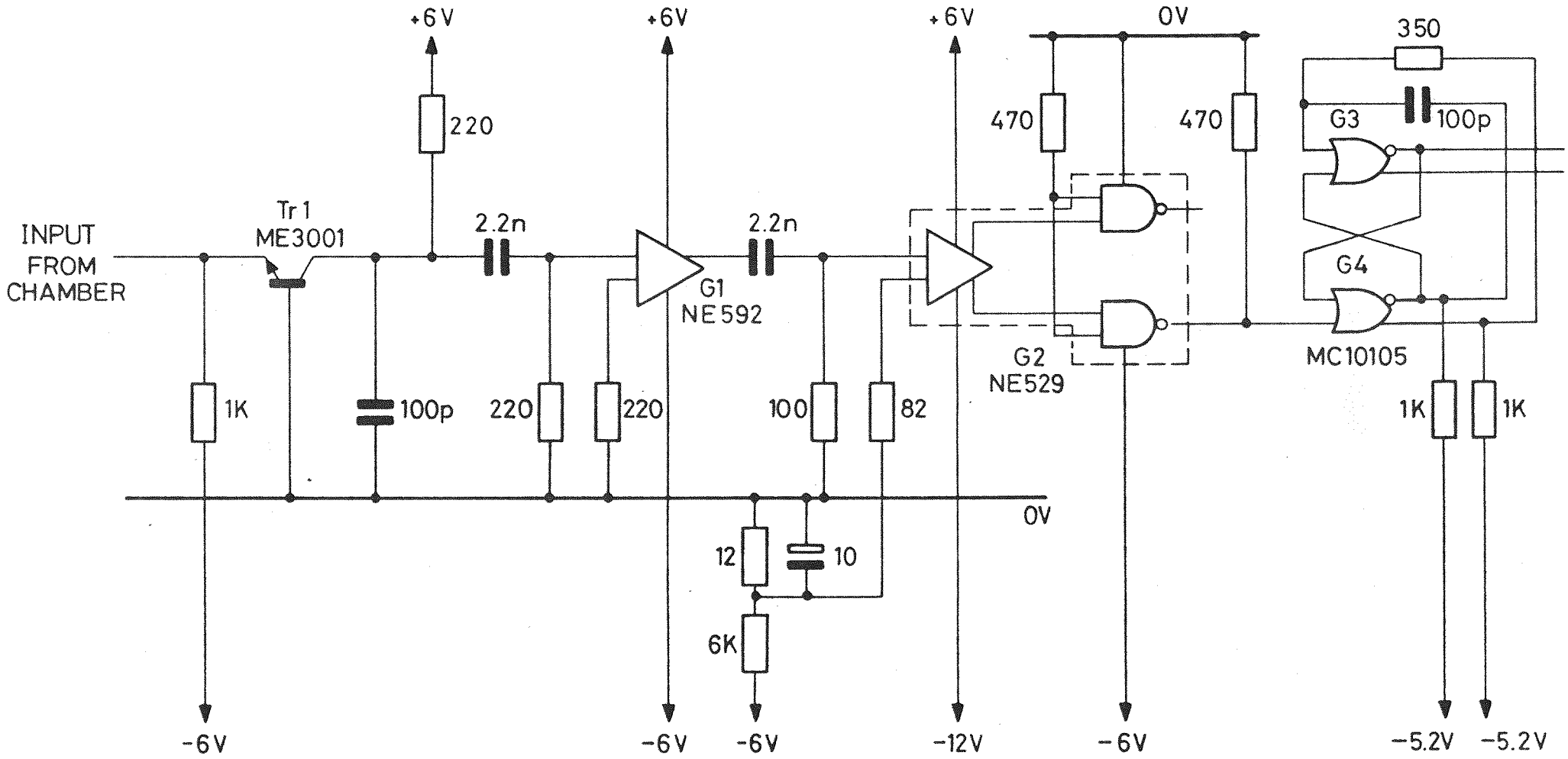

FIG.3.3 MULTIWIRE PROPORTIONAL CHAMBER PREAMPLIFIER

capable of triggering the discriminator. To overcome this the discriminator threshold was changed to 12mV. and great care was taken to see that all connections to ground at the input were via the shortest path. This effectively eliminated the problem of noisy wires.

(b)Encoders

Each encoder generated an eight bit binary code according to the state of its sixty four input lines. Each wire was represented by an address, ranging from 0 to 63, which was displayed on the first six bits. If more than one wire was activated a priority scheme ensured that the lowest address was recorded.

The remaining two bits were used for the chamber status which could therefore take one of four values. In general, because the particles were travelling at right angles to the planes of sense wires, a single particle would activate either one wire (SINGLE) or at most, two adjacent wires (DOUBLE). More than one particle passing through within the resolution time of the chamber would normally be detected by at least two non-adjacent wires (MULTIPLE). The remaining code (ZERO) was used to record the absence of signals on the sense wires.

The encoding was achieved principally with eight

line priority encoders (Fig 3.4). These produced an output in binary code of the highest order input and any input of lower priority was ignored. Thus selection of one wire from sixtyfour required two levels of encoding.

The address of each wire was determined in two ways to give a simple method of finding the status. Each forward address (FA1 to FA6) was the number of the first active wire counting from one end of the line of inputs and each reverse address (RA1 to RA6) was the number of the first active wire counted from the other end of the line. The chamber status could now be easily determined from the sum of the forward and reverse codes. For example, a SINGLE resulted in a sum of 63, whereas a DOUBLE produced a sum of 62. A MULTIPLE always resulted in a sum of less than 62. This sum appeared in code on the outputs of the adders and was easily used, as indicated, to determine the levels of the remaining two bits. The forward code appeared on the six address bits.

In the case of a SINGLE the position of the particle was obtained directly from the wire address. For DOUBLES, the position was found by displacing the coordinate, determined from the encoded address, by half a wire spacing. ZERO and MULTIPLE wire addresses were ignored in the reconstruction of the beam track for that event.

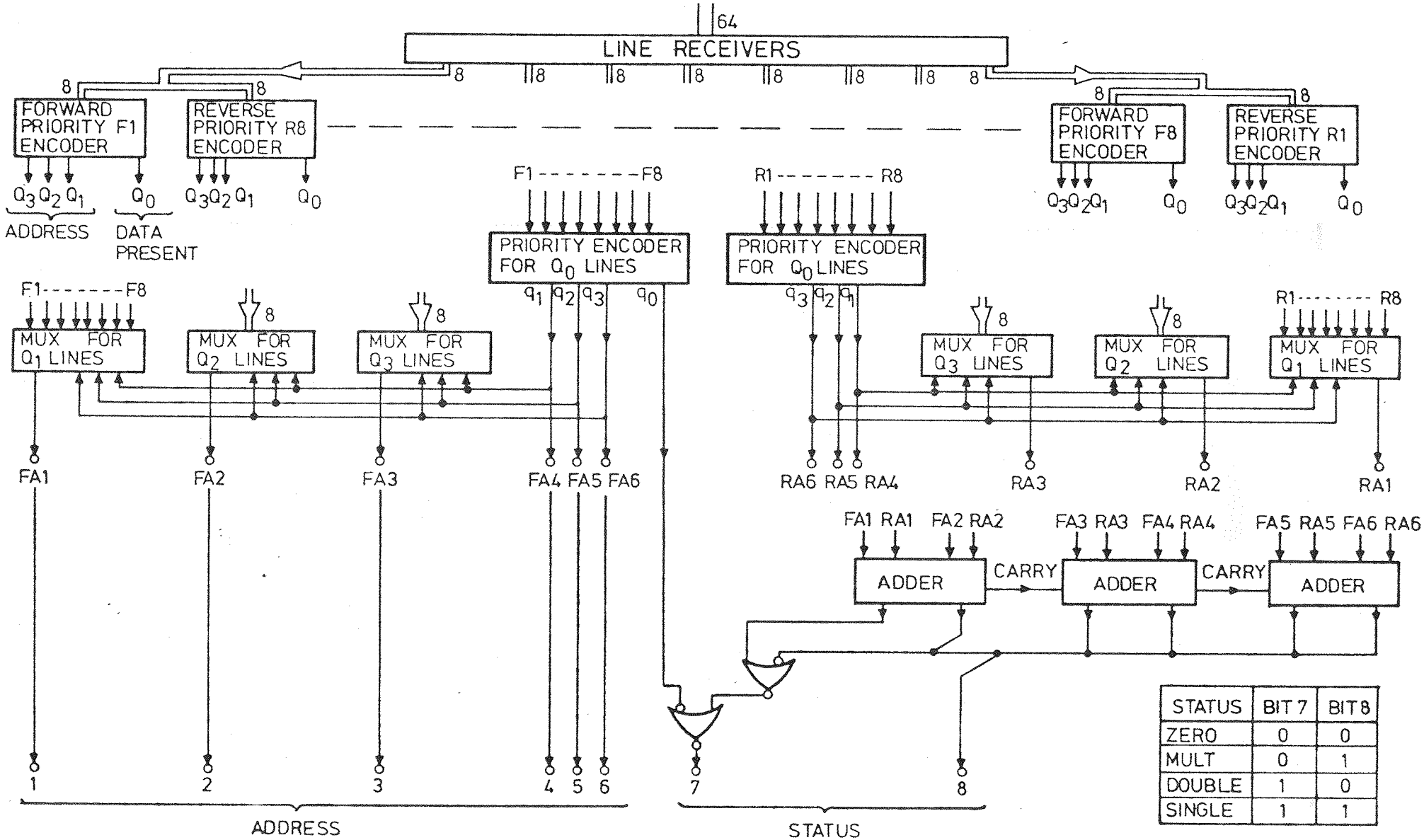

STATUS	BIT 7	BIT 8
ZERO	0	0
MULT	0	1
DOUBLE	1	0
SINGLE	1	1

FIG. 3.4 SCHEMATIC DIAGRAM OF A PROPORTIONAL CHAMBER ENCODER

3.4 Operation and Performance

The argon/ carbon dioxide /freon gas mixture was preferred to the most commonly used mixture, 'magic gas', because of its non-corrosive, non-explosive nature and its availability ready mixed in gas bottles. The chambers were flushed at a rate of 50 cc/min and the gas was allowed to escape into the atmosphere. Gas piping at the chamber outlets prevented air from seeping back and poisioning the mixture in the chambers.

The variation of detection efficiency with the applied voltage for a typical chamber is shown in Figure **3**.5. The chambers were set to an operating voltage approximately 100 volts above the 'knee' of the plateau. Under normal conditions the chambers took less than 1μA standing current which increased to 5μA in the burst. This current was sensitive to the flux of particles through the chambers. Each chamber was driven by a seperate supply which tripped if the current exceeded 50μA. This protected the chambers from continuous breakdown in the event of sparking.

The effect of varying the delay in the load pulse is also shown in Figure **3**.5. Increasing the delay appears to allow time for the primary ionization to drift to neighbouring sense wires since the proportion of doubles and multiples increases. The delay was chosen

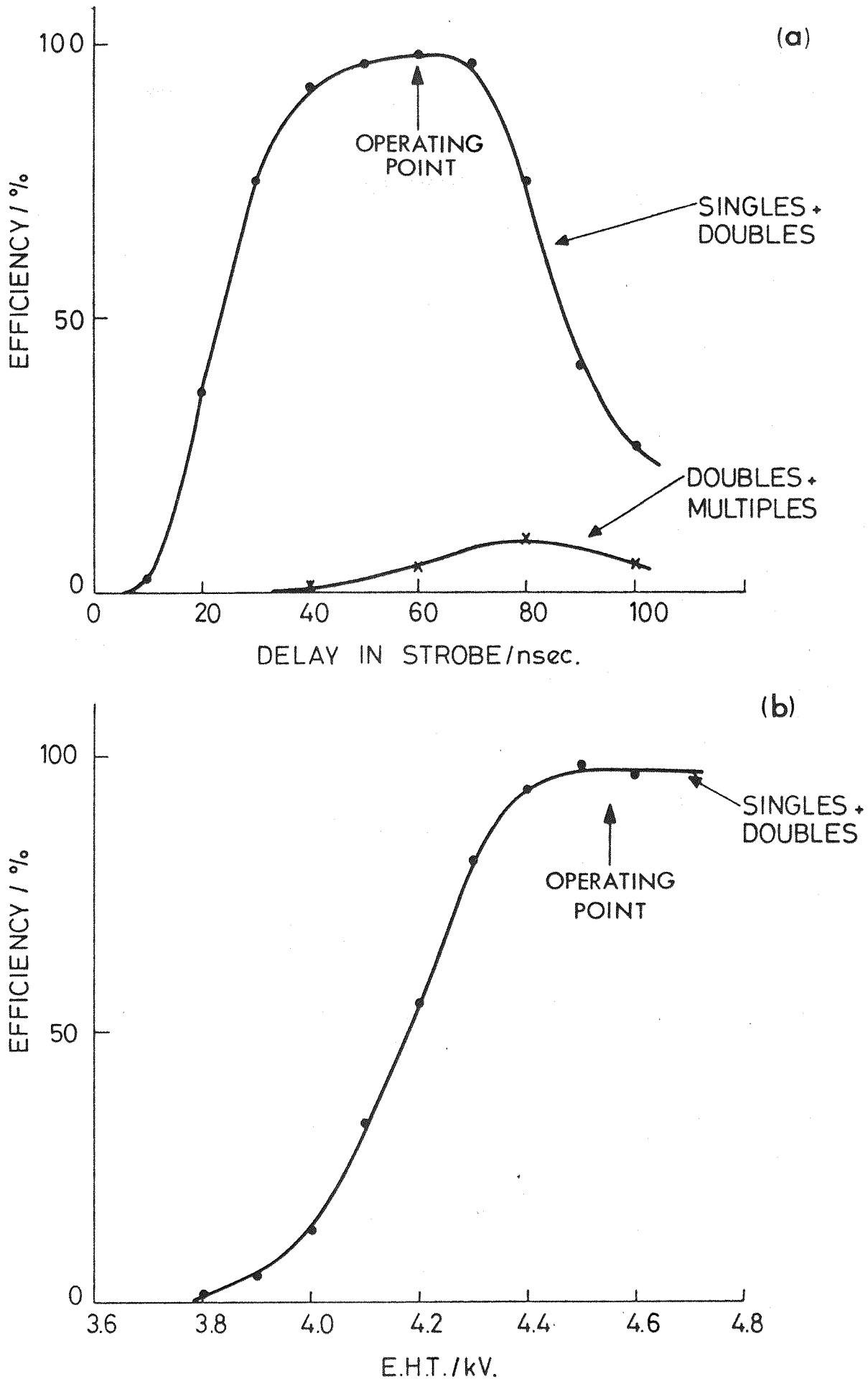

FIG. 3.5 PERFORMANCE OF A TYPICAL BEAM PROPORTIONAL CHAMBER

such that the sum of the singles and doubles was a maximum. The risetime of the efficiency curve indicates the jitter time in the arrival of the pulses (30 nsec.).

After 2 cycles of data taking several chambers were seen to take a few μA standing current. On inspection white deposit was seen on both sense and cathode planes. This was analysed and found to be copper bromide presumably produced by the dissociation products of the freon gas. Very occasionally a chamber would take 10-20 μA standing current and this was found to be caused by one or more slack wires. Consequently chambers were removed periodically for cleaning and maintenance, usually between cycles of data taking, with the result that they maintained high efficiency over all cycles.

3.5 S1 and S7 MWPC's

The S1 and S7 proportional chambers were used to facilitate the identification of scattered particle tracks, particularly in the beam region. As described previously, the operation of MWPC's depends on their internal geometry and the gas mixture used. The beam chambers and the S1/S7 chambers were identical in this respect and as they used the same sense pulse amplification system they operated under the same

conditions. However the size and location of chambers S1 and S7 in the beamline necessitated certain design modifications, and a different readout system was used for complete recording of all wires 'struck' during an event.

(a) S1 Chambers

Efficient operation of MWPC's depends upon the sense wires being maintained in their plane of operation under suitable tension. In large chambers the critical tension required exceeds the mechanical strength of the wires used and the latter must therefore be supported in position.[25] This support was provided by insulated nylon wires stretched across the sense plane in the centre of the chamber. Chamber efficiency in the region of the support wires was restored by equating their potential with the equipotential corresponding to the plane of the support wire.

The size of the S1 chambers varied with distance from the target but because of their rectangular shape the Y chambers contained the longest sense wires and were therefore subject to the greatest strain. In spite of the fact that mounting these chambers at 15° to the spectrometer axis enabled a reduction in their size it still proved necessary to use support wires in all but

the smaller X chamber.

(b)S7 Chambers

The S7 system consisted of two identical chambers which were restricted in size and covered only the region through which unscattered beam particles passed after traversing the target. The small size of the chambers eliminated the need for support wires. The sense planes were supported on a three sided frame, the fourth side being open so as not to obstruct the movement of scattered particles (PLATE 3). As a consequence of the three sided design of the frame, the cathode and sense wires were parallel to one another, but there were no detectable effects on chamber performance due to this unorthodox arrangement. The two chambers were supported at 30^{o} relative to each other in the beamline, thus enabling detection and reconstruction of particle positions from the 'struck' wires.

(c)S1,S7 Readout

The beam chamber encoding system was not used on the S1/S7 chambers because of the need to resolve multiple tracks. Instead the outputs from the discriminators were fed in groups of 16 into memory

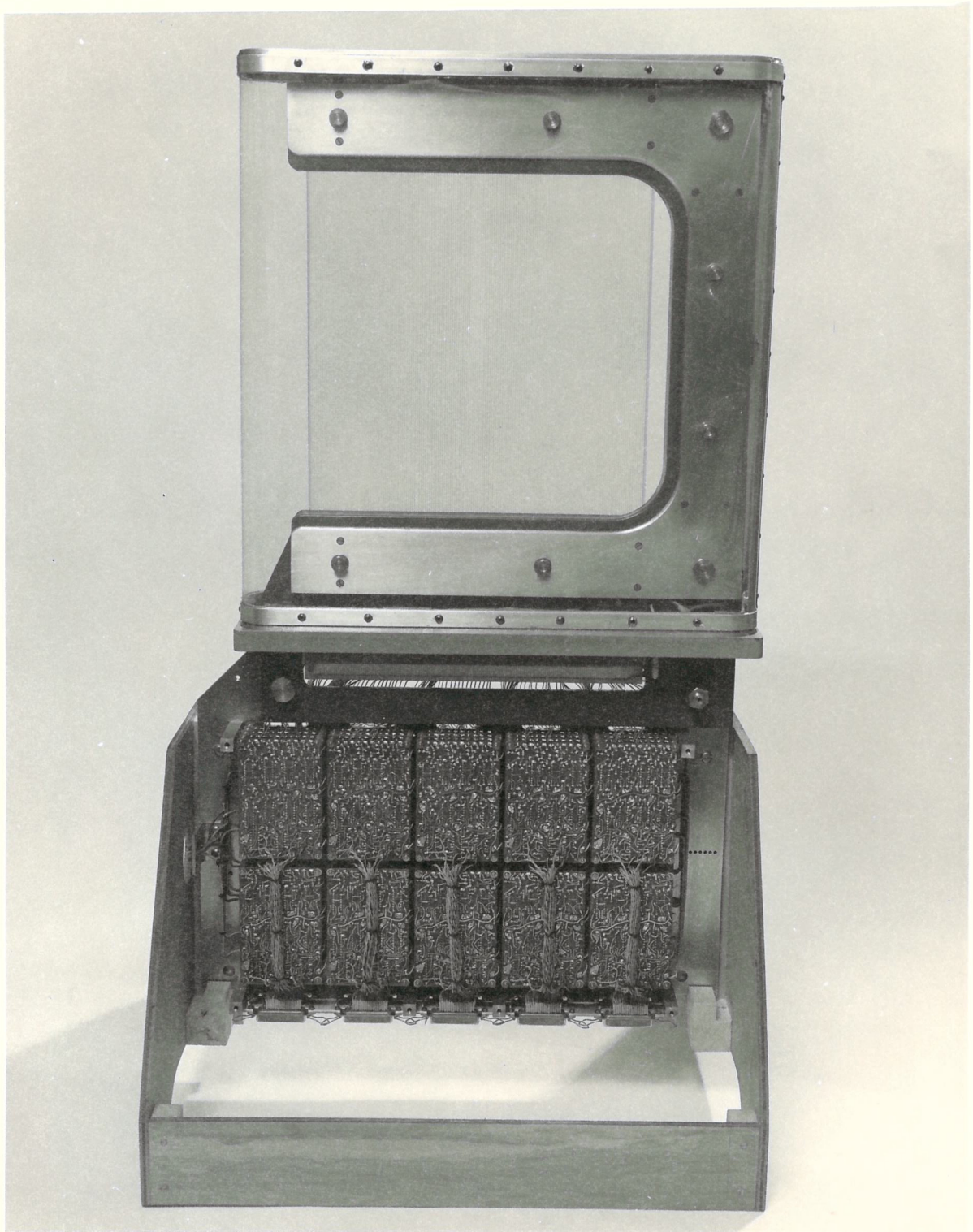

Plate 3 S7 M.W.P.C.

boards, which were subsequently interogated by a 'start-scan' pulse. The scan proceeded until a board with set channels was located. At this point the scan stopped and the data from all sixteen wires were transferred to an interface (RL402), together with the encoded board numbers. The data were presented on the CAMAC read lines as binary coded numbers, one wire address for every CAMAC read operation. The RL402 interface read out the address of hit wires only, and since the scan interogation took less than 1nsec. per wire the readout time was short compared with direct readout.

CHAPTER 4

Capacitive Readout Spark Chambers

4.1 Principle of Operation

When the ionization deposited in the chamber by a charged particle is subjected to a sufficiently high field breakdown in the chamber gas occurs with a spark forming along the ionization trail. In wire chambers the spark current is constrained to run along those wires nearest the breakdown point. These wires determine the spark position with a spatial accuracy dependent upon the wire spacing.

In the capacitive readout system[26] each wire is connected to chamber earth via its own capacitor. When a wire conducts its capacitor is left charged thus providing a 'memory' for the spark information. During the readout process the charge is removed and detected by sensing components.

To avoid spurious breakdown the field is applied to the chamber in the form of a high voltage pulse and any track produced within the 'memory time' of the chamber is recorded. This is the time for which enough ionization persists after the passage of a particle to

precipitate a spark when the chamber is fired. To facilitate track reconstruction the memory time should be as short as possible. It is reduced by maintaining a small field across the chamber to sweep the ionization from the gap more quickly. This clearing field is adjusted such that the memory time is just longer than the delay in applying the firing pulse. It also aids in the recovery of the chamber after breakdown.

4.2 Chamber Construction

Each electrode consisted of a plane of parallel wires mounted under tension on a rectangular aluminium frame and at a constant pitch of 1mm. The wires were soldered onto printed circuit boards which were bolted onto the long sides of the frames. In some cases the wires were stretched directly across the frame but in others they were either at an angle of 15° or 30° to the short side. The wire used was made of beryllium-copper and was 0.12mm in diameter.

A single chamber was made by bolting together two of these frames. The chamber assembly was designed to ensure a gas-tight volume was maintained whilst providing both good insulation and a uniform gap (1cm.) between electrodes (Fig4.1). Each electrode determined the spark position in one direction only. The

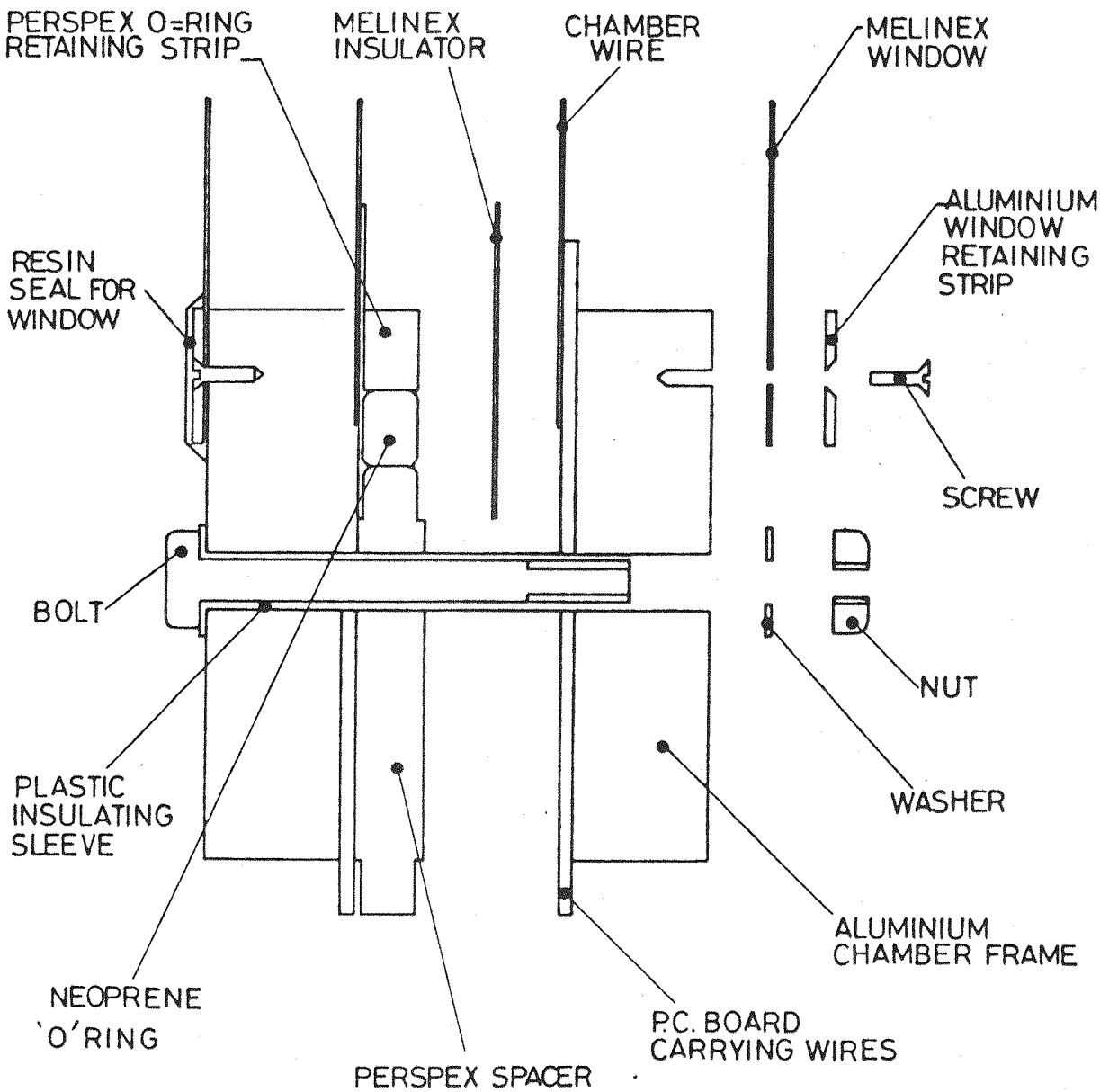

FIG. 4.1 SCHEMATIC DIAGRAM SHOWING THE SPARK CHAMBER ASSEMBLY

combination of wire planes with different orientations in each chamber made it possible to determine the precise position of the spark. This design restricted the functional area of the chambers to the regions of overlap between the electrode planes.

The three chambers forming the S6 module are shown in PLATE 4.

4.3 Firing System

The high field was produced by sending large pulses of opposite polarity to appear simultaneously on opposing wire planes. These pulses were produced by rapidly earthing the high voltage side of two capacitors. The switch used was a hydrogen thyratron (CX1157) which was capable of delivering up to 1000A with a risetime of approximately 30nsec.[27]

The firing sequence was initiated by a trigger pulse from the coincidence logic which was amplified using the circuit of Figure4.2 to operate the thyratron switch. The effect of earthing the capacitors, C10 and C11, was to induce large negative pulses on their output side which were carried to the chambers by coaxial transmission lines.

The scheme for applying the high voltage to the

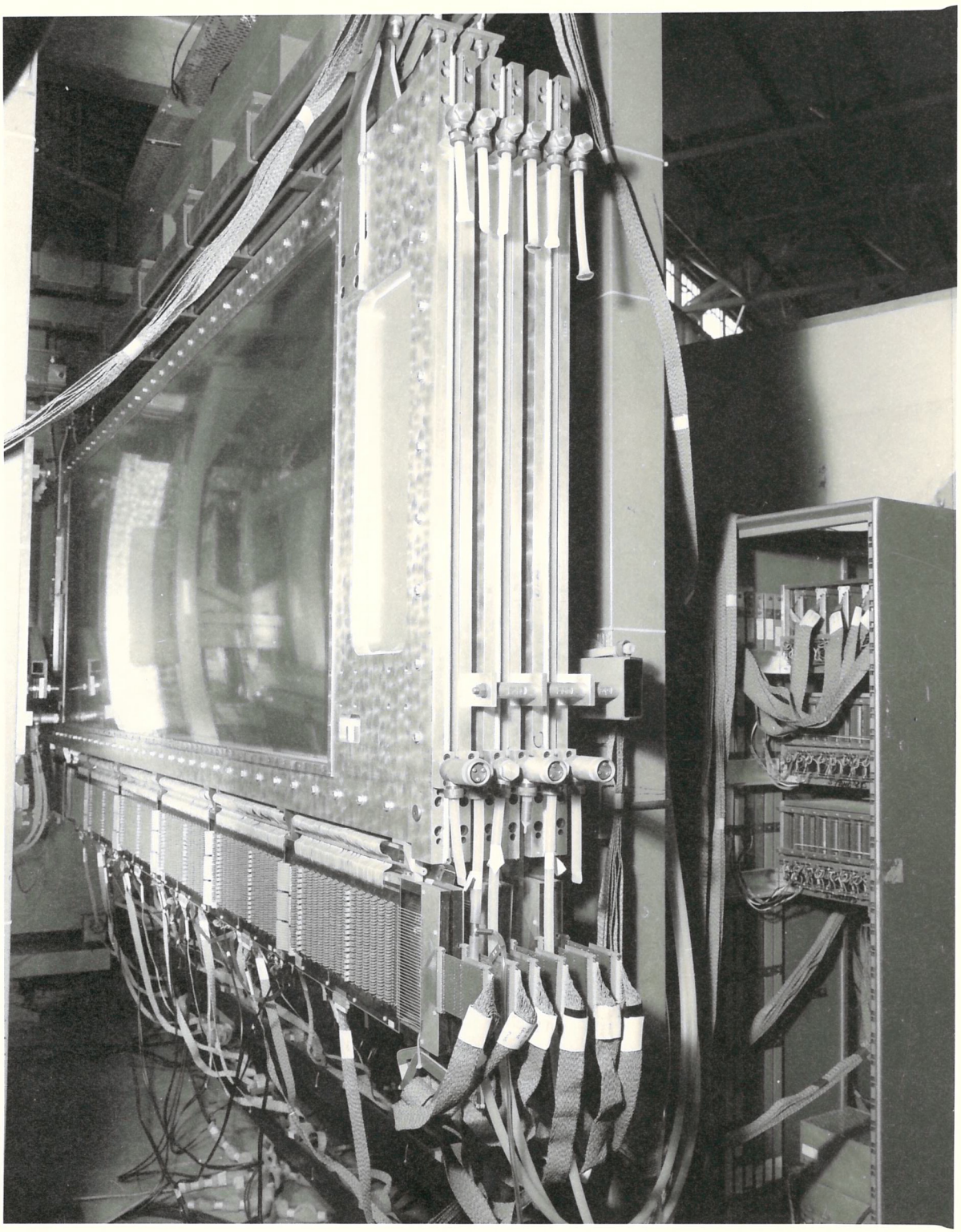

Plate 4 S6 Spark Chamber Module

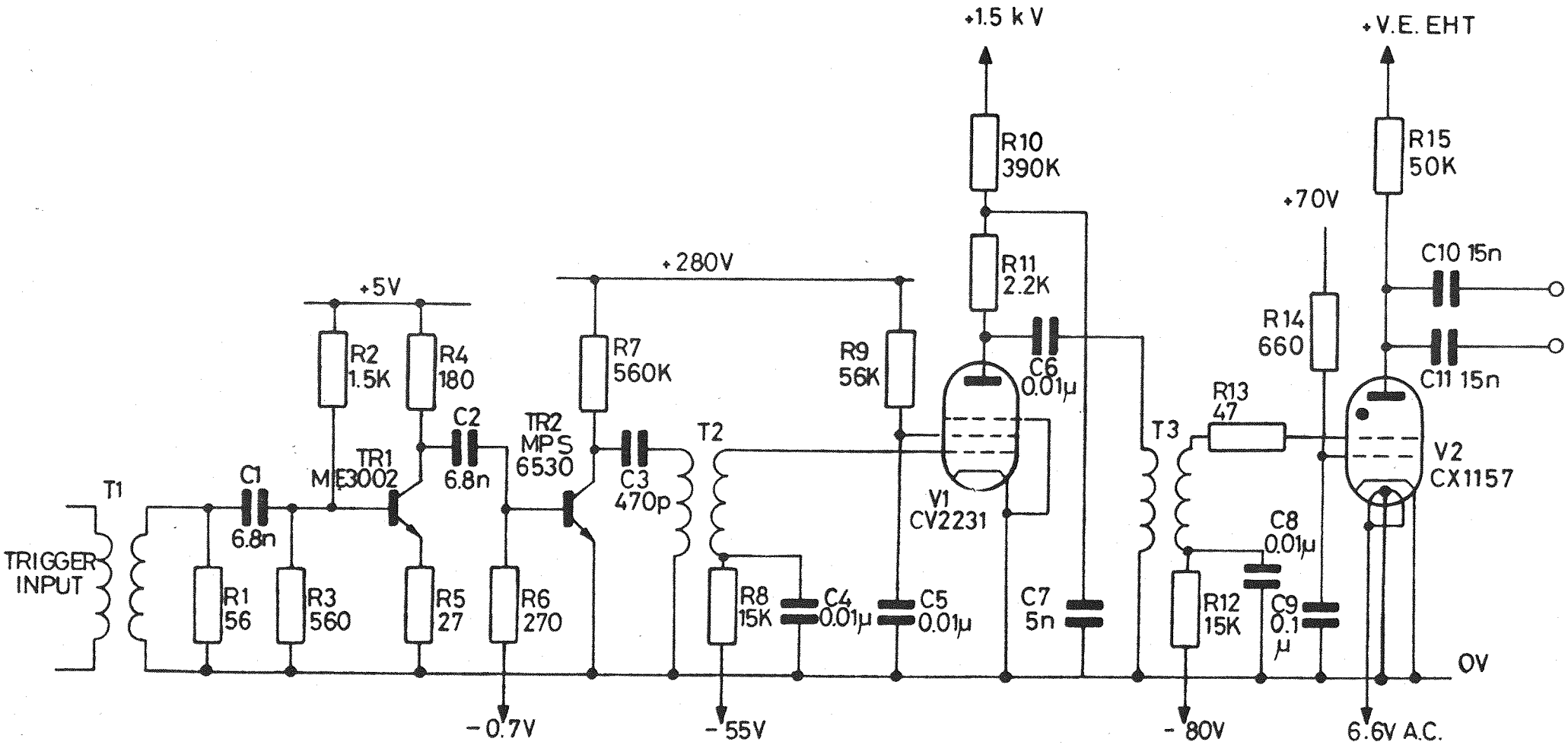

FIG.4.2 CIRCUIT DIAGRAM OF THE HYDROGEN THYRATRON UNIT

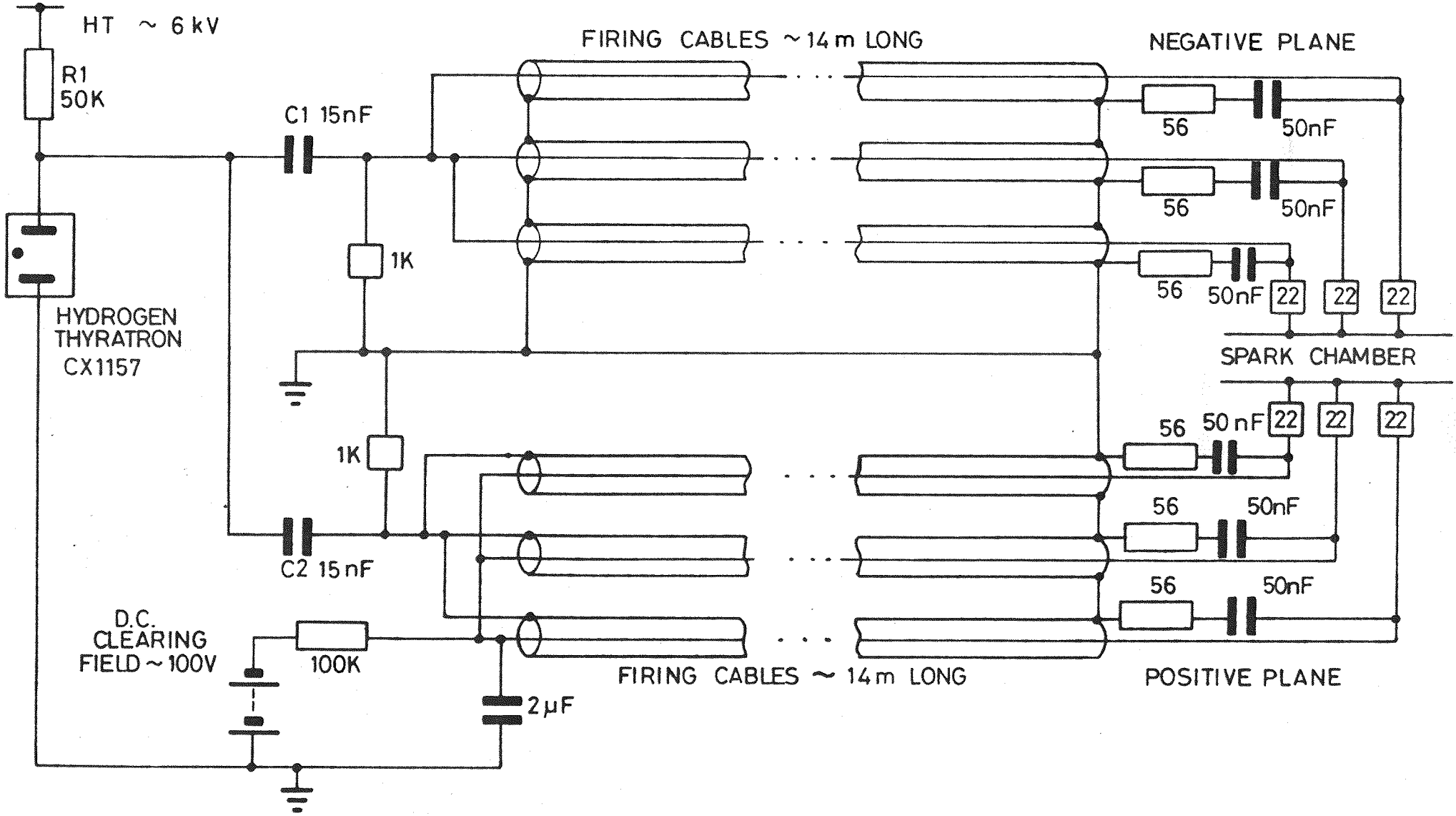

FIG. 4.3 ARRANGEMENT OF THE SPARK CHAMBER HIGH VOLTAGE PULSING SYSTEM

chambers is shown in Figure4.3. On the negative plane the pulse appeared directly on the chamber. On the positive side the capacitor was connected to the outer conductor of the cable which was earthed at the chamber end. This induced a positive pulse on the chamber. The high voltage was distributed to three regions of the chamber to reduce the possibility of 'spark robbing'.

The clearing field was maintained across the gap in the opposite sense to the high voltage field. Thus the ions which began to drift under the influence of the clearing field were swept back into the gap where they initiated the spark.

4.4 Readout System

The readout system was developed from a CERN design[28] by Bristol University.[29] Its mode of operation can be explained in principle by referring to Figure 4.4 which shows the chamber circuitry used for recording the charge state of the capacitors.

Breakdown is initiated by the appearance of the high voltage pulses on the chamber earth lines. When breakdown occurs the Zener diode becomes forward biased and conducts the spark current, which leaves the capacitor charged. The voltage on the capacitor is

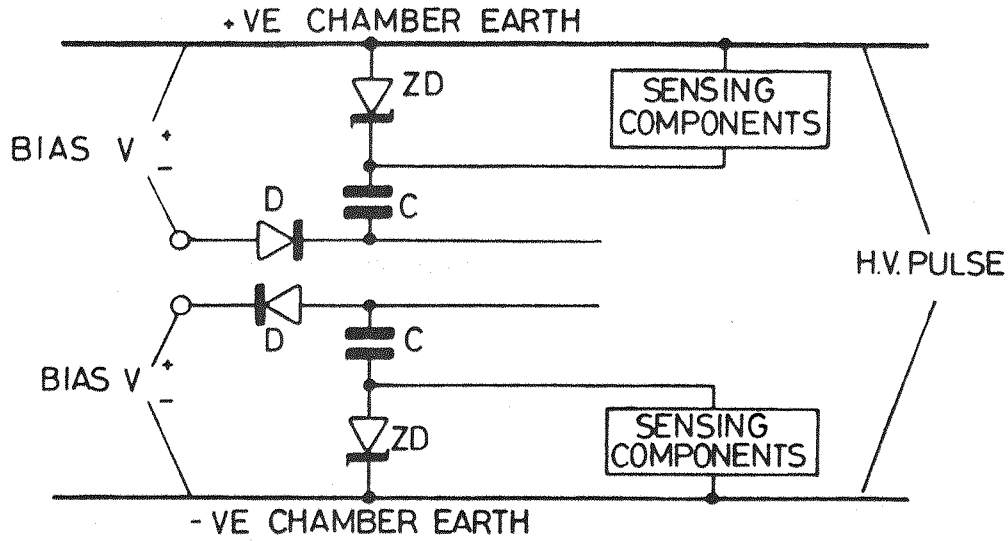

FIG 4.4 CHAMBER CIRCUITRY FOR TWO WIRES

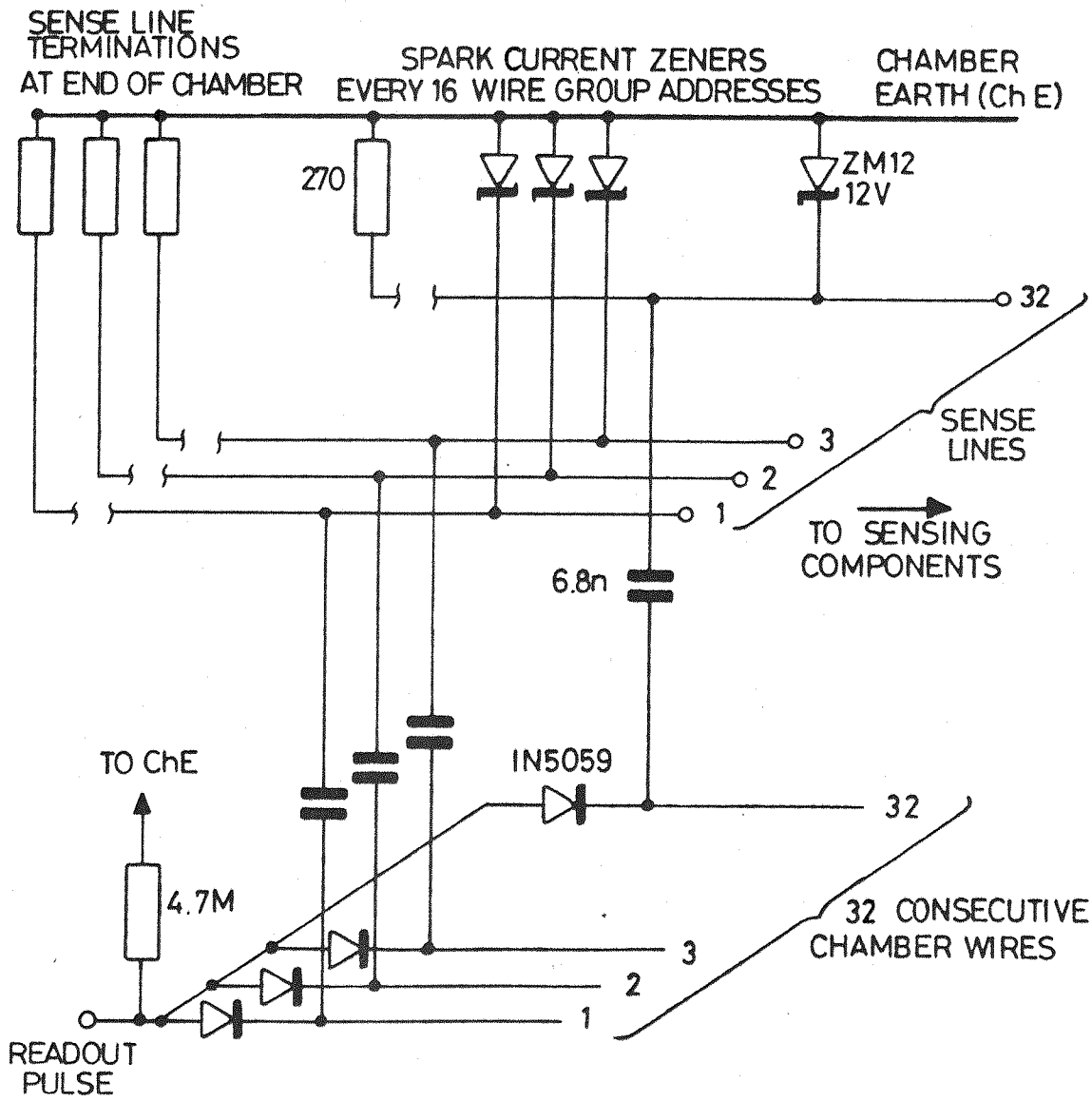

FIG 4.5 GROUPING OF COMPONENTS INTO WIRE GROUP ADDRESSES

limited by the diode which conducts when its bias voltage is exceeded. The function of the diode is twofold since it also allows the read pulse to reach the capacitor in the readout phase. The effect of applying the 'READ' pulse is to remove the bias voltage which allows the capacitor to discharge. On the sense side the zener diode is now reverse biased and so the charge is forced towards the sensing components.

A common 'READ' pulse was applied to thirtytwo consecutive wires, with each capacitor within the group presenting its data on a separate sense line (Fig.4.5). This procedure was repeated in time sequence for subsequent groups of wires and in each case the data were read onto the same thirtytwo lines. Data were recorded, therefore, in terms of a wire group address, corresponding to a particular group of capacitors, together with a 'bit pattern' reflecting the pulses detected on the sense lines. The readout sequence was controlled by a special interface which had direct access to the memory of the computer for rapid transfer of data. The total time taken to read all fifteen chambers in a given event varied with the number of sparks but typically was found to be about 5msec.

4.5 Readout Logic

The 'READ' pulse was supplied to the capacitors by address driver modules. The modules used for negative and positive planes differed slightly (Figs.4.6&4.7). In each module that part of the circuit enclosed by broken lines was repeated sixteen times each channel supplying the 'READ' pulse for one wire group address. The remainder of the circuit was common to all channels.

Initially the pulse bias rail was held at 60 volts to prevent the capacitors from being discharged by any r.f. ringing produced by the firing pulse. When the ringing had stopped a readout gate was applied simultaneously to all address drivers in the system which reduced the pulse bias rail to seven volts and which remained until the read cycle had been completed.

In the subsequent readout sequence the wire group address generated by the interface was decoded by the control logic to produce:

(a) a 'card enable', which selected the module, and

(b) an 'individual enable', which identified the correct channel.

The 'read' pulse produced by the circuit was superimposed on the pulse bias rail through a transformer, T1, and was carried to the chamber via

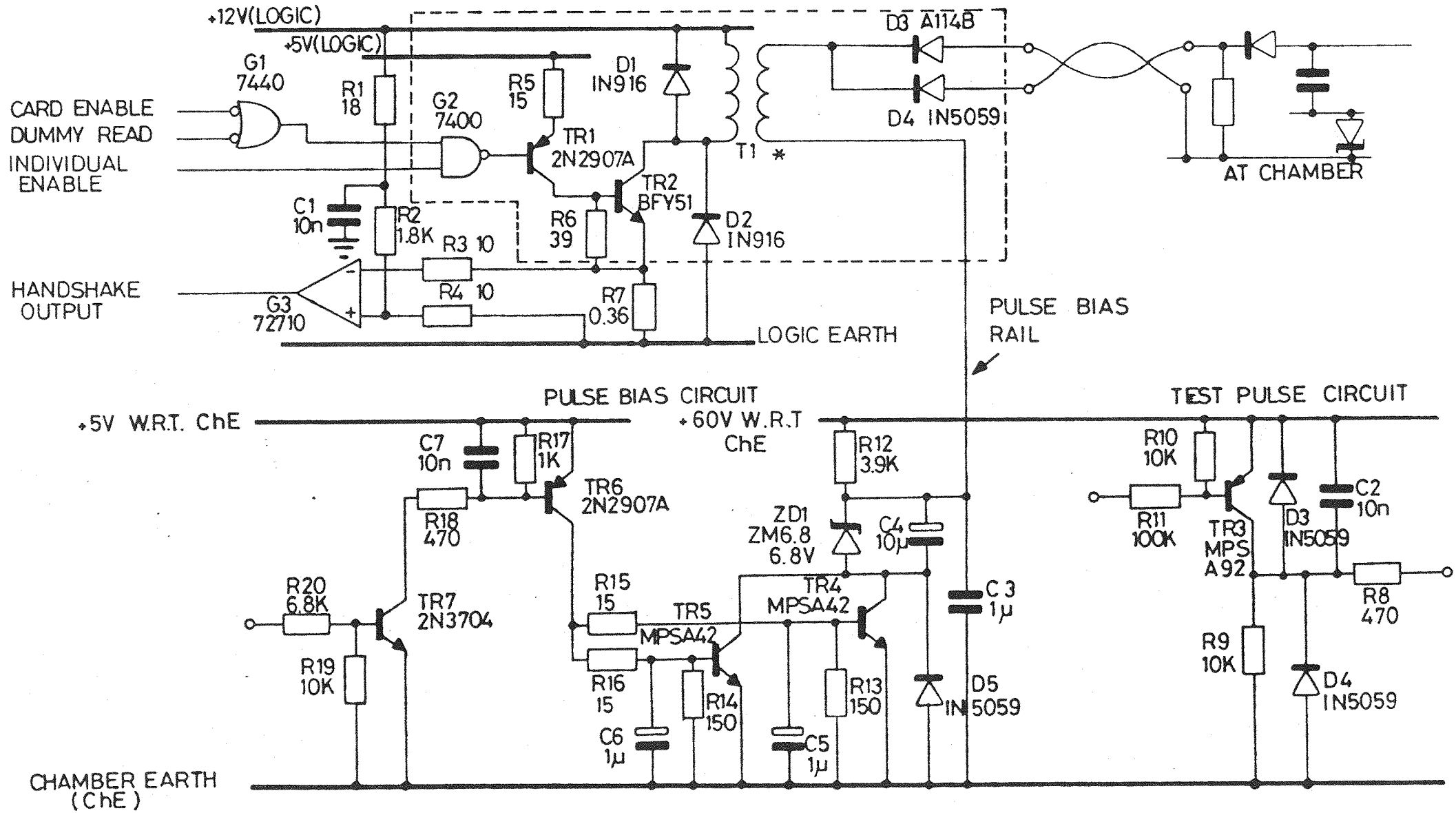

FIG.4.6 NEGATIVE PLANE ADDRESS DRIVER CIRCUIT DIAGRAM

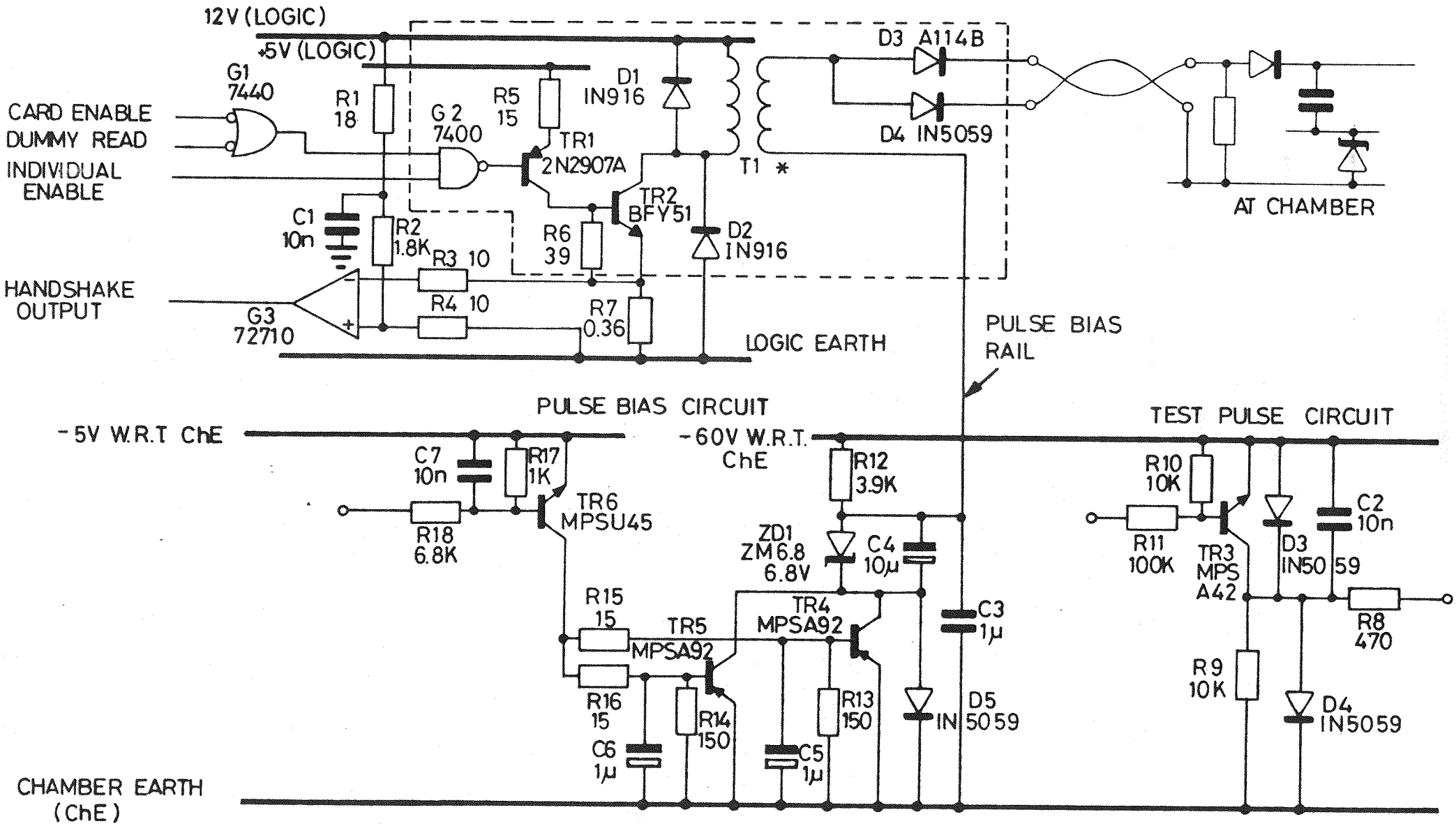

FIG.4.7 POSITIVE PLANE ADDRESS DRIVER CIRCUIT DIAGRAM

twisted pair cable. This cancelled the diode bias and discharged the capacitor.

The circuit used to detect pulses on the sense lines is shown in Figure4.8. The pulses were shaped by an attenuator and digitised before being fed onto the 'data highway'. The comparator, G1, had a variable threshold which was used to discriminate against noise signals.

After completion of the readout sequence a 'dummy read' signal was issued in preparation for the next event to remove any residual charge on the capacitors. A test pulse facility was also provided to simulate sparks, without firing the chambers, by charging capacitors in well-defined patterns. The pulses detected on the sense lines were used to locate faults in the readout logic.

On both the address drivers and the sense amplifiers the logic was isolated from high voltages by transformers. It was found necessary to wrap the twisted pair transmission cables around ferrite cores to 'choke' the pickup of noise signals produced by the firing pulse.

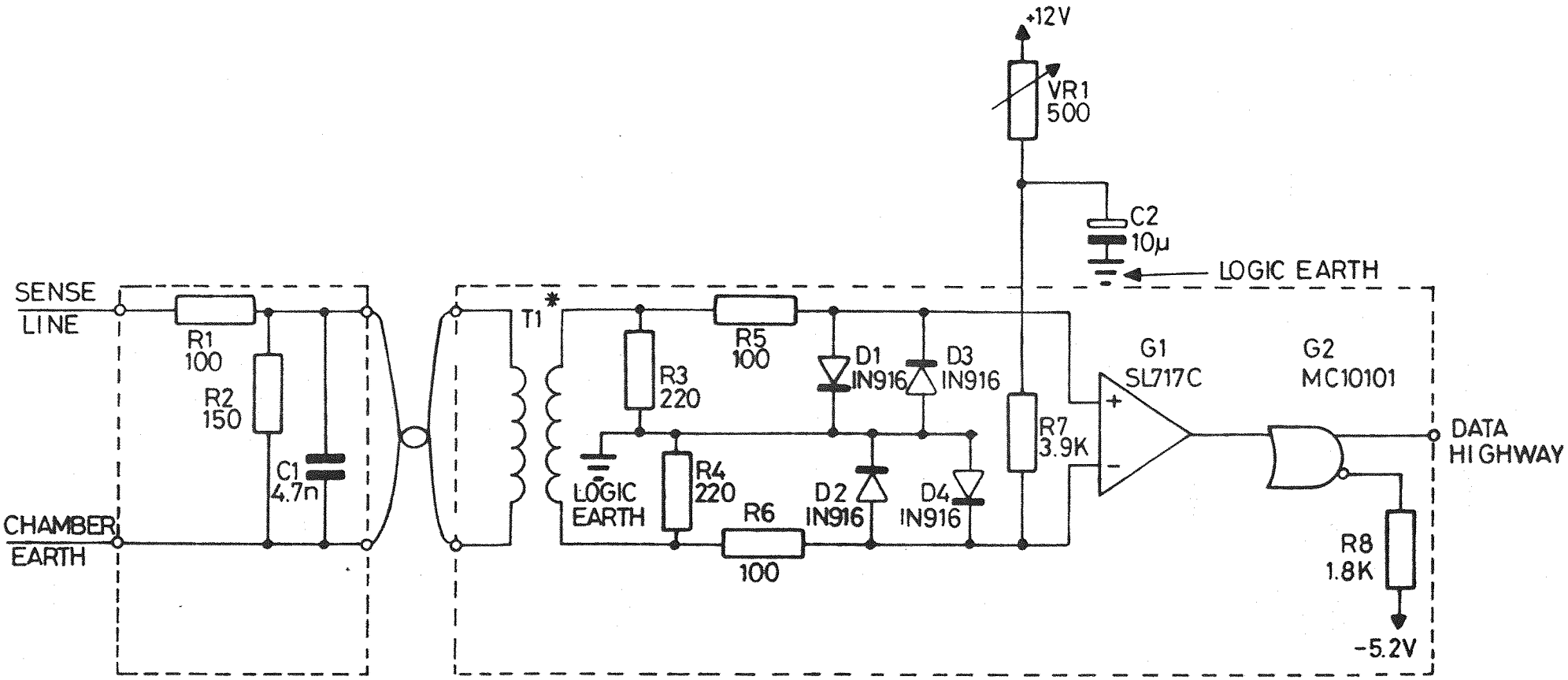

FIG. 4.8 SENSE AMPLIFIER CIRCUIT DIAGRAM

4.6 Operation and Performance

The chambers were flushed with a mixture of neon and helium (70% Ne, 30% He) at a rate of 400 cm^3 per minute. Noble gases are used because of their small electron affinity with neon being most suitable since it has a high gas amplification factor and a relatively high total specific ionization. However a mixture of neon and helium is much cheaper and still gives satisfactory results. The gas was recycled to minimise the cost of supplying fifteen chambers. The mixture was purified on the return side and any drop in pressure in the system was compensated by adding pure Ne/He mixture. The chambers were kept at a slight excess pressure because of the difficulty of excluding all leaks. The presence of oxygen is quite detrimental to the operation of spark chambers because of its electronegativity. The level of oxygen was continuously monitored and never exceeded 0.15%.

The field across the chambers was controlled by adjustment of the high voltage applied to the thyratrons and, typically, produced a characteristic variation in efficiency (Fig.4.9). The operational voltage, as indicated by the arrow in Figure 4.9, provided near-100% efficiency generally, but the chambers were scanned for inefficient regions. The only significant decrease

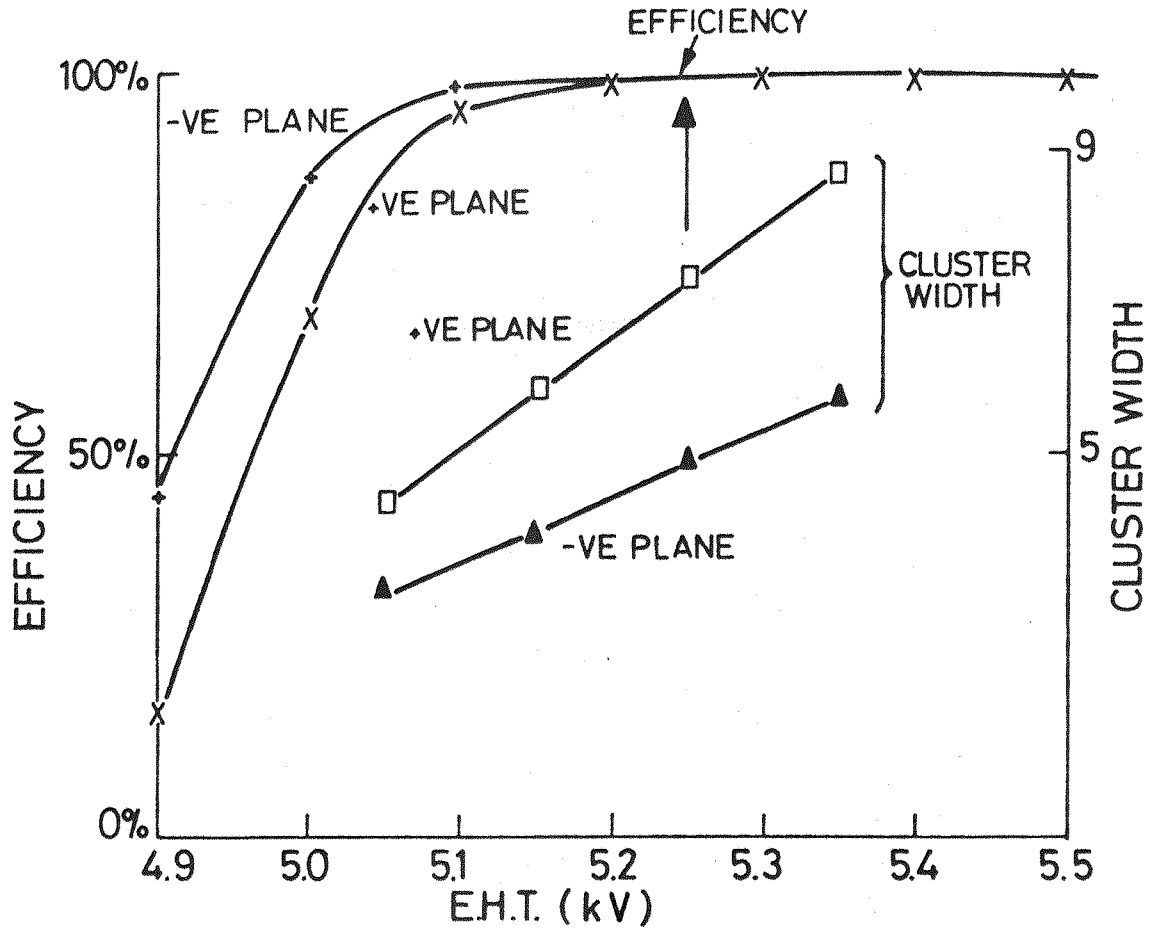

FIG. 4.9 DEPENDENCE OF S6A EFFICIENCY AND CLUSTER WIDTH ON E.H.T. VOLTAGE

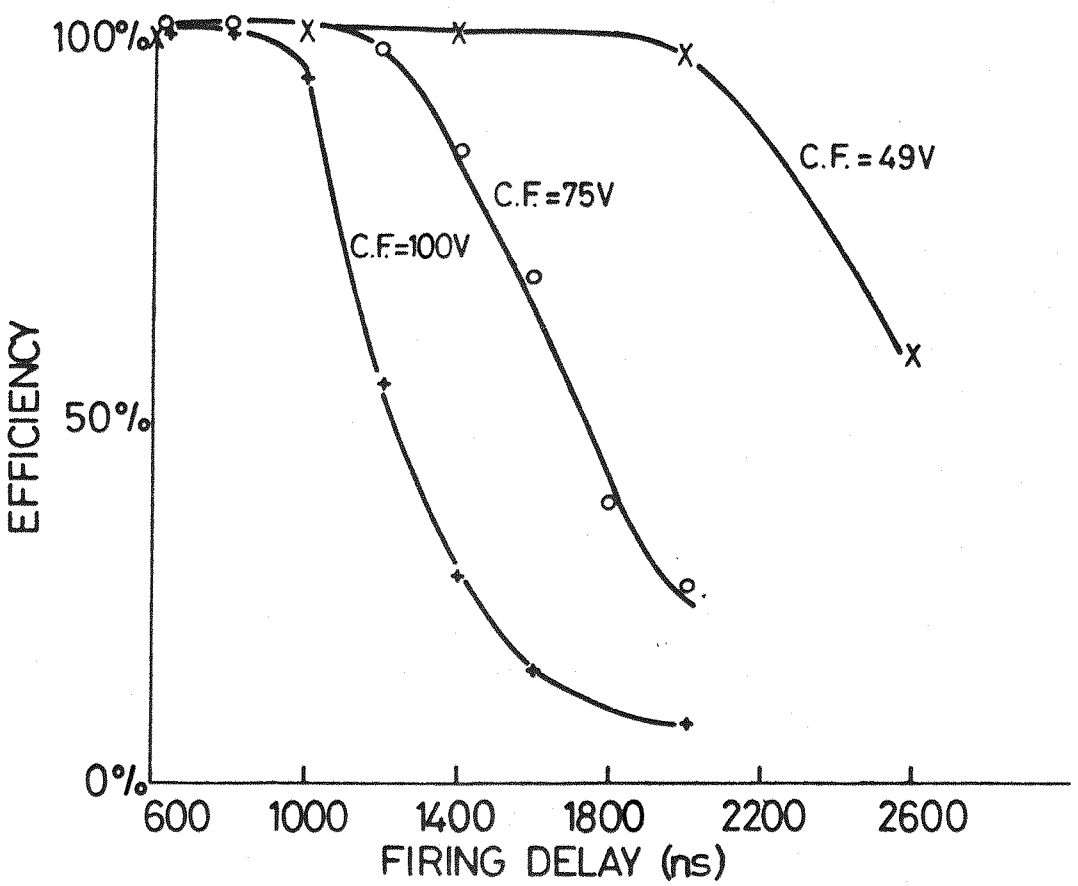

FIG. 4.10 DEPENDENCE OF S6A EFFICIENCY ON CLEARING FIELD AND FIRING DELAY

detected was in S3C where the efficiency fell to about 85% over part of its area.

After breakdown the spark current was shared between a cluster of neighbouring wires, the size of the clusters varying with the applied field (Fig.4.9). The efficiency of the chambers was also measured as a function of the delay in firing and the strength of the clearing field (Fig. 4.10). Efficiency fell when the delay approached the memory time of the chamber and the latter was reduced as the clearing field increased.

CHAPTER 5

Data Acquisition

5.1 Field Calibrations

Momentum analysis using the M205 and M505 magnets necessitated accurate calibration of their fields.

The M205 field was calibrated by the floating wire technique. The central field of the magnet, monitored by a Hall plate probe, was adjusted to deflect a current-carrying wire by 17.4° i.e. along the central ray of the beam. The nominal momentum corresponding to the central field was then inferred from the tension and current in the wire. Since the beam was well collimated all particles experienced essentially the same field and their momenta were determined directly, relative to the nominal value, from their incident and emergent trajectories. The accuracy of the floating wire measurements was estimated to be better than 0.5%.

Since the M505 magnet accepted scattered particles into all regions of its field volume extensive field maps were made, using Hall plate probes, to measure its uniformity. However for the purpose of momentum measurement the field was found to show good approximation to the rectangular field model. In this

model the field within the rectangle is assumed to be uniform and equal to the central value, B_o, and the length of the rectangle, known as the effective length of the field, is given by:

$$L = \int B \, dl \, / \, B_o \quad . \; . \; . \; . \; 5.1$$

Particle momenta were therefore determined, using the above field parameterisation, from their deflection as measured by the spark chambers.

A full discussion of the momentum measurements is given in Chapter 6.

5.2 Preparation Of Equipment

The D1 and D2 scintillators were supported in light-tight boxes with air-light guides and were each viewed by two photomultipliers, one on each side of the beam. The 'halo' was also viewed by two photomultipliers, to ensure good detection efficiency, these being connected to the scintillator via lucite light guides. The sideboard and hodoscope counters were each connected to a single photomultiplier by a perspex light guide and, together with the 'halo', were wrapped in black mylar to exclude all light. The operating voltages were determined using the beam by 'plateauing' in the usual way and the pulse heights were checked with

analogue to digital converters. The efficiency of each counter was found to be at least 99.9% but, in some elements, was observed to drop when the M505 field was turned on. The efficiency was restored on all hodoscope counters by screening their photomultipliers with thick mumetal sheaths and steel tubes.

The DISC Cerenkov operated by the requirement of a nine-fold coincidence between signals from its photomultiplier tubes. Thus photomultipliers with high quantum efficiency were used to optimise the detection efficiency.

The efficiency of the DISC was measured by recording the ratio D1.D2.DISC(9)/D1.D2 using a proton beam which was essentially free from background particles. From this result (56.6%) the detection efficiency for kaons was calculated to be 63.6% (Appendix2). The same measurements were made using a pion beam but with the DISC adjusted to identify kaons. In this way the pion rejection efficiency was measured, less than 1 in 10^4 pions being misidentified as kaons. To maintain this background rejection at high momenta, where the velocity separation of kaons and pions is reduced, it was found necessary to reduce the width of the iris by control of the diaphragm.

The momentum range of the kaon beam was covered

using cells of glycerol, heptane, ethanol and water.

On completion of testing procedures the counters, proportional chambers and spark chambers were surveyed into position in the beamline.

5.3 Trigger Logic

Signals from the scintillation and Cerenkov counters were processed by logic units to select candidates and to function as the trigger for the spark chambers. Analogue signals from the photomultipliers were discriminated to form digital pulses of adjustable length and association with a single event was established by detecting their time overlap in coincidence units.

The logic used to select candidates is illustrated in Figure 5.1. Signals from D2, in delayed coincidence with their complementary signals from D1, produced a master STROBE which defined the origin of the timing sequence. Variations in the relative timing of the D1 and D2 signals due to time-of-flight fluctuations, were accounted for by delaying D2 to well within a wider D1 pulse. In this way the timing of the STROBE was always determined by the arrival of particles at D2. After the production of each STROBE the experiment was 'paralysed'

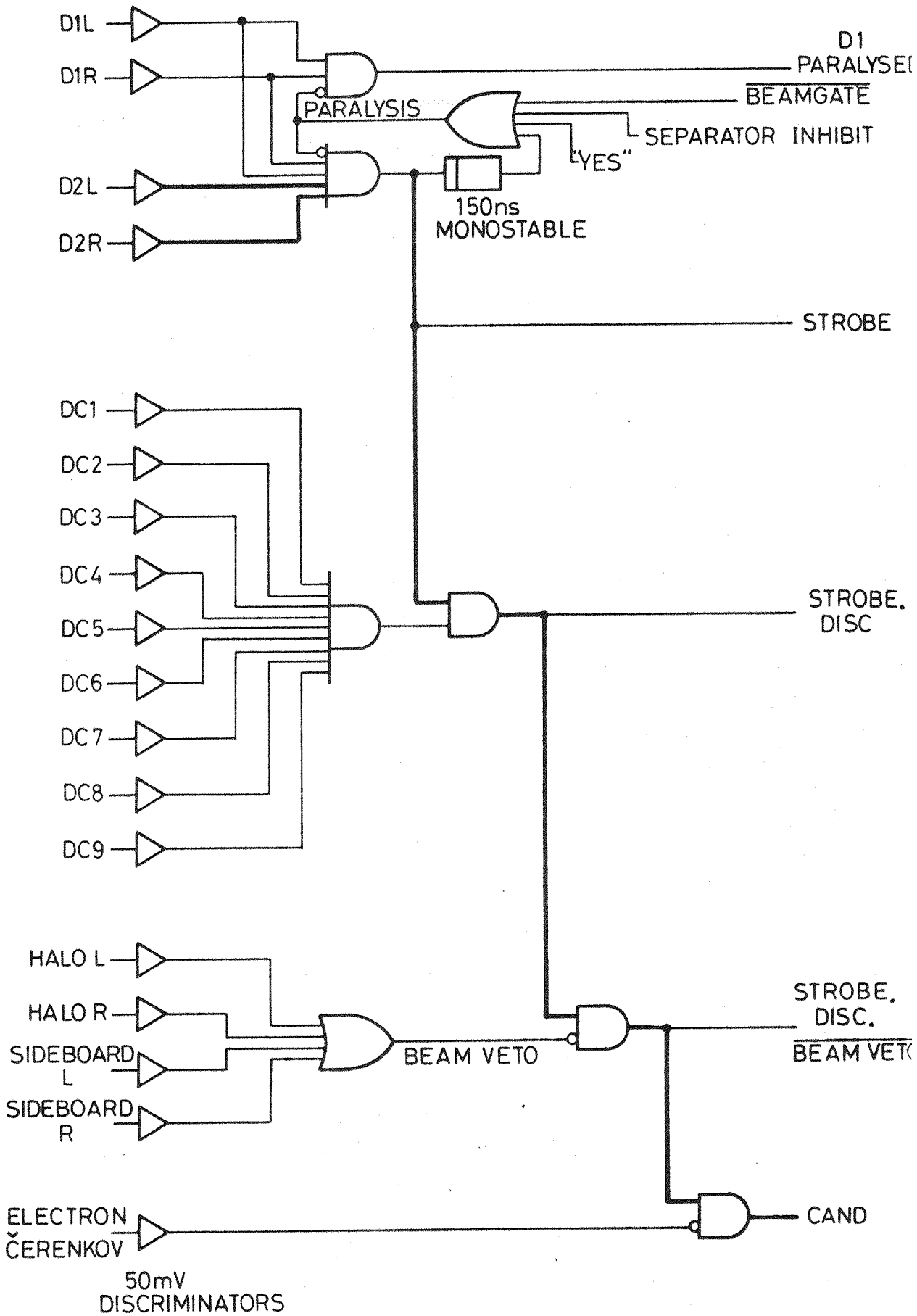

FIG. 5.1 BEAM COINCIDENCE LOGIC

for 150 nsec by inhibiting further D1.D2 coincidences. This provided enough time to identify candidates and to test the trigger requirement. Nine-fold coincidences from the DISC and veto signals from the halo, sideboards and electron Cerenkov were successfully brought into coincidence to finally produce the CANDIDATE pulse. Pulses at each coincidence level were scaled by CAMAC serial registers capable of counting input signals at rates up to 100 MHz .

Signals from the trigger arrays were fed into RL379 hodoscope units which were designed to shape photomultiplier pulses and to store gated outputs in a fast register. (Fig.5.2) The contents of the register could be read by a CAMAC-read operation. The register was reset by the leading edge of the next gate input or by a 'RESET' pulse generated by the trigger logic. Another facility provided by the units was the 'OR' output, taken from the register, which produced a pulse when data were present on any of the eight channels. The 'SINGLES' pulse provided an ungated output of the eight inputs and was therefore used to scale the total flux seen by the hodoscopes.

The function of these units in the trigger formation logic is shown in Figure 5.3. A different unit was used for each hodoscope, two units being required by

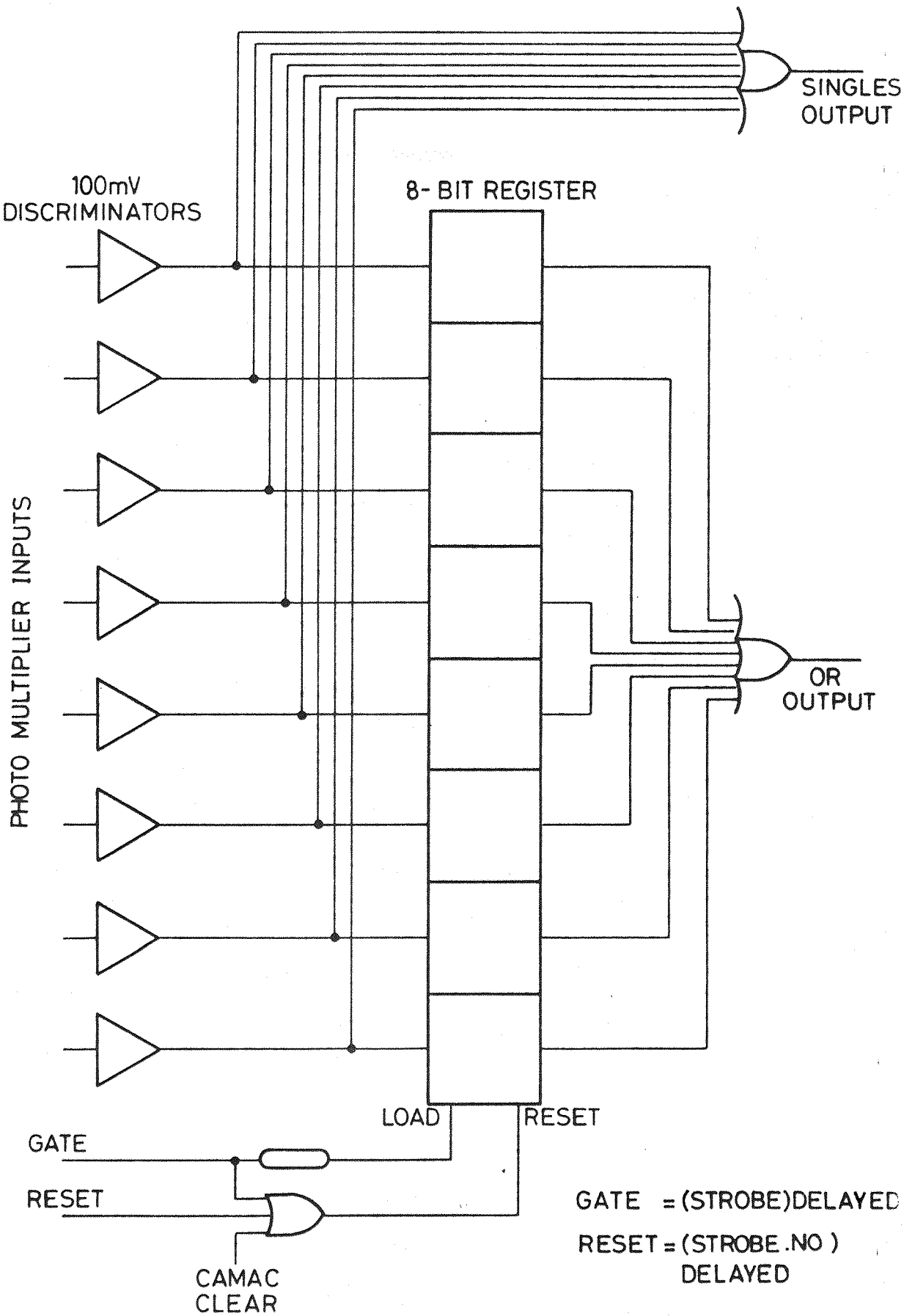

FIG. 5.2 SCHEMATIC DIAGRAM OF RL379 HODOSCOPE REGISTER UNIT

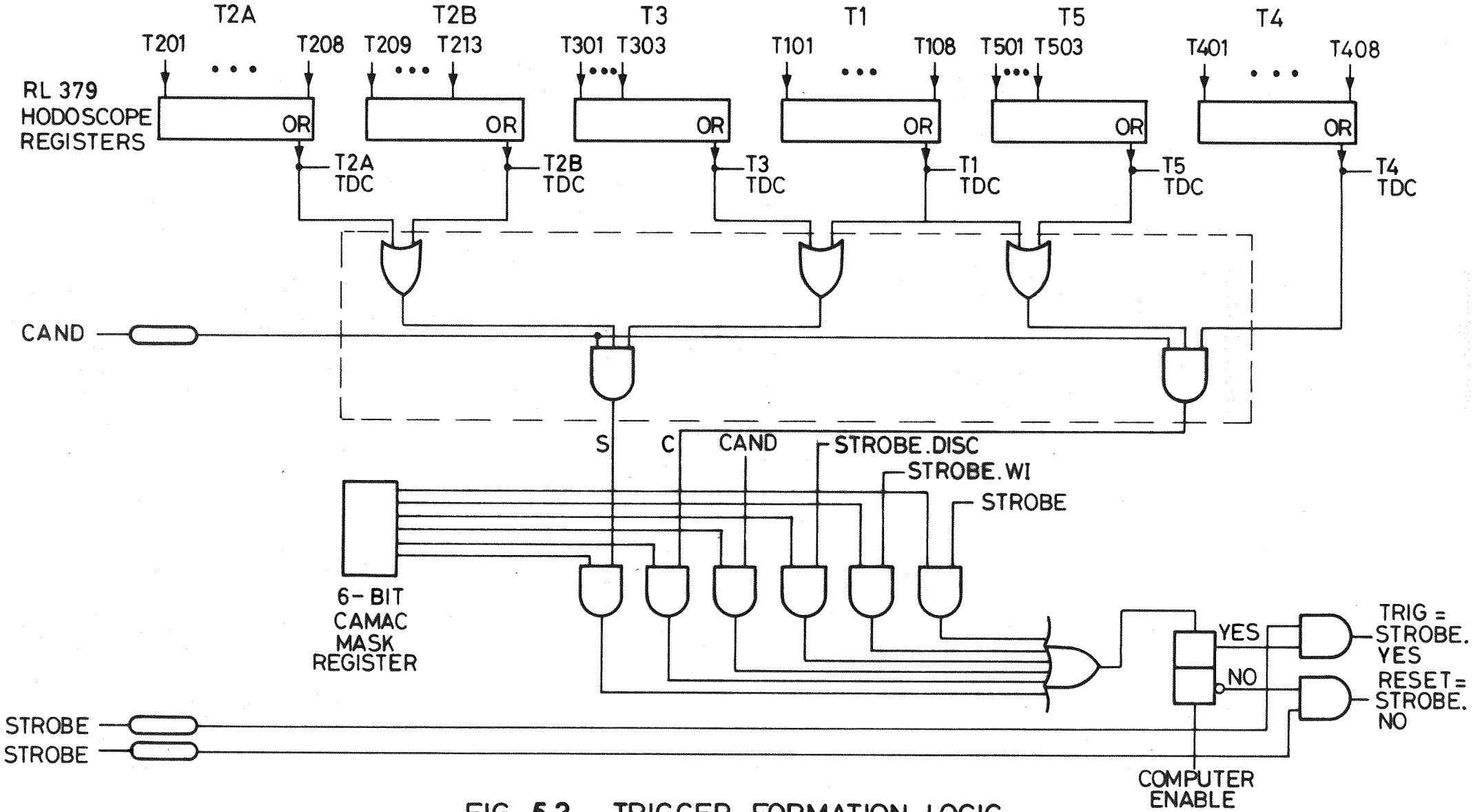

FIG. 5.3 TRIGGER FORMATION LOGIC

the thirteen elements of the T2 array. The width of the STROBE pulse used to gate the registers was different for each unit, being chosen to encompass time- of-flight variations within each counter array. The gated OR outputs were combined in the trigger selection unit (indicated by broken lines) to fulfil the S- and C-mode trigger requirements.

The trigger mode was selected from combinations of six different coincidences by control of a six-bit CAMAC mask register. The final decision, YES or NO was set in a bistable, which when gated with STROBE either produced a trigger pulse or a reset pulse. The YES level, as well as initiating the spark chamber firing sequence, was also used to paralyse the experiment by inhibiting the production of further STROBE signals. The paralysis was maintained until the chamber dead time had elapsed when the bistable was reset by the 'computer enable'.

The RESET pulse was used to clear the hodoscope and proportional chamber registers in preparation for the next event.

The photomultiplier pulses were also sampled by analogue to digital convertors (A.D.C.) to give a precise measurement of their amplitude (Fig.5.4). The signals were delayed to coincide with the gate which selected pulses only from trigger events for analysis. A

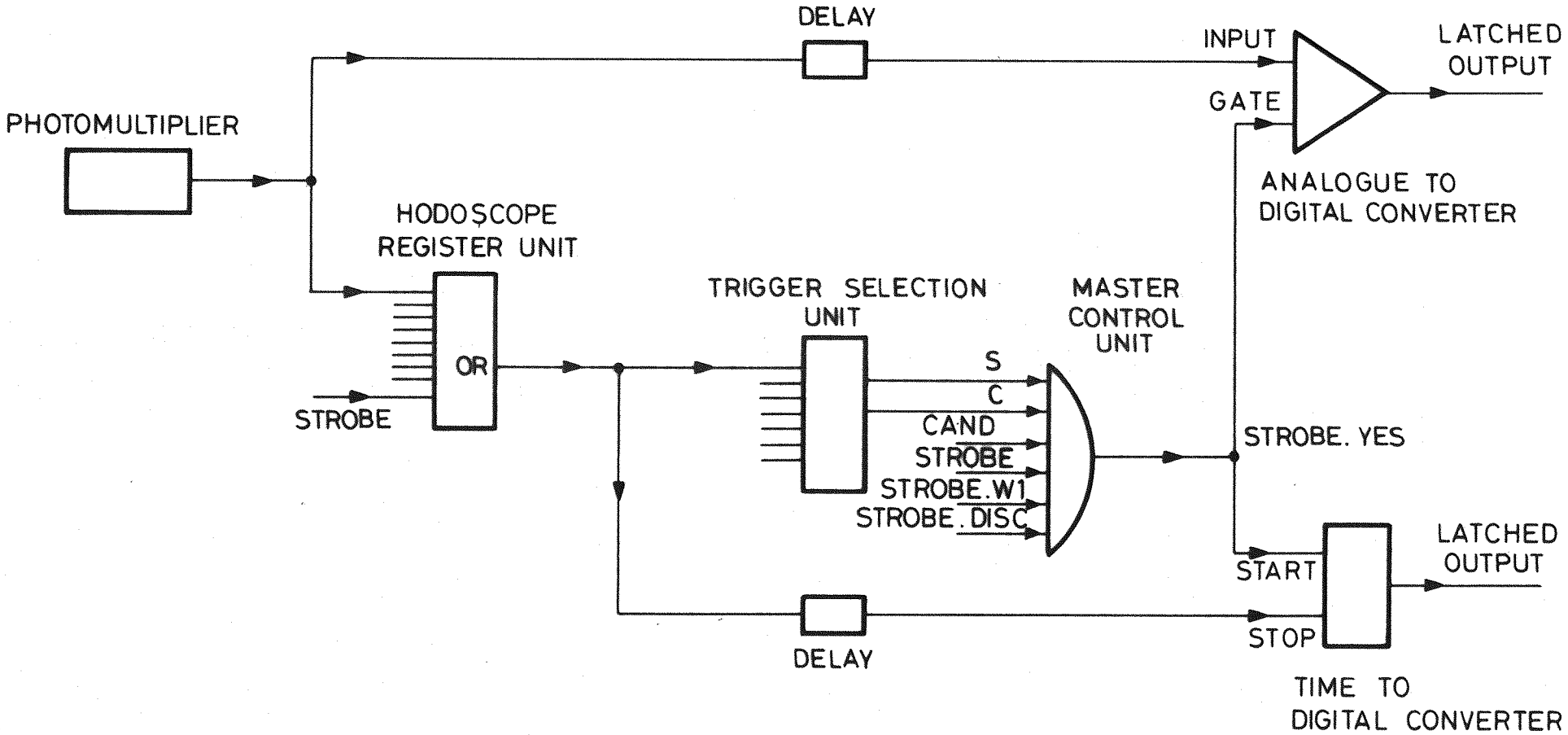

FIG. 5.4 CONNECTION OF ADC AND TDC UNITS TO THE HODOSCOPE ARRAYS

separate A.D.C. was used for each counter. The time interval between the passage of particles from D2 to each counter was deduced from measurements made by time to digital convertors (T.D.C.). These generated a binary digital output proportional to the time interval between the leading edges of 'start' and 'stop' timing signals. The precision of the measurement was largely governed by risetime and jitter in the signals which gave a resolution of approximately two nanoseconds. Since the pulses were taken from the hodoscope units only one T.D.C. channel was needed for each unit.

During data taking further paralysis was provided by a 'beamgate' and a 'separator inhibit'. The 'beamgate' was derived from the current rise in the NIMROD magnet ring and remained open for the duration of the burst. The 'separator inhibit' was generated by the loss of H.T. on the velocity separator and maintained for a short time during recovery.

5.4 On-Line Program

Data were recorded on seven-track magnetic tape using a PDP11/45 computer (PLATE 5). Standard features of this machine included a UNIBUS, which provided direct access to memory for peripheral devices, and an automatic priority interrupt system. Data transfers were

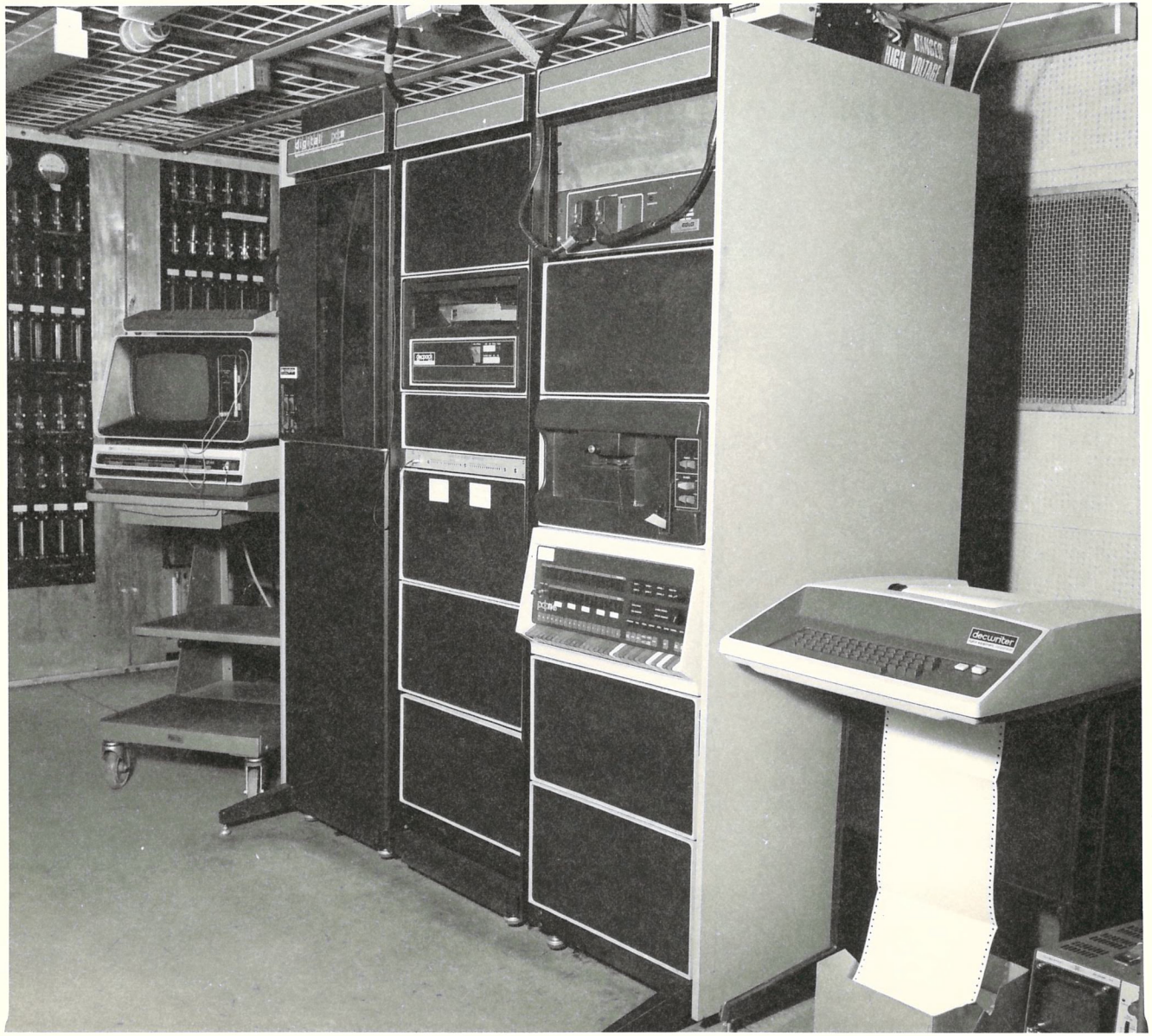

Plate 5 On - Line Computer

accomplished via two interfaces, one for CAMAC registers and a special interface used to read out the capacitive information.

An on-line program, KNULP, organised the retrieval of data, its control sequence being summarised in Figure5.5. At the beginning of each data run certain constants were set up to specify the run number and beam momentum, and to define the trigger mode. The latter was then selected during data-taking by masking the master control unit (M.C.U.) register. At the start of each burst the program received an interrupt from the beamgate unit and control was passed to the burst routine. An 'event interrupt' was generated by the trigger logic and this initiated the read-out sequence. S1/S7 data were read by program control whereas other CAMAC data, together with the capacitive data, were read by direct memory access (D.M.A.). During D.M.A. operations the C.P.U. performed preliminary anaysis of data already read into the memory buffer. The event was then written to tape and the computer idled until the spark chamber dead time had elapsed.

5.5 Data Collection

The proton flux in the X3 beam was monitored by a secondary emission counter (S.E.C.) and its steering

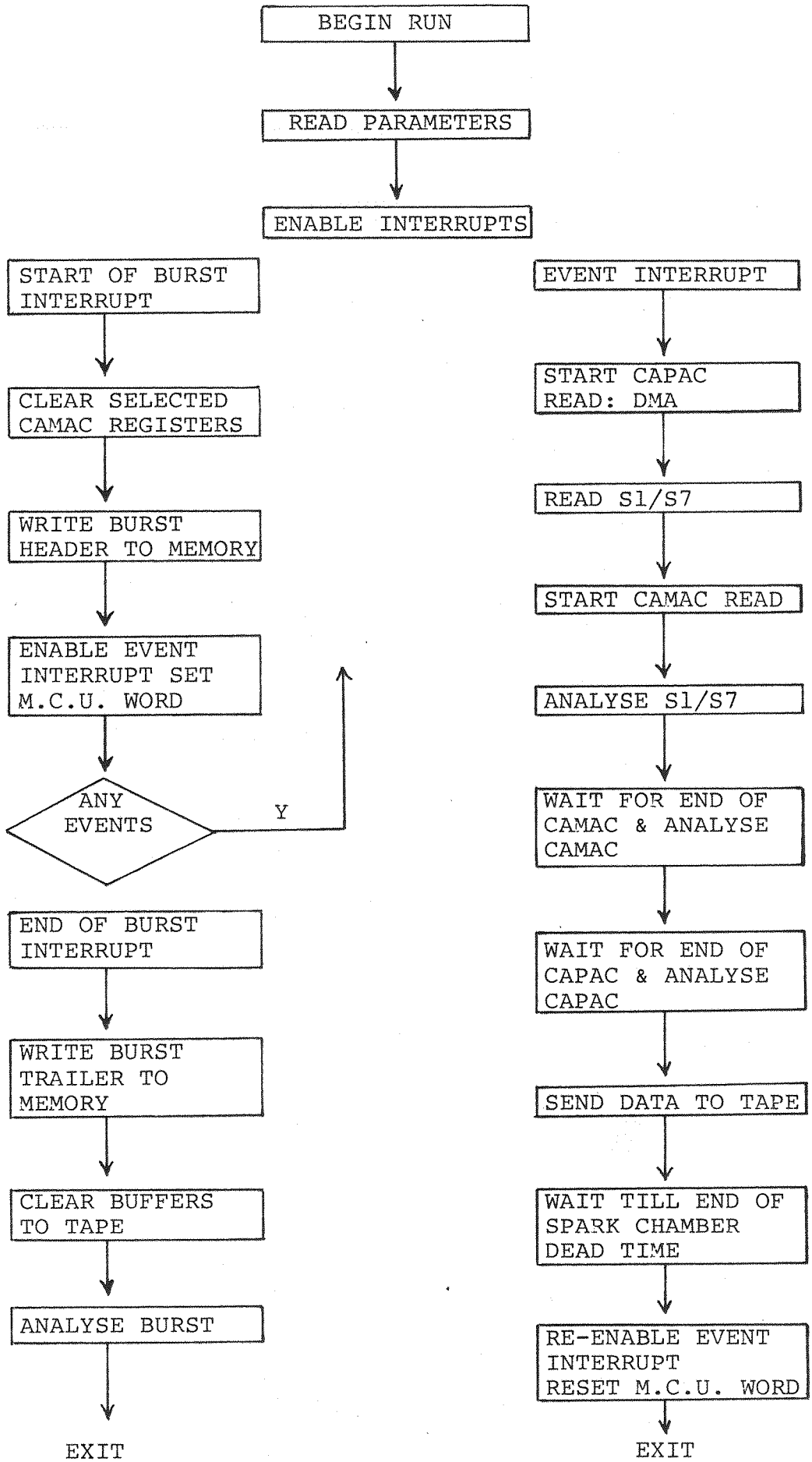

Fig. 5.5 FLOW CHART FOR THE ON-LINE PROGRAM, KNULP

onto the X3 target by a scintillation counter telescope (TMON.). These rates, together with coincidences from the beam counters, were displayed by scalars in the control room for quick assessment of beam conditions.

The following procedure was adopted for setting-up the beam at each momentum. Firstly the central fields of M205 and M505 were set to their calibrated values using a nuclear magnetic resonance (N.M.R.) probe. The appropriate cell was then mounted in the DISC and the axicon and S116 compensating magnet were scanned to locate the kaon peak. The operating currents of the remaining magnets, having been set initially to their programmed values, were now adjusted to optimise the kaon flux.

The total particle flux in the beamline was controlled by adjustment of the collimator apertures. The horizontal collimator was kept at ±15mm to provide a constant momentum bite (±2%). The vertical collimator was set initially to ±60mm at the low end of the momentum range but was progressively reduced as the velocity separation decreased. The blockhouse collimator was opened fully (±400mm) to maximise the beam intensity. Typical beam conditions are given in Table5.1.

Table 5.1 Particle flux measurements per Nimrod burst at 1372 MeV/c.

S.E.C.	1.9×10^{12}
TMON.	1.0×10^{4}
D1	2.5×10^{5}
STROBE	1.7×10^{4}
STROBE.DISC	875
STROBE.DISC.$\overline{(HALO+SB)}$	850
CANDIDATES	850

During data taking the M205 and M505 fields were monitored since the accuracy of the momentum measurements depended on their stability. M205 was monitored with the N.M.R. probe, which was accurate to ±0.05%, and M505 with magnetoresistive monitors having an accuracy of ± 0.1%.

At each momentum 500,000 events were recorded with the target full and a further 30,000 with the target empty. The basic event sample consisted of S- and C-mode triggers which were selected by suitable control of the M.C.U.. However, for every tenth event the CANDIDATE trigger mode was selected in order to record an unbiased sample of beam tracks. These beam tracks were subsequently used in a Monte Carlo program for computation of the acceptance of the detectors.

In addition 30,000 events were recorded, using the STROBE.W1 trigger mode, at the beginning and end of each NIMROD cycle as well as before and after the removal of any equipment. These events were used to check the alignment of the detectors and therefore were recorded using a proton beam.

CHAPTER 6

Data Analysis

Differential cross sections were produced by determination of two quantities.

(1) The angular distribution of elastic events selected from all triggers recorded on tape.

(2) Weighting factors for each bin evaluated from a Monte Carlo calculation of the acceptance of the apparatus.

In this chapter the treatment of the data will be described.

6.1 Introduction

Each tape of raw data was copied onto a 9 track high density tape for analysis on the Rutherford Laboratory I.B.M. 360/195 computer.

Analysis proceeded with the reconstruction of particle trajectories from the chamber data. Extensive use was made of a geometry 'data set' which contained the survey positions of all detectors. Changes in the chamber positions due to removal and replacement of equipment were calculated from the alignment runs and incorporated on the geometry 'data set' as corrections to the survey.

Providing sufficient information was available for the reconstruction of tracks an attempt was made to form a common vertex. By confining the vertex to a fiducial region within the liquid hydrogen it was possible to ensure that the scatter did not originate from components of the target vessel. The beam and S-mode trajectories were also used to compute particle momenta. These kinematic quantities, together with scattering angles determined from the inclination of tracks were sufficient to identify the elastic nature of events. For each event satisfying the selection criteria the elastic event count was incremented for the appropriate bin.

However some inelastic events conspire to resemble elastics and therefore contribute to a background under the elastic peak. This background was estimated by extrapolation of the event distribution outside the elastic peak.

Finally several factors having a potential effect on the normalisation of the data were considered and corrections made as appropriate.

6.2 Data Reduction

The program was organised to read raw data from tape, to fit tracks to the measured co-ordinates and to

copy track parameters and diagnosties associated with failures to a Data Summary Tape (D.S.T.). In the CANDIDATE trigger mode only the beam trajectory was reconstructed and this was copied to a temporary file for use in the acceptance calculation.

In addition information from the beam and trigger counters was examined and quantities relevant either to the differential cross section measurement or to the performance of the counters were copied to the D.S.T..

The track fitting procedures will now be considered in detail.

(i)The Beam

Information from the proportional chambers was decoded and trajectory co-ordinates were determined from the wire addresses and survey data. Straight lines were fitted to the measured points by the method of least squares. Since each chamber measured only one co-ordinate the X and Y planes had to be treated separately and the trajectory determined from its projection onto the horizontal and vertical planes. In addition, particle deflection in M205 and susceptibility to scattering in the cell of the DISC made it necessary to analyse each trajectory in three sections. Each section included various groups of chambers as specified in

Table 6.1.

Table 6.1 Arrays of proportional chambers used by the track fitting routines.

Section	Groups	Number of X Chambers	Number of Y Chambers
1	BA,BB	6	3
2	BC,BD	6	4
3	BD,BE	6	4

In order to contribute to the track fitting chamber data had to satisfy certain requirements.

(a) Data from chambers recording a ZERO or MULTIPLE status were ignored.

(b) A minimum of three valid points was required in each section of the track, otherwise the event was rejected.

(c) At least two points (1X and 1Y) from each group of chambers were required,to ensure an accurate fit.

Occasionally spurious points were recorded by the chamber electronics which appeared to bear no relation to the track direction. When included in the fit a point of this type distorted the reconstructed trajectory. To avoid this a limit was imposed on the residual distance of a point to the fitted line. If the limit was exceeded the chamber with the maximum residual was eliminated and

the line fitted to the remaining points. This process was continued until either the fit was successful or until there were insufficient valid points left to satisfy the track fitting requirements.

The momentum of beam kaons was determined from the track parameters of sections 1 and 2. The horizontal component of momentum (P_H), was calculated relative to the central momentum of the beam (Po) from:

$$\frac{P_H}{P_o} = \frac{2\sin(\theta/2)}{\sin\alpha_{in} + \sin\alpha_{out}}$$

and the total momentum (P) from:

$$P = P_H\sqrt{\frac{(1 + m_x(2)^2 + m_y(2)^2)}{1 + m_x(2)^2}} \quad \ldots\ldots 6.1$$

where θ is the fixed deflection of the central ray (i.e. 17.4°)

αin (αout) is the entry (exit) angle of the track in the horizontal plane.

$m_{x,y}$ (1,2) is the X(Y) gradient of the track in section 1(2).

A typical momentum distribution determined in this way is presented in Figure 6.1.

An estimate of the imprecision of the reconstructed trajectory was made from the residuals determined in the fitting procedure. This resolution

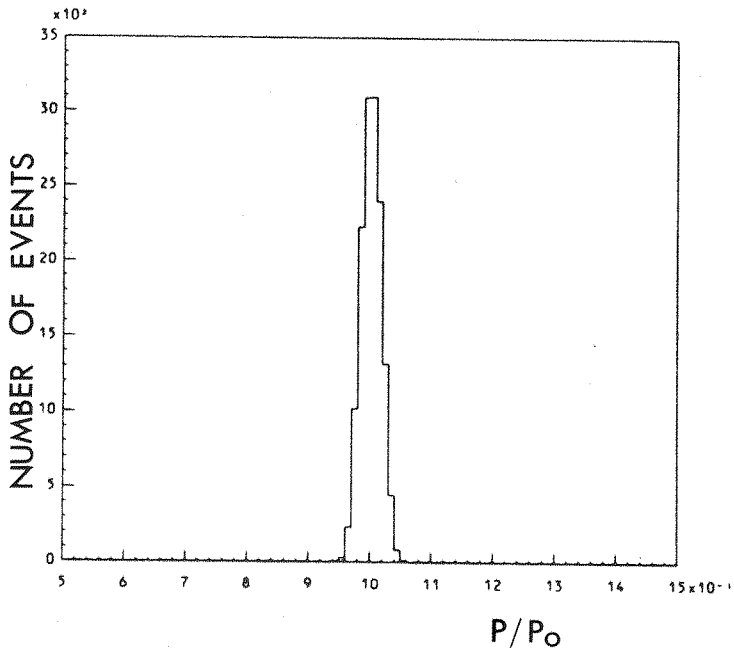

FIG. 6.1 NORMALISED BEAM MOMENTUM

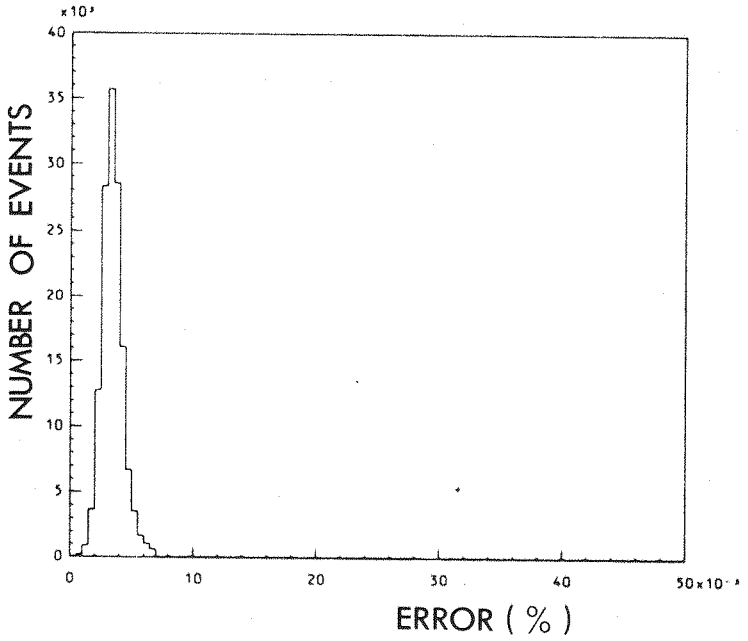

FIG. 6.2 ERROR IN BEAM MOMENTUM

contributed a random error to the measured momentum (Figure6.2). In addition there were three principal sources of systematic error in the momentum determination, namely:

(a) The accuracy of the floating wire measurements, which was estimated to be ±0.5%.

(b) The stability of the M205 field which was constantly monitored to within ± 0.05% by N.M.R..

(c) An unknown systematic effect due to possible inaccuracies in the chamber survey.

A check on the momentum calibration was made by measuring the range of 1 GeV/c protons in copper absorber. Results taken from range-energy relations were found to be consistent, within the estimated errors (±0.5%), with the measurements obtained from equation 6.1. (Appendix3).

Scattering in the cell of the DISC was identified from the track parameters of sections 2 and 3. The change in direction was required to be less than 20 mrad or the event was rejected. Further cuts were imposed on both the momentum, for which only values within 6% of the central value were permitted, and on the estimated error in momentum, which was required to be less than 0.7%. If successful the incident trajectory, defined by the track parameters of section 3, was accepted and

analysis proceeded to the identification of scattered particle trajectories.

(ii) Track Finding in the Spark Chambers

For the purposes of track reconstruction the chamber modules were combined in three groups (Table6.2) and where possible a track was fitted through the measured co-ordinates in each group. Spark co-ordinates were evaluated for all combinations of wire clusters on opposing planes, subject to the reconstructed spark lying within the fiducial area of the chamber. In general, the long memory time of the spark chambers resulted in more than one cluster per trigger on each plane, which complicated the identification of tracks.

Table 6.2 Arrays of spark chambers used by the track fitting routines.

Group	Spark Chamber Modules	Maximum Number of Points in Track
1	S1(S7),S2	5(6)
2	S3,S4	6
3	S5,S6	6

In the case of groups 2 and 3 the track finding proceeded by the formation of links between sparks on neighbouring chambers and track recognition was

established by the imposition of colinearity constraints on the chain of links so formed. A straight line was then fitted to the measured points providing at least three sparks were found with at least one spark coming from each chamber module.

This procedure resulted in the possibility of recording several tracks in a single event. The tracks, were therefore classified according to their 'goodness of fit' and, for both groups, up to five of these were stored on the D.S.T. for subsequent analysis.

In the case of group 1 a different philosophy was adopted. Use was made of the short resolution time of the S1 and, where applicable, S7 proportional chambers to preferentially select sparks from a limited region on S2. This region was selected from the projection onto S2 of tracks found in S1. Again up to five tracks were accommodated on the D.S.T.

6.3 Event Selection

The event selection programs were organised to read data in DST format and to store on the DST parameters associated with the geometric and kinematic fitting. The distribution of elastics for each run was written to a separate record on a special 'data-set' (DCS), which was designed to contain all information

neccessary for the computation of the differential cross sections.

Event selection proceeded as follows.

(a)Vertex Reconstruction

An attempt was made to locate the scattering centre by reconstructing the vertex of the beam track and scattered particle tracks. In general the tracks were non copunctual because of multiple scattering and the finite resolution of the detectors. The vertex was therefore defined as being that point from which the sum of the squares of the distance to the measured track was a minimum. The root mean square (R.M.S.) of these distances was used as an estimate of the quality of the vertex.

Where possible both left and right scattered tracks were used in conjunction with the beam track to define the vertex. Each combination of left and right tracks found by the track finding routines was considered and the combination producing the best vertex was selected. However, if the R.M.S. of this vertex (Figure6.3) exceeded 8mm the fit was classified as a failure. For those events having an S-mode trajectory an attempt was made to form a vertex from the beam track and left track only. Again a limit was placed on the

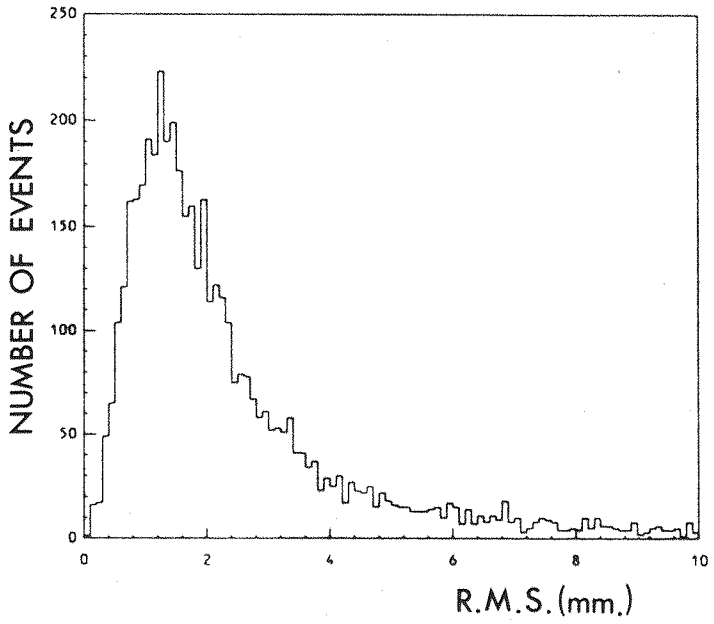

FIG. 6.3 R.M.S. FOR C – MODE VERTICIES

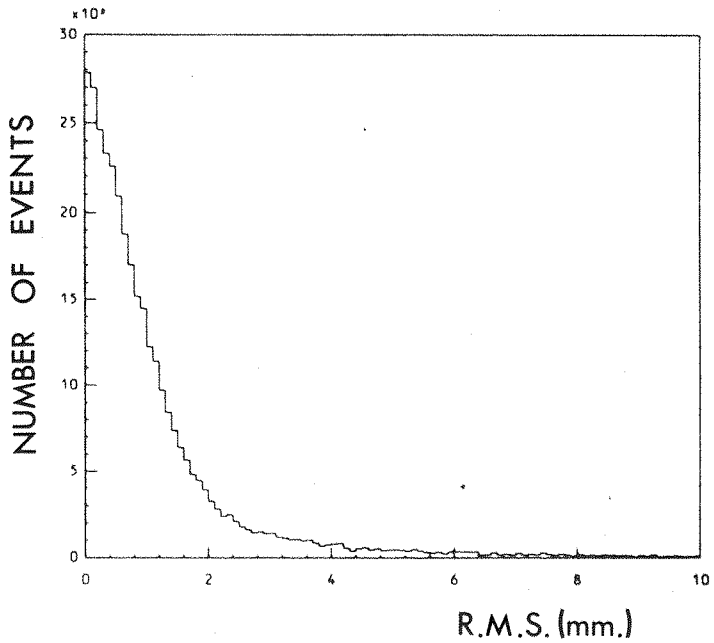

FIG. 6.4 R.M.S. FOR S–MODE VERTICIES

R.M.S. (8mm.) and if this was exceeded the event was rejected. (Figure6.4)

The distribution of vertex positions for C-mode events gives an indication of the quality of the track reconstruction (Fig.6.5). The target position and length are well reproduced and regions corresponding to the D2 scintillator and target vessel windows are clearly visible. Scatters not originating in the liquid hydrogen were excluded by placing cuts on the vertex position. However that region from which the scatter could be unambiguously assigned to a collision with the hydrogen depended on the resolution of the vertex reconstruction. The size of the fiducial volume was therefore chosen on the basis of target empty data where the extent of these components could be clearly measured.

S-mode verticies were relatively poorly constrained and the resolution of the vertex varied with the inclination of the scattered track. Below a scattering angle of 7° the fiducial volume had to be reduced to allow for a broadening of the regions corresponding to the target windows. Below 3° the vertex position was completely unreliable and so all events in this range were rejected. This placed a limit on the acceptance of the experiment in the forward and backward directions.

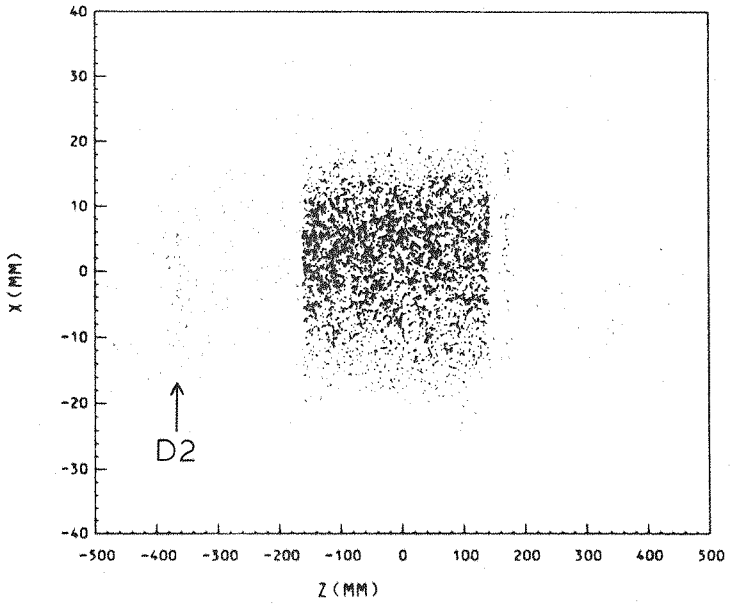

FIG. 6.5 RECONSTRUCTED VERTICIES FOR C-MODE EVENTS

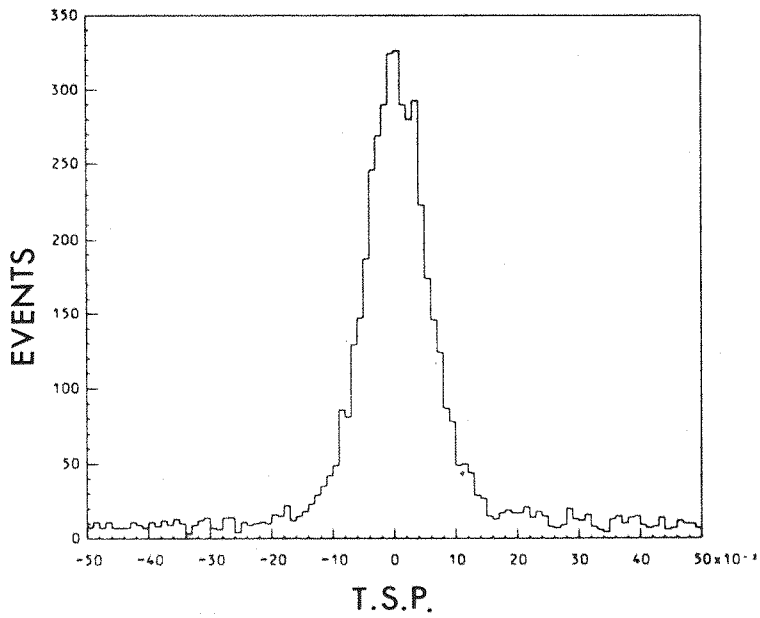

FIG. 6.6 TRIPLE SCALAR PRODUCT

If the vertex reconstruction was successful the scattering and azimuthal angles of the scattered particles were determined relative to the incident beam track. The coplanarity of C-mode events was also investigated by determination of the triple scalar product (T.S.P.) of unit vectors along the three track directions (Fig.6.6).

(b)M505 Momentum Measurement

The best GROUP 1 track, selected by the vertex reconstruction, was used in conjunction with each of the tracks found in GROUP 2 to determine the momentum of the observed particle. The two parameter rectangular field model (Equation5.1) was used for the M505 magnet and the momentum (P) was given by:

$$P = \frac{L\ B_o\ 0.0003}{\sin\alpha_{in} - \sin\alpha_{out}} \times \frac{1}{\cos\phi}$$

L and B are the effective length and central field of the model field.

α_{in} (α_{out}) is the entry (exit) angle of the trajectory in the horizontal plane

ϕ is the inclination of the ingoing track to the horizontal plane.

The momentum was checked for self consistency by assigning it to the measured track in group 1 which was

then retraced through the magnet using the model field. The position and direction of the emerging trajectory at the exit window of the magnet were then compared with those of the track measured by the group 2 spark chambers. The limits imposed on the discrepancies in the horizontal (Δx) and vertical (Δy) positions (Fig.6.7&Fig.6.8) and in the vertical inclination ($\Delta\beta$) (Fig.6.9) were:

$$\Delta x < \pm 30.0 \text{ mm.} \quad \Delta y < \pm 35.0 \text{ mm.} \quad \Delta\beta < \pm 25 \text{ mrad.}$$

This procedure was repeated for each group 2 track with the best combination, satisfying the above constraints,being selected on the basis of the following distribution:

$$\chi^2 = \left(\frac{\Delta x}{\sigma_x}\right)^2 + \left(\frac{\Delta y}{\sigma_y}\right)^2 + \left(\frac{\Delta\beta}{\sigma_\beta}\right)^2$$

Here $\sigma_{x,y,\beta}$ are the widths of their respective distributions.

The momentum corresponding to the successful trajectory was finally corrected for energy loss between the target and M505 axis to give the particle's momentum at the vertex.

(c)Kinematic Selection

Those events processed successfully by the vertex and M5 tracking routines were finally subjected to

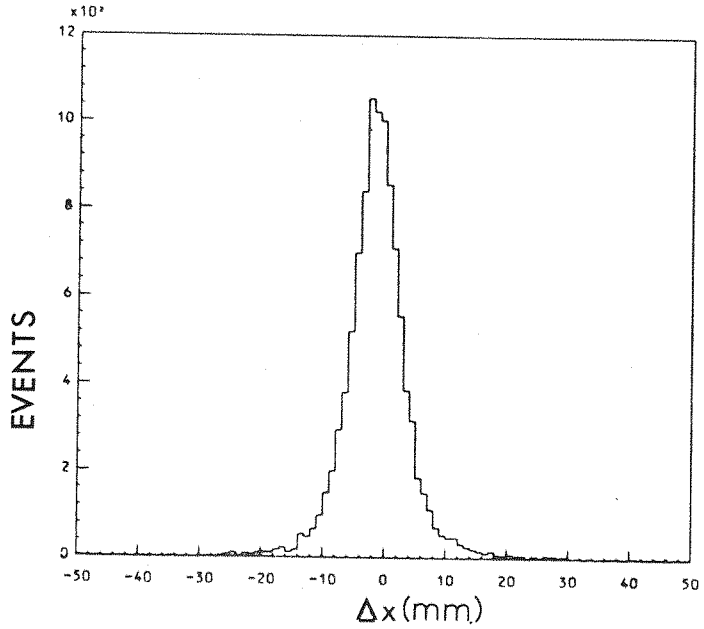

FIG. 6.7 HORIZONTAL DISCREPANCY AT M5 EXIT WINDOW

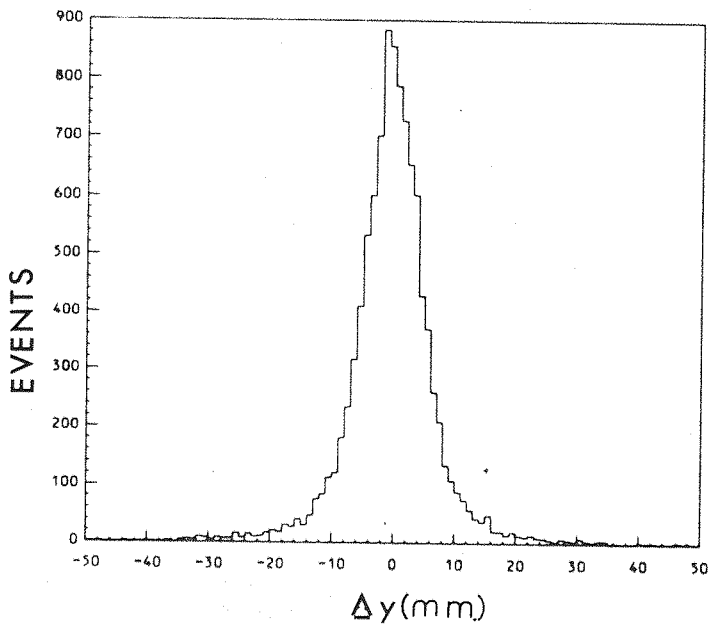

FIG. 6.8 VERTICAL DISCREPANCY AT M5 EXIT WINDOW

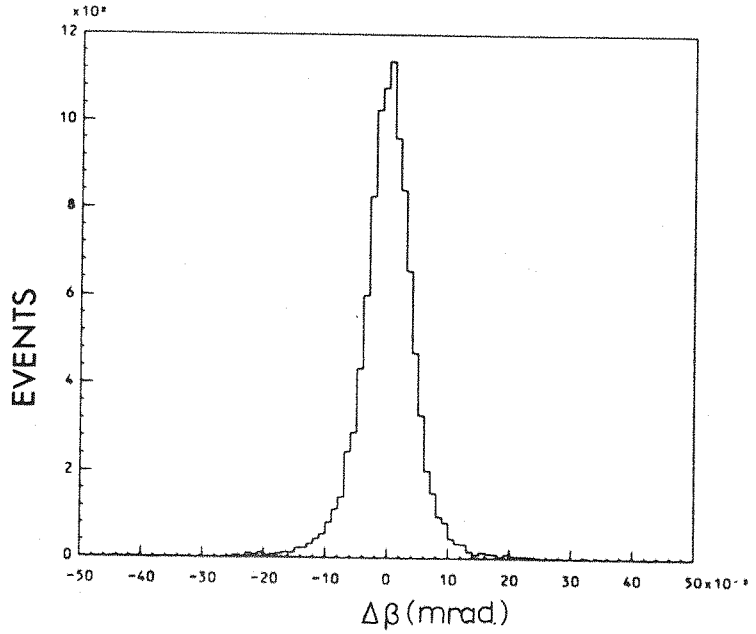

FIG. 6.9 VERTICAL INCLINATION DISCREPANCY AT M5 EXIT WINDOW

kinematic selection. The association of particle type with the measured tracks enabled the centre of mass scattering angle to be determined. Different hypotheses were tried by assigning the kaon or proton to a particular track and predicting the correlated quantity (i.e. either second angle or momentum). The best hypothesis was selected on the basis of the agreement between the measured and predicted quantities.

A plot of left vs. right scattering angle for C-mode events displayed two distinct bands corresponding to the kaon scattering elastically to the left or to the right (Fig.6.10). Particle assignment was therefore equivalent to finding the nearest curve to the point corresponding to the measured angles. Inelastic events were rejected on the basis of the distance of the point from this curve, known as the kinematic angular difference (K.A.D.-Fig.6.11). A limit of 3° was placed on the K.A.D..

The coplanarity of the three measured tracks was also used to reject inelastic events. This constraint was applied by requiring the T.S.P. of each event to be within ± 0.025 rad..

A lower limit of 420 MeV/c was placed on the proton momentum since below this value the particles were subject to large fluctuations in energy and

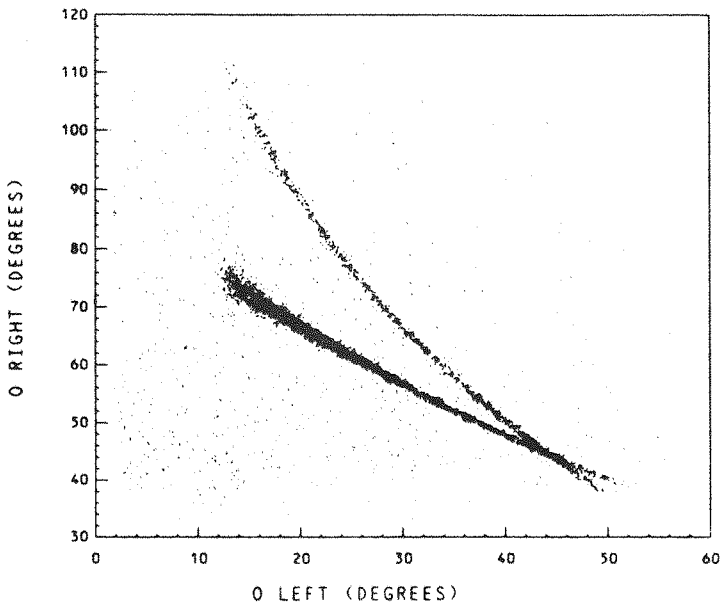

FIG. 6.10 ANGULAR CORRELATION FOR C-MODE EVENTS

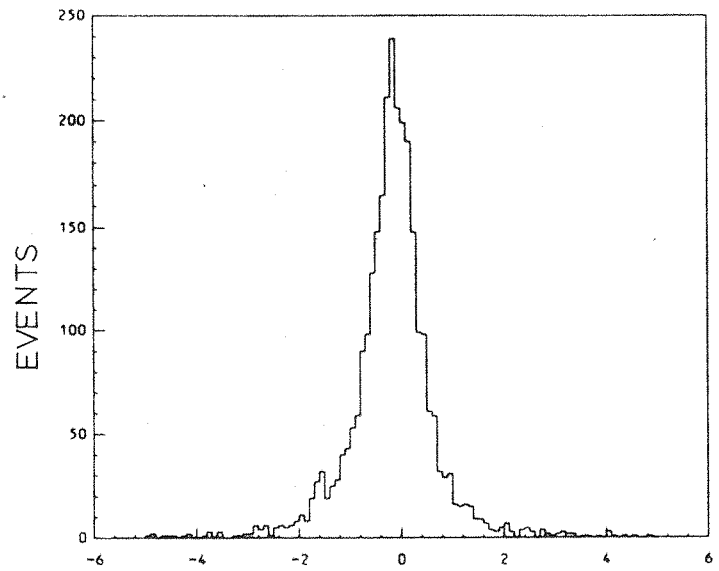

FIG. 6.11 KINEMATIC ANGULAR DIFFERENCE

direction such that they were not reliably detected. This constraint meant that events were counted only over the angular region for which the acceptance could be accurately determined (cf. Chapter7).

For S-mode events predictions of the kaon and proton momentum were made from the scattering angle and compared to the observed momentum. The elastic kaon and proton signals were easily distinguished as can be seen from the momentum-scattering angle correlation (Fig.6.12). In addition, bands corresponding to muons and pions arising from two body decays of kaons in the region of the target were also clearly visible. Events of this type were only observed in the S-mode configuration as the complementary decay products ($\vec{\nu}s$ and π°'s) were not detected. Events not conforming to elastic kinematics were rejected by placing a limit of ±4% on the kinematic momentum difference (Fig.6.13). However at small scattering angles the muons become indistinguishable from the elastic kaons and so all events in this region had to be rejected. This set the upper limit to the angular coverage in the forward direction which varied from a $\cos\theta^{*}$ of 0.94 at 1,000 MeV/c to 0.98 at 2,000 MeV/c.

Events producing both a C- and S- mode trigger simultaneously were rejected only if both constraints

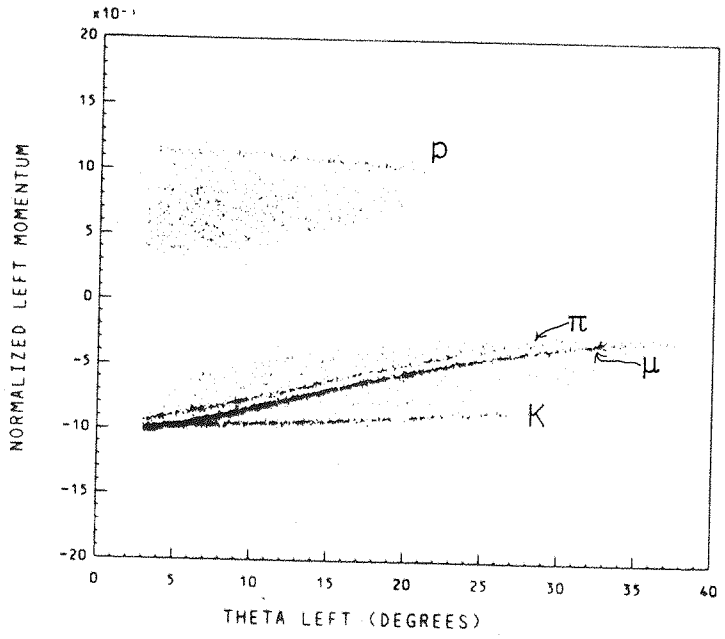

FIG. 6.12 MOMENTUM-ANGLE CORRELATION FOR S MODE EVENTS

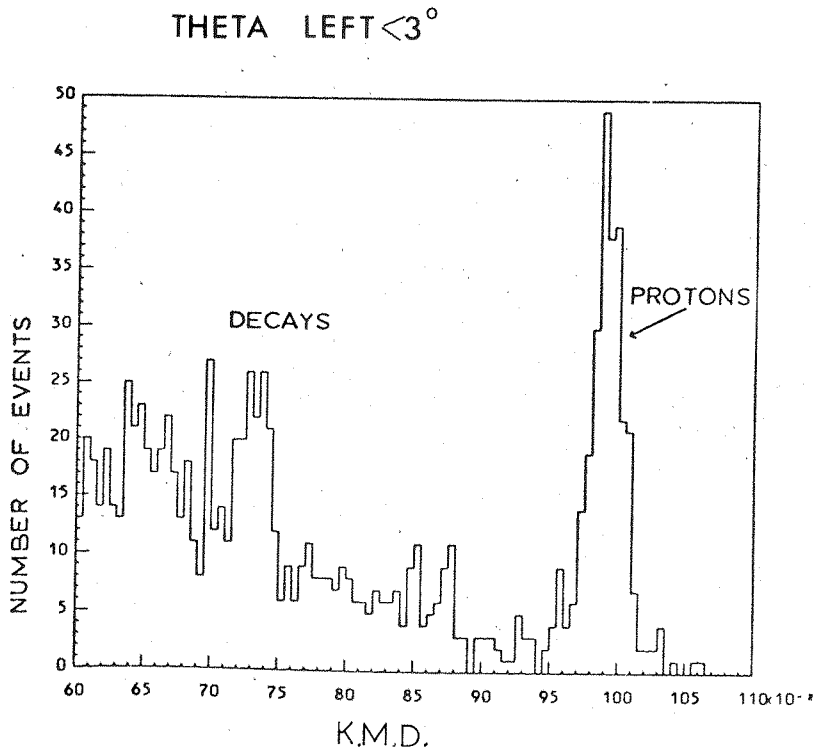

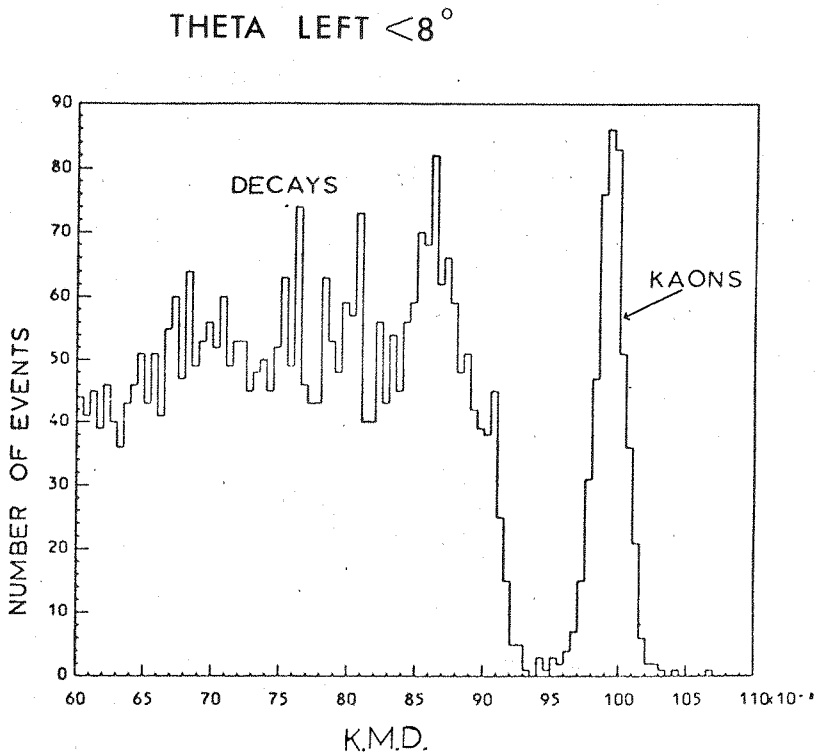

FIG. 6.13 KINEMATIC MOMENTUM DIFFERENCE

failed their individual cuts. If only one constraint failed the kinematic fit was classified according to the successful correlation.

A summary of event losses for a typical run is given in Table 6.3

6.4 Background Subtraction

The non elastic background lying under the elastic peak may be estimated by extrapolation of fits to the distribution of events outside the elastic region. However, the results presented in Chapter 8 are preliminary and do not include this correction.

Approximate estimates for the C- and S- mode backgrounds may be made by inspection of the relevant histograms. The T.S.P. distributions contain backgrounds of approximately 3% at 1212 MeV/c, rising to 8% at 1683 MeV/c. Preliminary checks indicate that they are independent of $\cos\theta^*$. The K.M.D. distributions for S-mode events indicate a background of less than 2% for the elastic kaon and approximately 6% for the recoil proton.

6.5 Corrections To The Data

Several corrections were applied to the data to obtain absolute normalisation of the differential cross

TABLE 6.3 EVENT PROCESSING DETAILS FOR A TYPICAL RUN AT 1283 MeV/c

(1)	TOTAL NUMBER OF TRIGGERS	32,005
	(a) TRIG = CANDS	3,360
	(b) TAPE LOSSES	51
	(c) C - MODE	3,034
	(d) S - MODE	24,696
	(e) BOTH S- AND C - MODES (B)	870
(2)	TRIGGERS LEFT AFTER BEAM PARTICLE TRACK FINDING LOSSES AND CUTS ON P, ΔP, AND SCATTER IN 'DISC'	24,934
(3)	TRIGGERS LEFT AFTER TRACK FINDING LOSSES IN SPARK CHAMBER SECTIONS	7,566
	(a) C - MODE	782
	(b) S - MODE	6,297
	(c) B - MODE	487
(4)	TRIGGERS LEFT AFTER KINEMATIC SELECTION i.e. NUMBER OF ELASTICS	911
	(a) C - MODE	351
	(b) S - MODE	413
	(c) B - MODE	147

sections. The corrections considered were:

(i)Beam Candidate Normalisation

For certain events the reconstruction procedure was not attempted:

(a) Events for which the beam proportional chambers failed to record a satisfactory beam trajectory.

(b) Events for which the momentum, error in momentum, and scatter in the 'DISC' of the beam kaon were outside the acceptable limits.

(c) Events associated with 'CANDIDATE' triggers, which were used only in the acceptance calculation.

(d) Events for which the record on magnetic tape contained parity errors.

The number of CANDIDATES recorded by the scalar registers was corrected for these events by subtracting from the running total the number of CANDIDATES recorded since the previous event. This modified total was used in the calculation of the differential cross section.

(ii)Beam Contamination

The tests described in Chapter 5 demonstrated the high pion rejection efficiency of the DISC Cerenkov (>99.9%). The primary source of beam contaminants therefore arose due to the decay or absorption of kaons between the DISC and the target. These processes are

most easily treated by Monte Carlo technique and were therefore incorporated in the acceptance calculation. Decay and absorption of the reaction products were also corrected in this way.

(iii)Detector Inefficiencies

The efficiency of the scintillation counters forming the trigger hodoscope T1 to T5 was measured to be close to 100%.

The spark chamber efficiencies were typically greater than 95%. However the redundancy provided by the groups of modules in each segment produced essentially 100% tracking efficiency.

Thus no correction to the results was applied for detector inefficiencies.

CHAPTER 7

The Acceptance

7.1 Introduction

The experiment was designed to cover only a part of the scattering region (Chapter 2). Consequently the measured distribution of events represents only a fraction of the total number of elastic collisions produced in the target.

The proportion of elastic events sucessfully identified by the apparatus depended on the following:

(a) The geometry of the detectors.

(b) The profile of the beam.

(c) Processes such as decay and absorption that lead to the loss of genuine elastic events.

These factors collectively determine the detection efficiency for elastic events which is normally referred to as the acceptance of the apparatus. An accurate estimate of the acceptance was essential to the measurement of the differential cross section.

Calculation of the acceptance involved calculation of the probability function P; this represents the probability of an elastic event being detected by the

trigger counters and of the trajectories reconstructed from the chamber data satisfying the selection criteria. The function depends on many variables since there are many physical effects that contribute to the developement of the particle trajectories. However the acceptance is required only as a function of the centre of mass scattering angle (θ^*) and so any explicit dependance on other factors must be eliminated by integration.

The acceptance is largely governed by the size of the detectors. If other processes are ignored the probability function depends merely on the direction of the scattered particles. In this approximation, and assuming the incident beam is collimated along the beam axis, the acceptance is given by the expression derived in Appendix1; this represents the solid angle covered by the detectors averaged over the length of liquid hydrogen (L_t):

$$A(\theta) = \int_0^{2\pi} \int_{l_1}^{l_2} \frac{P(\theta, \phi, l)}{2\pi L_t} \, d\phi \, dl \quad \ldots\ldots \quad 7.1a$$

A better estimate is achieved, however, if the probability function is averaged over the position ($\underline{x}$) and momentum ($\underline{p}$) distributions of incident kaons at the final beam counter:

$$A(\theta^*) = \int_0^{2\pi} \int_{l_1}^{l_2} \int_{\underline{x},\underline{p}} \frac{P(\theta^*, \phi, l, \underline{x}, \underline{p})}{2\pi L_t} \, d\phi \, dl \, d\underline{x} \, d\underline{p}$$

This equation produces too high an acceptance since distorted trajectories, particularly when produced as a result of decay or absorption, lead to the rejection of genuine elastic events. These modifications have to be considered particularly carefully as not all events experiencing them will necessarily be lost. Improvements of this sort make the integral extremely complicated and so if a reliable value for the acceptance is required analytic methods cannot be used. However this type of calculation is ideally suited to the so called 'hit or miss' Monte Carlo technique.[30]

7.2 Application Of Monte Carlo Technique To The Acceptance Calculation

This section firstly contains a description of how the simple integral of equation 7.1(a) can be evaluated by the Monte Carlo method and then shows how the processes that modify the results may be introduced into the calculation.

The method is based on the direct computer simulation of the scattering process. For each generated event the scattering parameters $(\theta^*_i, \phi_i, l_i)$ are chosen randomly, within their limits, using a numerical

algorithm for producing an even distribution of random numbers. Tests are then applied to determine whether the scattered particle trajectories intercept the counter hodoscopes. Those particles reaching the entrance aperture of the M5 magnet can be traced through the field using the two component field model. The probability function $P(\theta_i^*, \phi_i, I_i)$ is defined to be either 1, if the struck counter combinations satisfy the trigger selection criteria, or 0, otherwise. The expression for the acceptance becomes, in this approximation:

$$A(\theta_j^*) = \sum_{i=1}^{N_t} P(\theta_j^*, \phi_i, I_i) \frac{}{N_t}$$

where N_t is the total number of trials and A has again been normalised to lie between 0 and 1.

However the acceptance is required in terms of weighting factors (Appendix 1) since the results are binned in small intervals of $\cos\theta^*$. If $\bar{A}_j$ is the mean acceptance for bin j, which has width $\Delta\cos\theta_j^*$, then the weight for that bin is given by

$$W_j = \bar{A}_j \, \Delta\cos\theta_j^* \quad . \quad . \quad . \quad . \quad 7.1$$

The standard error in this estimate of the weight is:

$$\bar{\delta}_j = \sqrt{\frac{W_j (1-W_j)}{N_t}} \quad . \quad . \quad . \quad . \quad 7.2$$

This basic technique can be modified to follow the

data more closely by simulation of the following processes.

(a) Multiple Scattering

The incident and scattered particles suffer many small angle deflections which are principally due to Coulomb interactions with the nuclei of the materials they traverse. Since these deflections are independent the phenomenon is one of multiple scattering for which accurate theories exist. The distribution of the nett deflection in each material is approximately gaussian but with 'broad tails'.

In order to incorporate the correction into the Monte Carlo an estimate of the distribution in terms of the radiation length is normally used. In the absence of large angle scatters the distribution is assumed to be gaussian with a standard deviation given by:[31]

$$\sigma = \frac{21.2}{P\beta}\sqrt{\frac{L}{Lr}}\left[1+\frac{1}{9}\log_{10}\left(\frac{L}{Lr}\right)\right]\left[1+\frac{M^2}{Em_s}\right]$$

where the incident particle has mass M, velocity β, energy E and momentum P, and where the scatterer has atomic mass m_s, radiation length L_r and is of thickness L.

Multiple scattering is simulated by deflecting the particle in each material traversed before the counter

hodoscopes. In each case the path length in the material is determined and σ computed from the above expression. The scattering angle is then chosen randomly from a gaussian distribution of width σ and applied to the trajectory midway between the entry and exit points of the material. The azimuthal direction of the deflection is chosen randomly from between 0 and 2π .

(b) Energy Loss

Energy is dissipated by the particles principally via interactions with atomic electrons. The mean rate of energy loss per unit path length for collisions with electrons is given by the Bethe Bloch formula:[32]

$$\frac{dE}{dx} = \rho D \frac{Z}{A} \frac{1}{\beta^2} \left[\ln \left(\frac{2mc^2\beta^2}{(1-\beta^2)I^2} \left[\frac{2m_e P^2}{M^2 + m_e^2 + 2\varepsilon m_e} \right] \right) - \beta^2 - K \right]$$

where $D = 0.1535$ MeV $cm^2 g^{-1}$

Z and A are the charge and mass number of the material

I is the mean ionization potential of the material

β, P, ε and M are the velocity, momentum, energy and mass respectively of the incident particle.

K includes shell and density correction terms.

A modified version of the formula can be used for computing energy losses by neglecting the shell and density correction terms. The error introduced by such an approximation is less than 1% over the entire

momentum range of interest. The energy lost in each material is calculated from the product of dE/dx and the pathlength, and the energy of the particle corrected by the corresponding amount.

This simple procedure cannot be used for slow particles since the value of dE/dx changes appreciably within the slowing medium. Hence for slow recoil protons a range parameterisation is used to identify those not having sufficient energy to reach the T4 hodoscope. Those protons having sufficient energy can be tracked through the detectors and subjected to the normal energy loss and multiple scattering corrections.

(c)Absorption

An exact simulation of strong scattering between the kaon or proton and nuclei of the absorbing materials would require the use of differential cross sections for each process over a wide range of energies. This is clearly unfeasable in a computer calculation. Instead a random number is called to reject a track segment according to the probability that its associated particle is absorbed. This probability is given by:

$$1 - \exp[-\sum_i n_i \sigma_i t_i]$$

where t_i and n_i are the pathlength and density of nuclei per unit volume in each material.

σ_i are the total cross sections for nuclear scattering in each material, which can be estimated from the nuclear cross sections using a simple superposition model.

The validity of this approach relies on the fact that strong scatters generally produce substantial changes in both energy and direction of the particle and therefore spoil the elastic geometry of the events.

(d)Kaon Decay

The probability of a particle moving a distance l before undergoing decay is given by:

$$\exp[-l/l_D(\beta)]$$

l_D is the decay length of the particle and is a function of the velocity β .

At 1 GeV/c the decay length of the kaon is 7.4m, which implies that a large fraction decay before they leave the experimental region. However since the decays are isotropic in the kaon rest frame they can be easily generated by calls to the random number generator. Thus a rigorous treatment of the decay process is possible in the Monte Carlo calculation.

For each trial the total pathlength covered by the kaon before the decay point is reached must be randomly

chosen from the distribution defined above. One of the partial decay modes is then selected, being chosen on the basis of the branching ratios. However the two body decays represent 85% of the total decays and generation of the decays is greatly simplified if only these are considered:

$$K^- \rightarrow \mu\bar{\nu} \quad (75\%)$$

$$K^- \rightarrow \pi\pi^0 \quad (25\%)$$

If the decay is transformed to the laboratory frame the event simulation can proceed with the charged decay product.

The resolution with which the chambers record the particle trajectories can also be included by generation of 'pseudo sparks' at the chamber positions. The direction of the particle is then approximated by the straight line fitted to these points. Since the trajectories have been subjected to distortion the fitted tracks no longer automatically pass the selection criteria. Thus in addition to the trigger requirement the events must obey the constraints applied to the real data if they are to be counted; therefore the probability function is defined to be 1 only if all constraints are satisfied.

7.3 Evaluation Of The Weights

The approach adopted in the event simulation has therefore been to subject the particles to those processes affecting the real data and to record trajectories, as seen by the spark chambers, in D.S.T. format. The selection procedure described in section 6.3 was then applied to this data thus ensuring that simulated and real events satisfied the same constraints. The probability function was defined to be 1 only if all the constraints were satisfied and the weights and their errors were calculated according to equations 7.1 and 7.2 .

The event simulation proceeded as follows. Firstly, importance was attached to the generation of events from beam tracks that had the same position and momentum distributions as candidates in the real data. An unbiased sample of beam tracks was obtained from the CANDIDATE triggers recorded in the experiment. This sampling had to be done randomly over all data taken, since the beam profile was subject to changes. For this reason the Monte Carlo was run using CANDIDATE beam tracks from each run of real data..

A trial scatter was then generated from a random position along the beam track but within the physical region of the liquid hydrogen vessel. The scattering

angle was chosen from within the required $\cos\theta^*$ bin and the azimuth from between 0 and 2π .

At this point trials were rejected according to the probability that the beam kaon decayed or was absorbed between the final beam counter and the trial vertex. The true distribution of candidates was assumed to be:

$$N_C = N(l) = N_{D2} \exp[-\sum_i n_i \sigma_i t_i + l/l_D(\beta)]$$

where N_{D2} is the flux of kaons measured at D2 and the materials included in the summation are D2, the target window, and the thickness of liquid hydrogen penetrated up to the trial vertex.

In addition, the energy and direction of the kaon at the vertex were modified for energy loss and multiple scattering in these materials and the scattered particle directions were determined relative to the adjusted beam trajectory.

Both particles were then tracked separately through the materials of the detectors and changes in the trajectories due to multiple scattering and energy loss were determined. The materials considered were:

(a) the liquid hydrogen, which was enclosed in a cylindrical tube of mylar.

(b) the aluminium vacuum vessel.

(c) planes of chamber wires, which for simplicity were approximated by a thin sheet of metal of equivalent volume.

(d) sheets of mylar defining the chamber windows

(e) scintillator forming the T1 hodoscope.

(f) the air separating the detectors.

If the kaon reached its allocated decay point then the decay was generated and tracking proceeded with the charged decay product. The position of the particles at each chamber were recorded and randomly adjusted to reflect the chamber resolution. The absorption correction was applied separately at T1, T2 and T4 so that absorption in one tracking segment did not automatically result in rejection of the event. Providing the event satisfied the trigger selection criteria its associated track co-ordinates were written to the D.S.T.

The above procedure was repeated for many trials in each $\cos\theta^*$ bin. It can be seen from equation 7.2 that the error in the weight for a particular bin can be reduced by increasing the number of trials in that bin. The number of trials was chosen such that this error was small when compared with the error contribution from the data. The number of trials therefore varied from bin to bin according to the number of elastics in the real

data. This information was available on the D.C.S. dataset which was therefore read at the beginning of each Monte Carlo run to define the number of events to be generated in each bin.

Once all trials had been completed the simulated events were processed by the event selection routines. The weights and associated errors were then calculated and were written to the D.C.S. dataset.

Distributions of some of the kinematic and geometric variables are presented in Figures 7.1→7.3 for comparison with those of the real data. The compatability of the elastic peaks suggests that the widths in the data can largely be accounted for by multiple scattering and decay which confirms the high resolution of the chambers.

7.4 Beam Contamination Calculation

Kaons decaying between the DISC and D2 produced a CANDIDATE trigger when a charged decay product intercepted the D2 counter. This contamination of the of the CANDIDATE signal was estimated by a Monte Carlo program using a sample of the measured beam tracks. The correction was found to be approximately 0.7% which was assumed to be negligible.

a) C-MODE

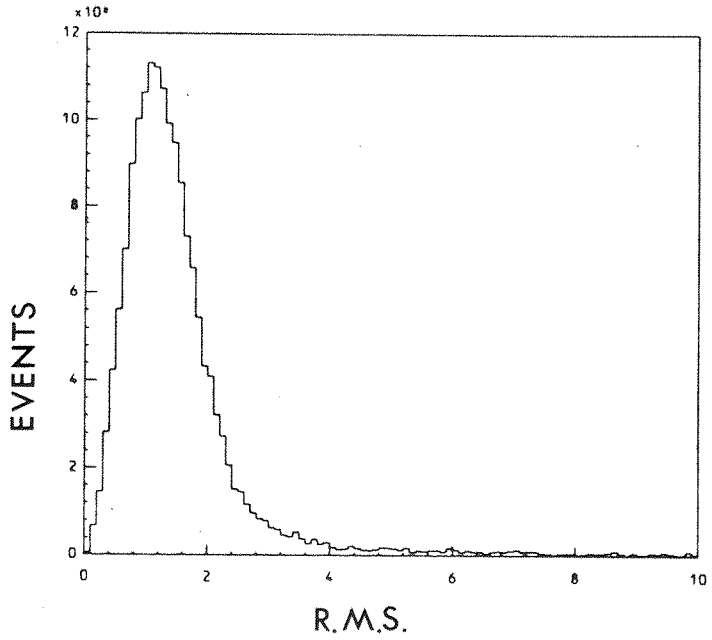

b) S-MODE

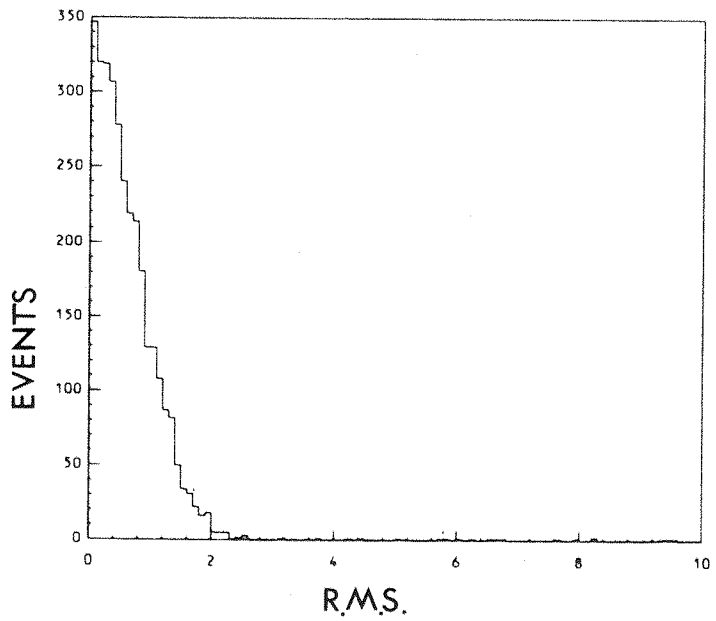

FIG. 7.1 R.M.S. DISTRIBUTIONS FOR MONTE CARLO EVENTS

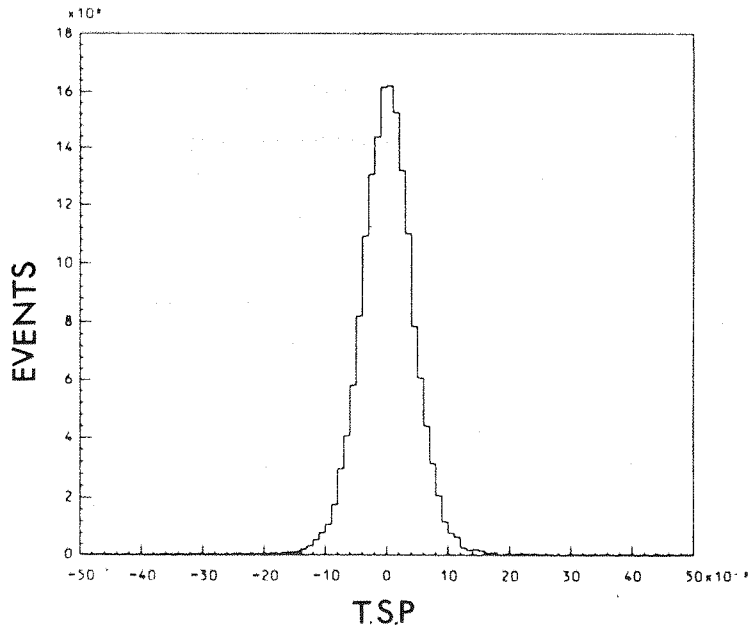

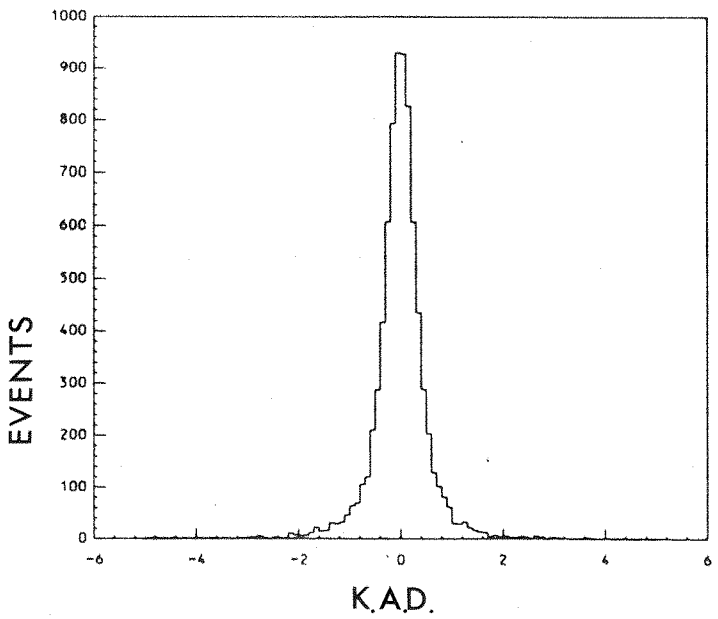

FIG. 7.2 T.S.P. & K.A.D. DISTRIBUTIONS FOR MONTE CARLO EVENTS

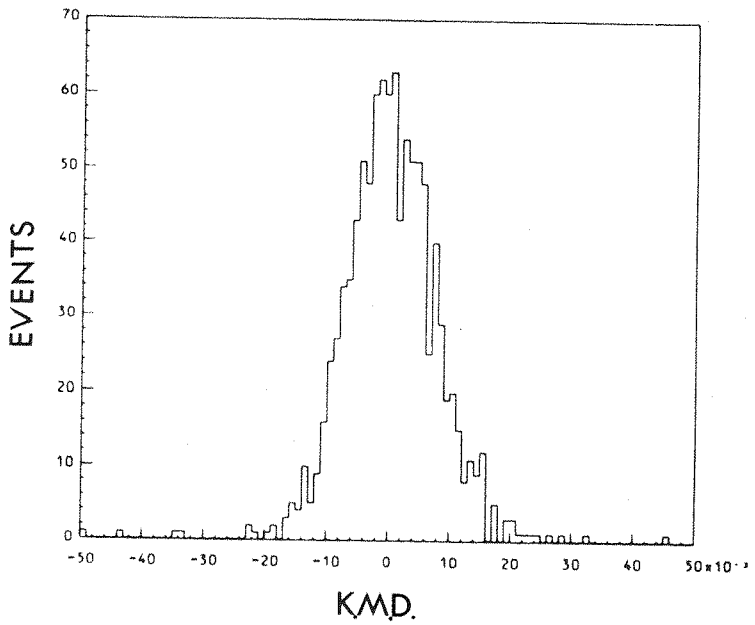

FIG. 7.3 K.M.D. FOR MONTE CARLO EVENTS

CHAPTER 8

RESULTS

Analysis of the data has not been completed and so the results presented here are preliminary. Extensive alignment checks have been performed only for data taken during the first two cycles (July to September 1976); the analysis has therefore been confined to data recorded during this period.

8.1 Differential Cross Sections

The differential cross section was computed from the angular distribution of events selected by the analysis routines and from weighting factors determined by the Monte Carlo program. Equation A1.1 was used assuming a target of liquid hydrogen boiling at one atmosphere.

Results have been obtained for five of the twentythree momenta and these are presented in graphical form in Appendix 4. The sample of data analysed represents approximately 60% of the total number of triggers recorded at each momentum. The data points do not cover the complete angular range being limited by

the kinematic ambiguity in the forward region and by the 3° cut, based on the vertex resolution, in the backward direction. The errors on each data point are purely statistical; normalisation errors are not included.

The solid curves represent a fit to the data by a Legendre Polynomial series:

$$\frac{d\sigma}{d\Omega}(\theta^{*}) = \sum_{n=0}^{N} C_n P_n(\cos\theta^{*})$$

The coefficients, C_n, were determined by minimising the function F:

$$F = \sum_{i=1}^{M} \left[\frac{d\sigma(\theta_i^{*})/d\Omega - \sum C_n P_n(\cos\theta_i^{*})}{\Delta_i} \right]^2$$

where M represents the number of data points (θ_i^{*}), with Δ_i the experimental errors.

The number of terms required to produce an accurate fit was determined by observing the χ^2 per degree of freedom of the data points. The present points have been fitted with polynomials of degree ten, producing a χ^2 approaching one. Increasing the order of the fit failed to produce a significant improvement in the fit.

The graphs also indicate the forward differential cross section and the elastic cross section. The forward differential cross section was determined by

extrapolating the fit to the forward point and the elastic cross section from the zero order coefficient:

$$\sigma_{el} = \int_0^{2\pi}\int_{-1}^{1} \frac{d\sigma}{d\Omega}\, d\phi\, d\cos\theta = 4\pi C_o$$

8.2 Comparison With Other Experiments

The results from this experiment have been compared with previous measurements selected according to their statistical precision.

At the low end of the momentum region the present experiment overlaps the experiment of Conforto et. al.[14]. This was a high statistics bubble chamber study containing approximately 15,000 events at each momentum. Comparison is made at 1212 MeV/c and 1283 MeV/c (Figs.8.1&8.2). There is good agreement in the shape of the differential cross section at both these momenta. The main discrepancy lies in the relative normalisation of the two experiments.

At higher momenta the results have been compared with the bubble chamber study of Litchfield et. al.[6] (Figs.8.3 to 8.5). This experiment recorded approximately 2000 elastics events.per momentum setting; thus the results from the present experiment represent a significant improvement in statistics. At 1433 MeV/c and 1683 MeV/c the data have also been compared with the

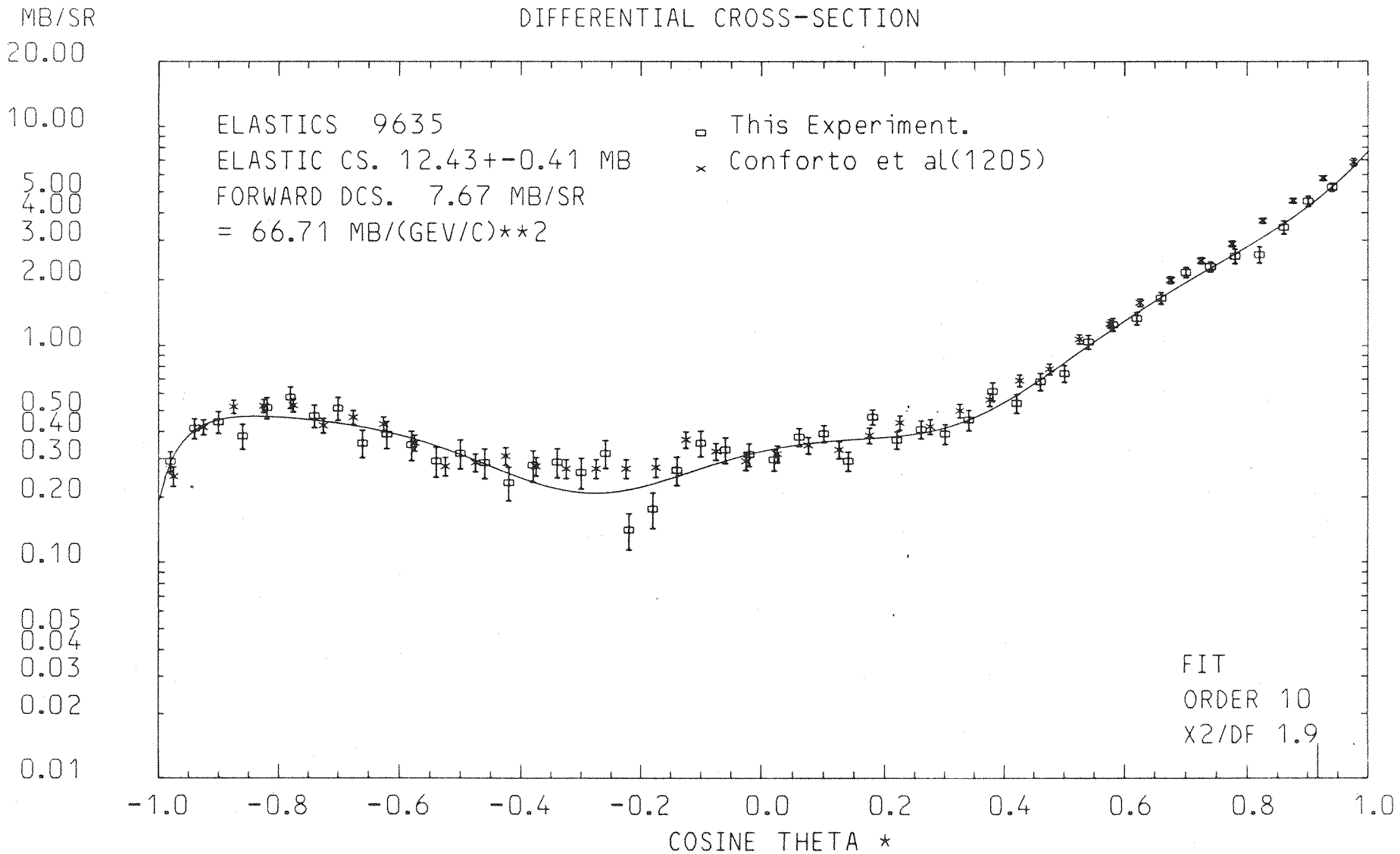

FIG 8.1 1.212 GEV/C. K- P ELASTIC K15A.

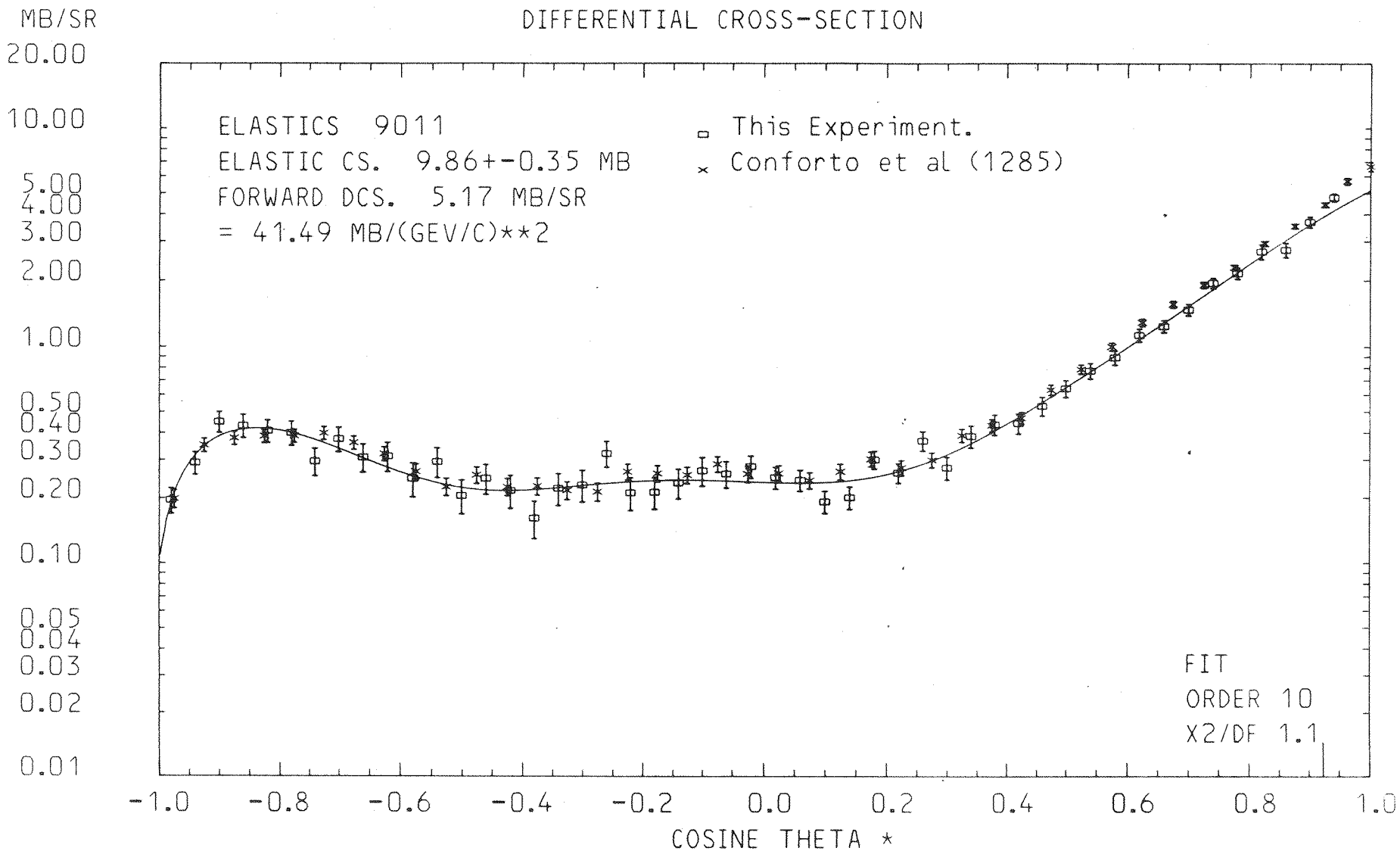

FIG. 8.2 1.283 GEV/C. K- P ELASTIC K15A.

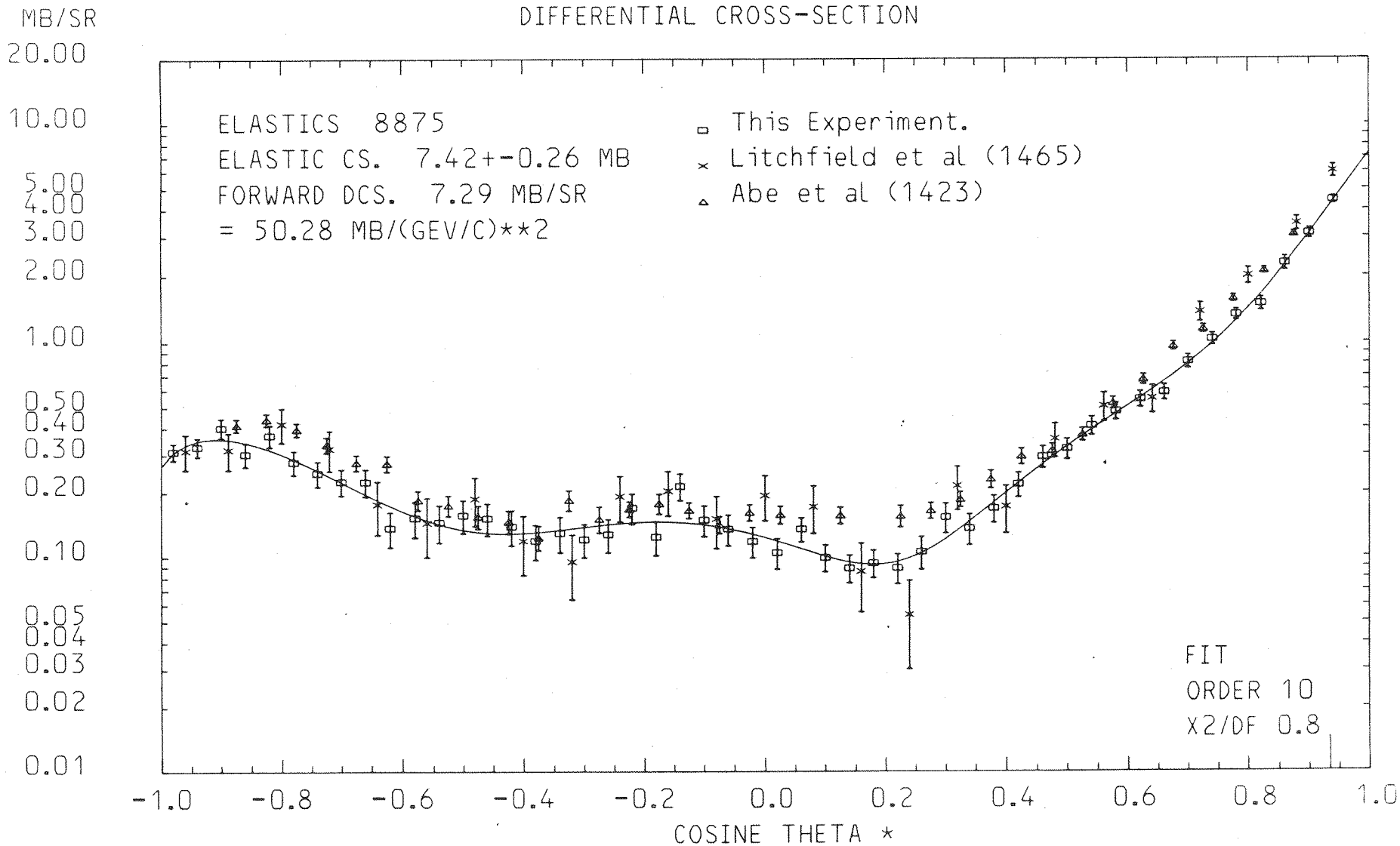

FIG 8.3 1.433 GEV/C. K- P ELASTIC K15A.

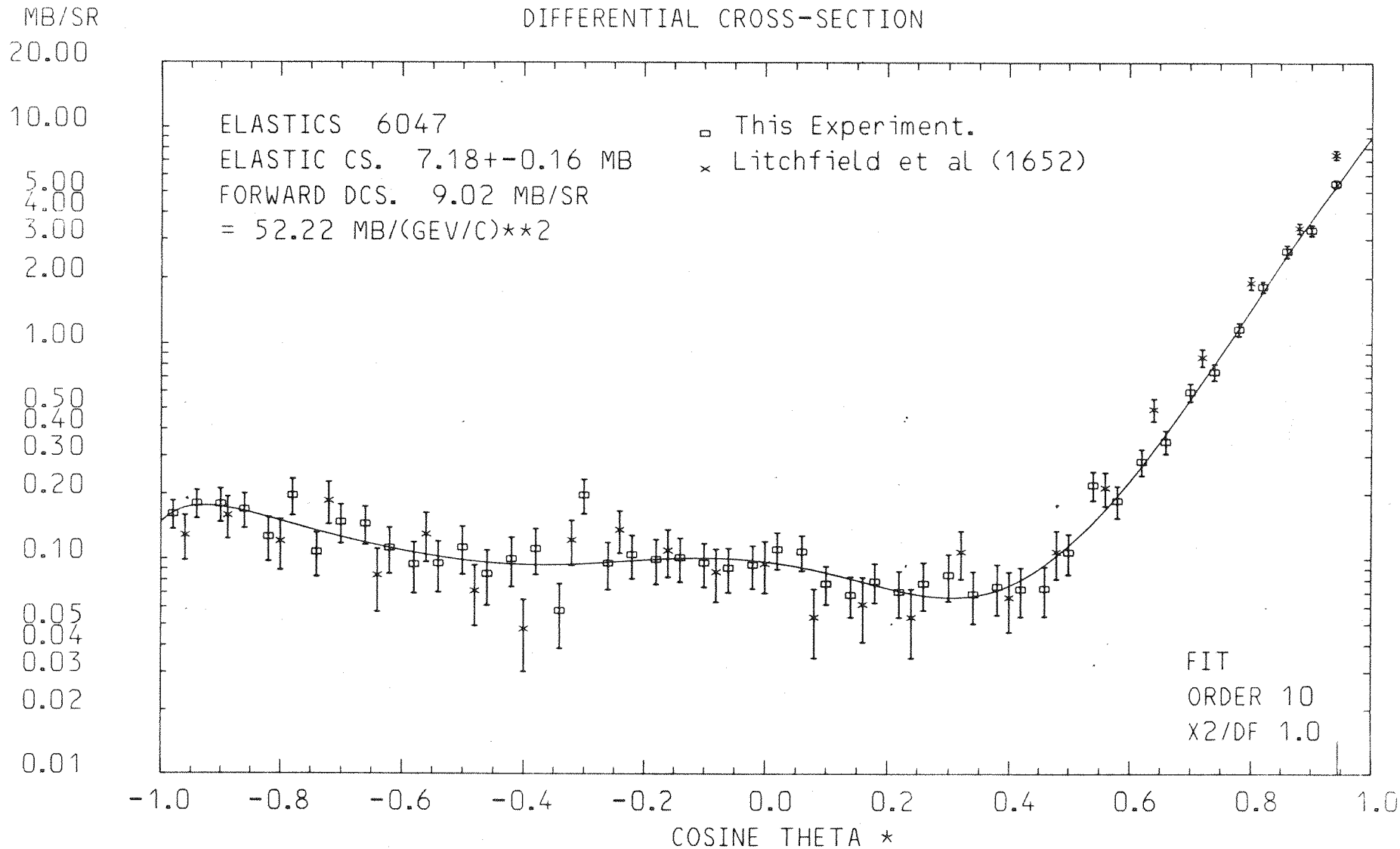

FIG 8.4 1.633 GEV/C. K- P ELASTIC K15A.

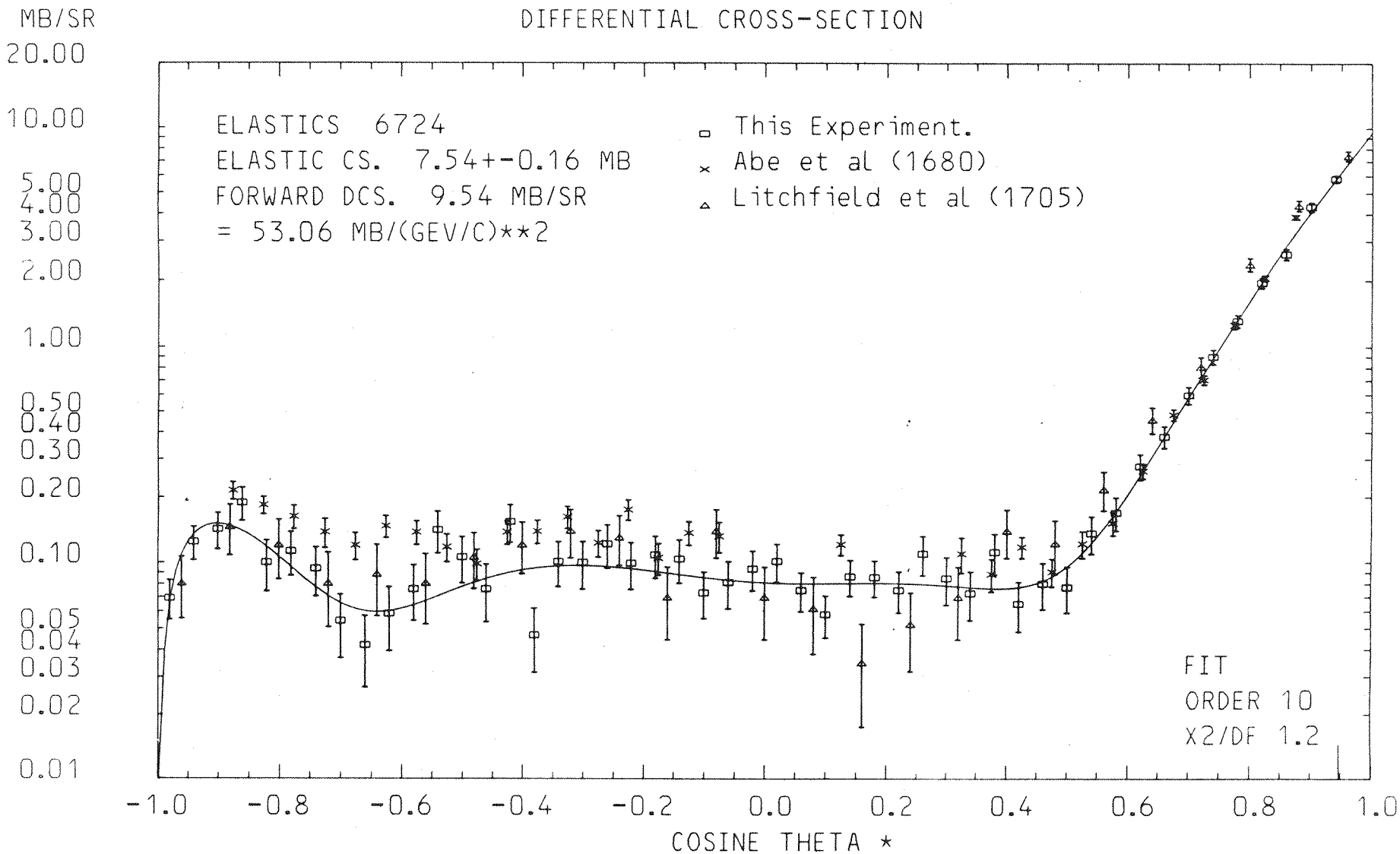

FIG 8.5 1.683 GEV/C. K- P ELASTIC K15A.

spark chamber experiment of Abe et. al.[13] This experiment has relatively high statistics but covers only the C-mode part of the angular range. Again, although there is good agreement between the shape of the distributions the normalisation of the present experiment is low by comparison.

8.3 Normalisation Check

An absolute check on the normalisation was provided by the sample of $K \rightarrow \mu\bar{\nu}$ events detected in the S-mode region. By changing kinematic routines to select muon decays an angular distribution of acceptable events was obtained. In addition, a modified version of the Monte Carlo program was used to obtain the acceptance of the detectors for the decay process.

It is convenient to compare the experimental results with theoretical predictions in terms of a 'pseudo-differential cross section', where the kaon decay length (l_D) is interpreted as the scattering length (l_s) of the reaction.

For a random process the fraction of particles moving a distance l without 'interaction' is given by:

$$\exp(-l/l_s)$$

The scattering length is related to the 'cross section',

σ , by:

$$l_S = 1/n\sigma$$

where n is the number of scattering centres.

Hence for the $K->\mu\bar{\nu}$ process:

$$\sigma_{\mu\bar{\nu}} = 1/(n\ l_D(\beta)B_{\mu\bar{\nu}})$$

where $B_{\mu\bar{\nu}}$ is the branching ratio for the $\mu\bar{\nu}$ decay mode.

Since the kaon is spinless the decay is isotropic in the centre of mass. Thus the 'differential cross section' is given by:

$$\frac{d\sigma}{d\Omega}_{\mu\bar{\nu}} = \frac{\sigma_{\mu\bar{\nu}}}{4\pi}$$

The decay length is related to the kaon lifetime τ by:

$$l_D = Pc\tau/M$$

where P is the kaon momentum and M its mass.

Thus with the assumption of a liquid hydrogen target, the theoretical prediction for the $K->\mu\bar{\nu}$. differential cross section becomes:

$$\frac{d\sigma}{d\Omega}_{\mu\bar{\nu}} = \frac{1.59007}{P} \quad \text{mb/sterad/(GeV/c)}$$

The decay distributions are presented in Figures 8.6 to 8.10. The angular region covered by the

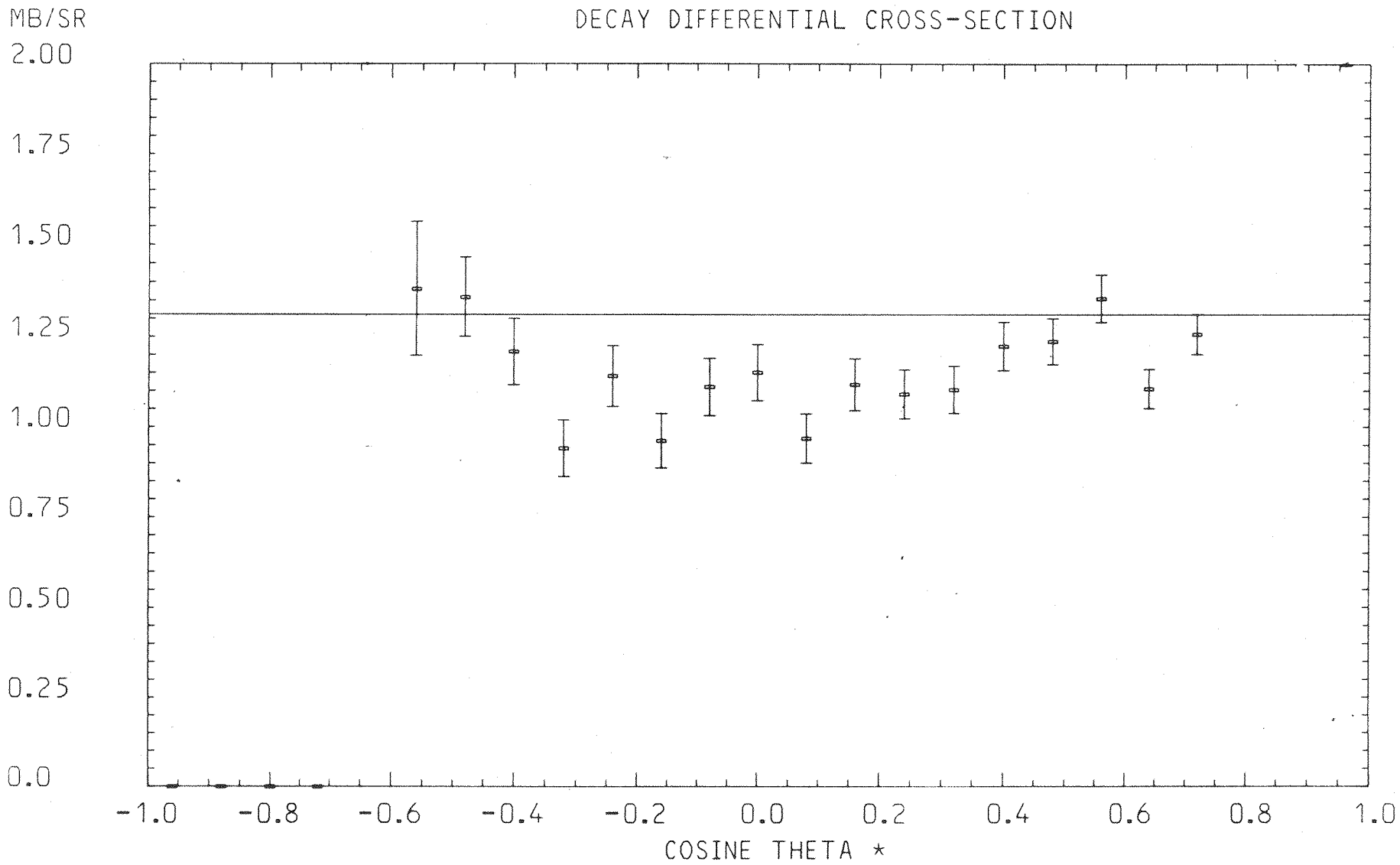

FIG 8.6 DECAY DCS AT 1.212 GEV/C

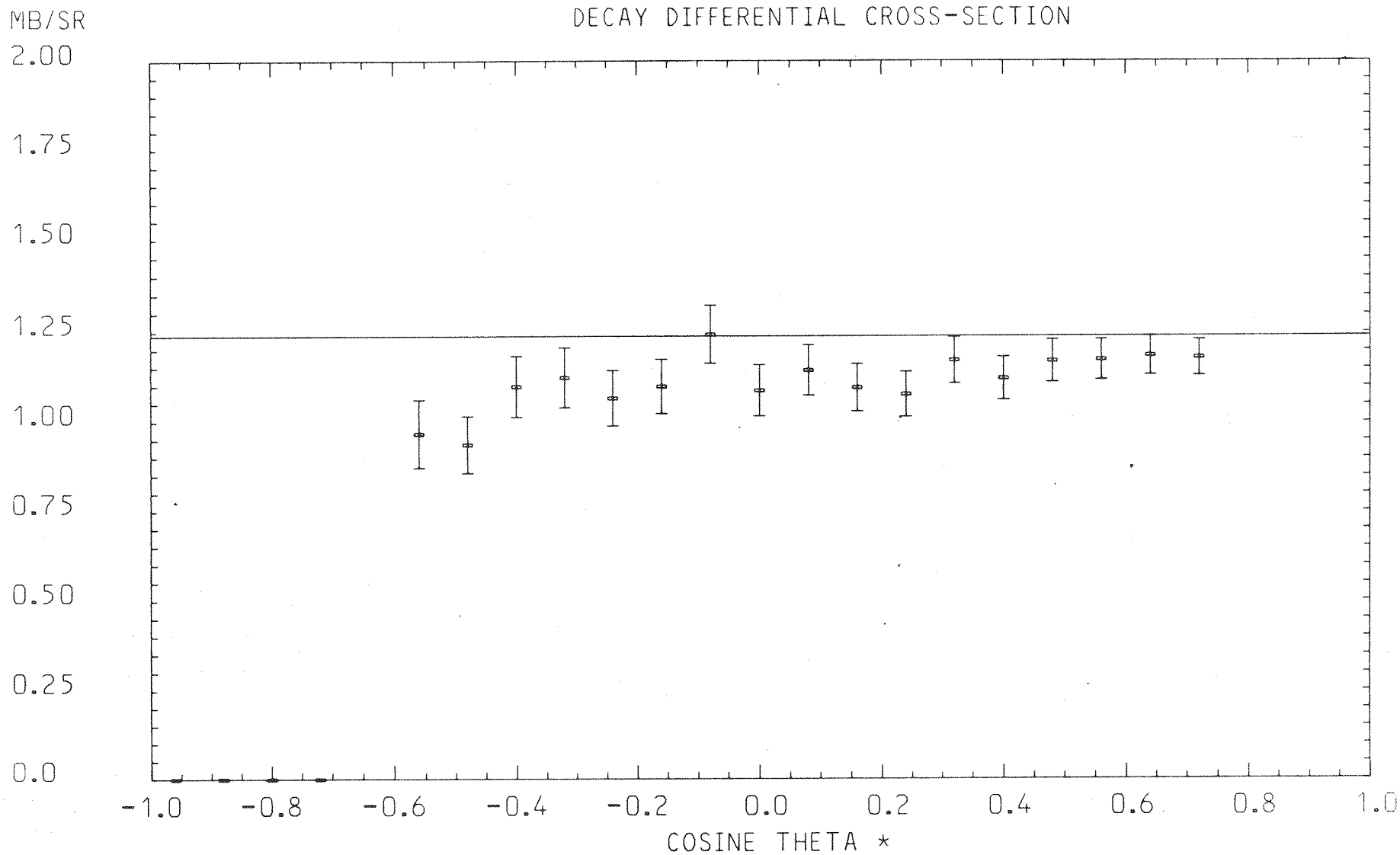

FIG 8.7 DECAY DCS AT 1.283 GEV/C

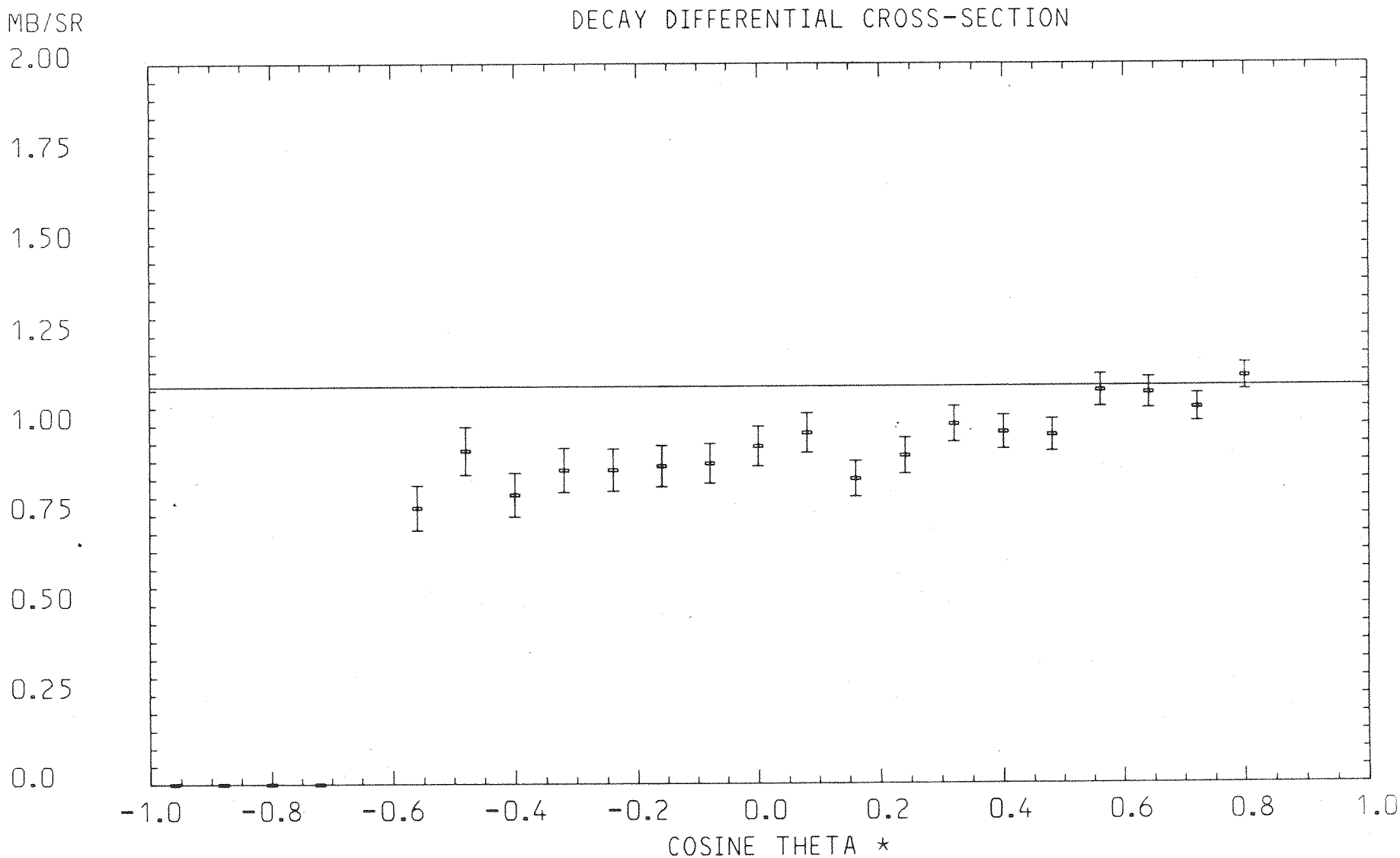

FIG 8.8 DECAY DCS AT 1.433 GEV/C

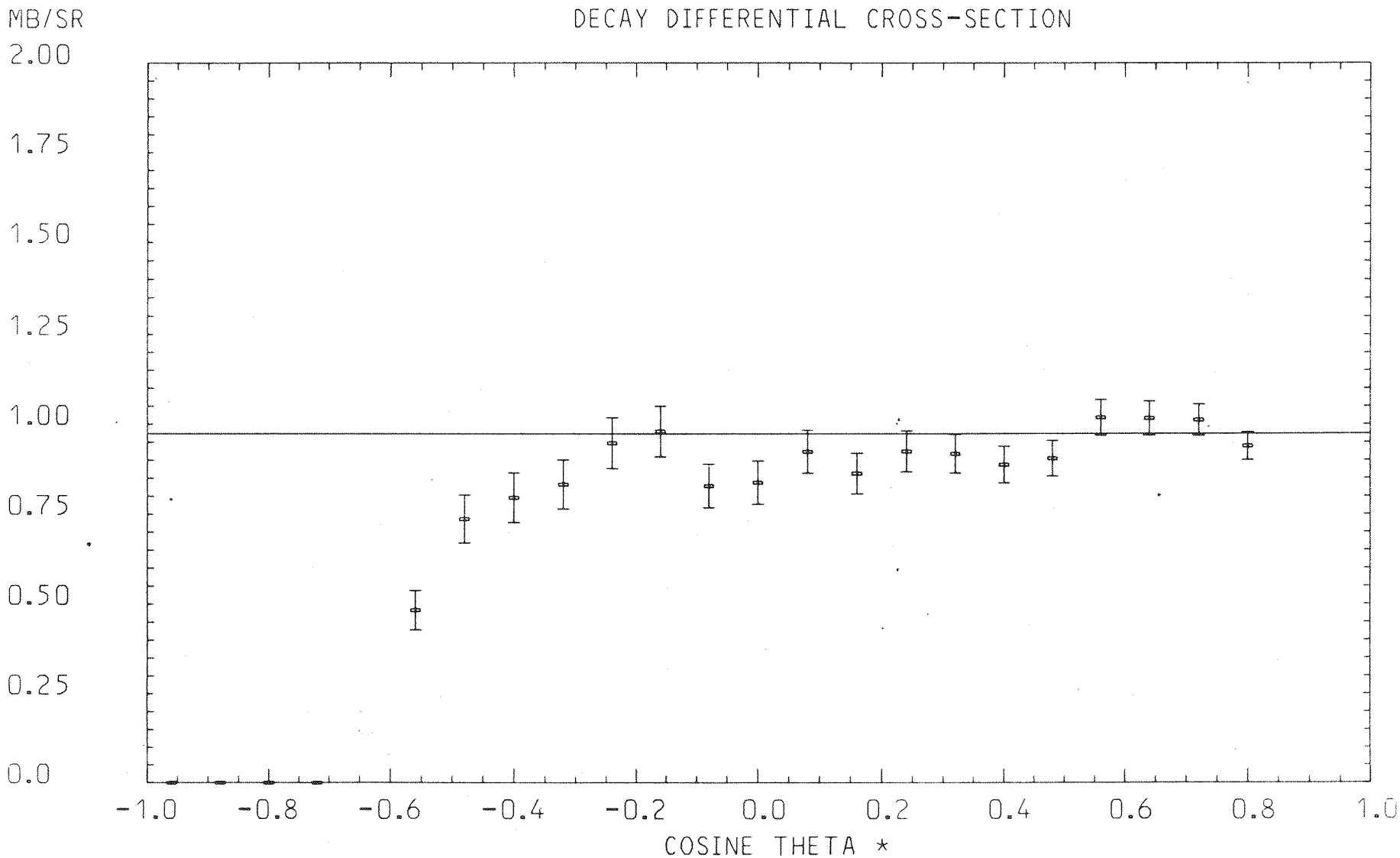

FIG 8.9 DECAY DCS AT 1.633 GEV/C

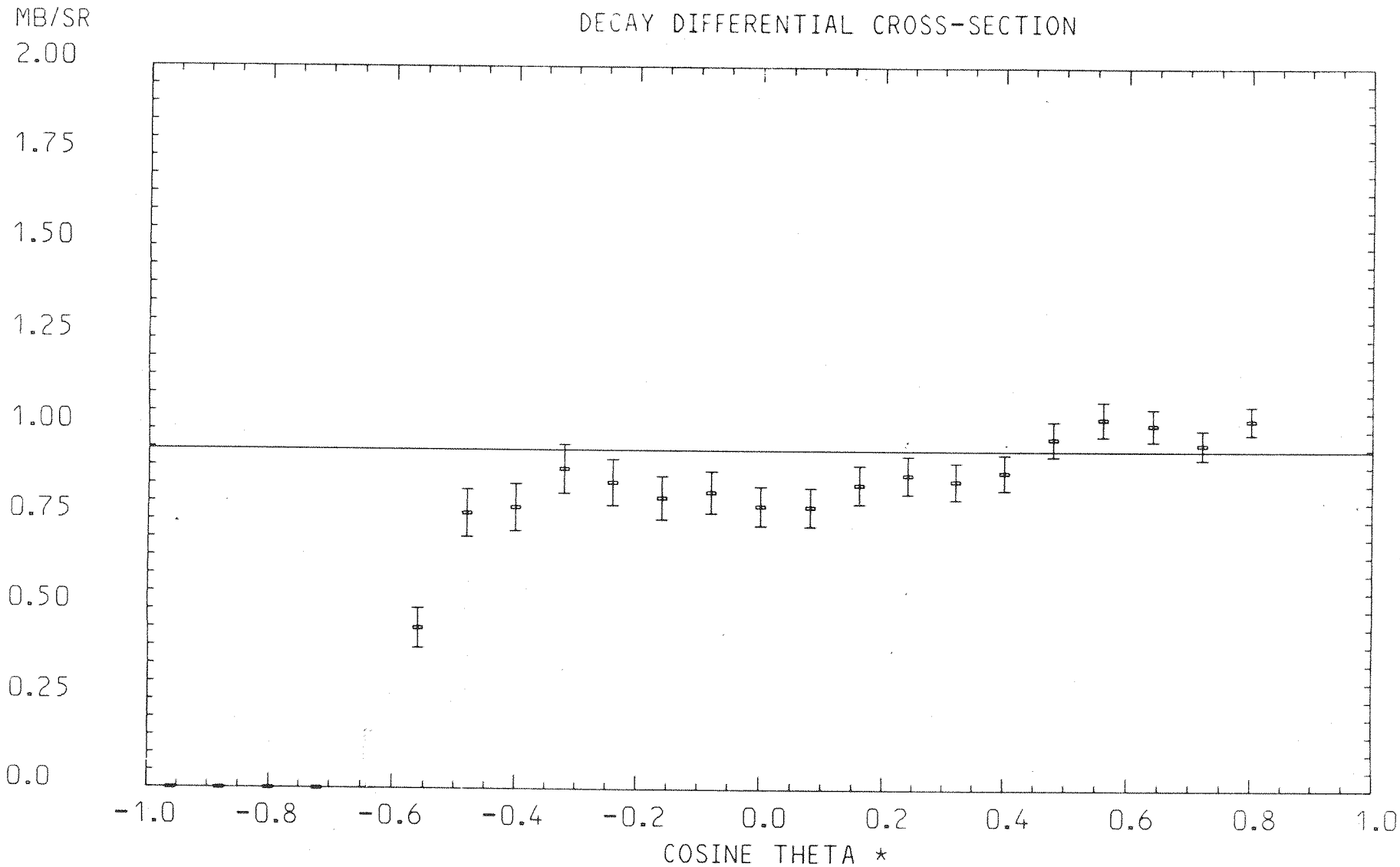

FIG 8.10 DECAY DCS AT 1.683 GEV/C

distributions is limited by the kinematic ambiguity in the forward direction and by the acceptance of the detectors in the backward direction. Again error bars on the data points are purely statistical.

Within statistical fluctuations the distributions are isotropic, apart from some evidence for a 'fall off' in the backward region. However the points lie consistently below the theoretical value which is indicated by the horizontal line. The discrepancy has been calculated at each momentum by fitting a straight line to the data points for values of $\cos\theta^*$ above -0.4. The factors required to bring the results into agreement with the theoretical values are given in Table8.1.

Table 8.1 Renormalisation factors, R, from a least squares fit to the decay distribution.

Momentum(MeV/c)	R
1212	1.16 ± 0.02
1283	1.09 ± 0.01
1433	1.17 ± 0.01
1633	1.07 ± 0.01
1683	1.07 ± 0.01

For the C-mode there was no absolute check on the normalisation. Therefore the two modes were analysed

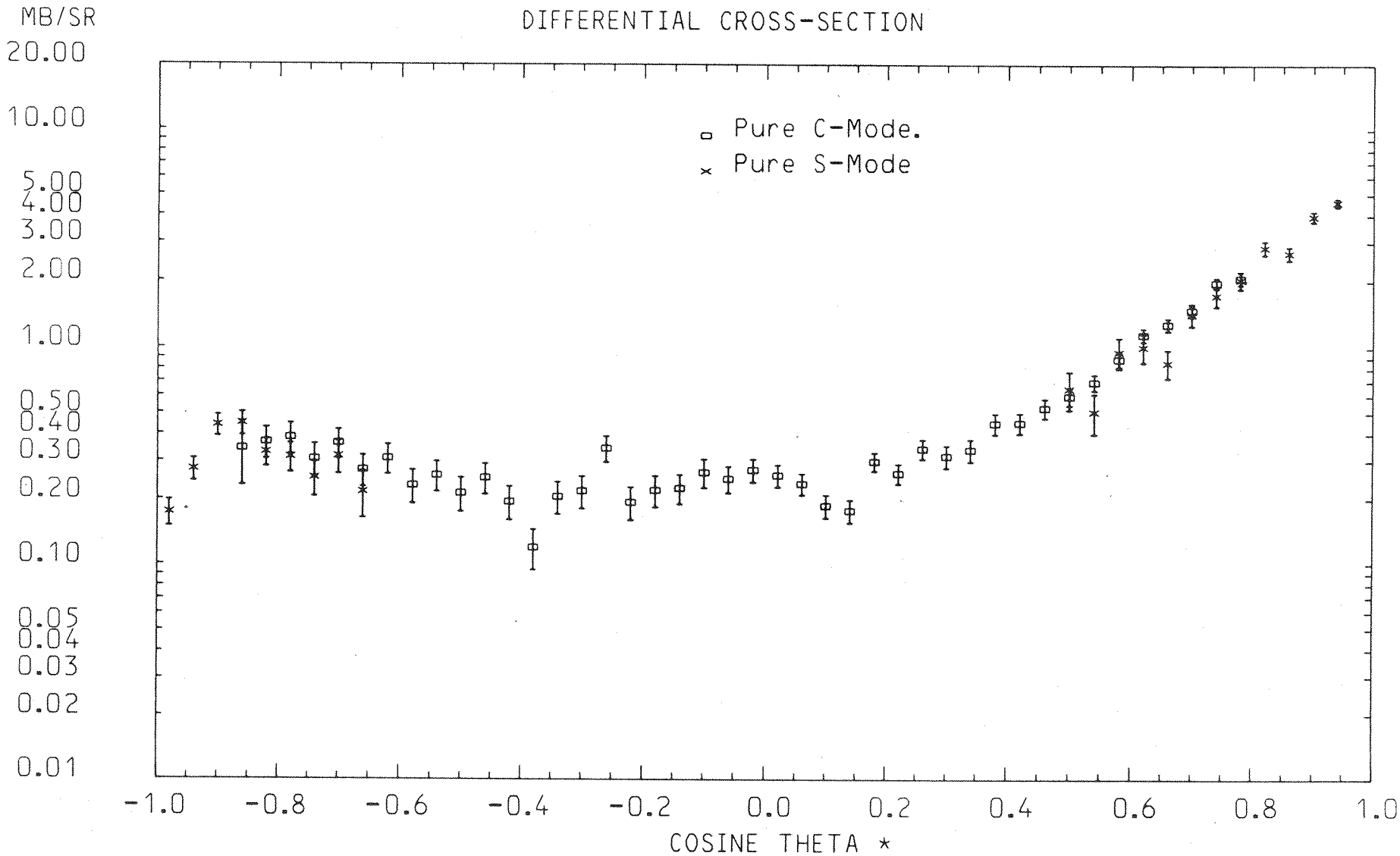

FIG 8.11 1.283 GEV/C. K- P ELASTIC K15A.

separately and an estimate of their relative normalisation was made by comparison of the resulting cross sections in the region of overlap. Figure 8.11 shows the result of such a test at 1283 MeV/c. The measurements appear to be consistent in the region from $0.5<\cos\theta^{*}<0.8$, but exhibit a small discrepancy between $-0.85<\cos\theta^{*}<-0.65$. It is worth noting that these results will be affected by asymmetry in the background.

8.4 Renormalisation

The decay distributions confirm the low normalisation of the present experiment for the S-mode, while the overlap check indicates that there is no serious discrepancy in the normalisation between the two modes.

At present the reason for this normalisation error is not known. However, since the discrepancy is common to both modes a fault in either the beam or S1S2 sections of the experiment is suspected. Inspection of a sample of events indicated that random particle tracks may be confusing track identification in the S1S2 'arm'. Thus a more general method of track finding is being developed which retains all reasonable tracks for selection by the kinematic routines.

The factors given in Table8.1 have been used to

renormalise the data and a new comparison with existing experiments made. At 1212 MeV/c (Fig.8.12) and 1283 MeV/c (Fig.8.13) there is now close agreement with the normalisation of Conforto et. al. over the complete angular range. This conclusion is substantiated by the elastic cross sections (Table8.2).

Table 8.2 Elastic cross sections in comparison with Conforto(CF),Abe(AB) and Litchfield(LF)

Momentum MeV/c	σ_{el}(mb)	σ_{el}(mb)xR	Comparisons(mb)	
1212	12.43±0.41	14.40±0.48	13.89±0.37(CF)	
1283	9.86±0.35	10.75±0.38	10.96±0.26(CF)	
1433	7.42±0.26	8.68±0.31	8.42±0.40(AB)	9.11±0.42(LF)
1633	7.18±0.16	7.65±0.18		8.40±0.29(LF)
1683	7.54±0.16	8.09±0.18	8.19±0.37(AB)	9.08±0.34(LF)

At the higher momenta the data points are consistently below those of Litchfield et. al. in the region of the forward diffraction peak (Fig.8.14 to 8.16). However this experiment did not have an absolute normalisation check. Instead the forward point, obtained from a Legendre Polynomial fit, was used to normalise via the optical theorem to the total cross section. The experiment of Conforto et. al. was normalised using Tau decays at all their momenta and by measuring the total

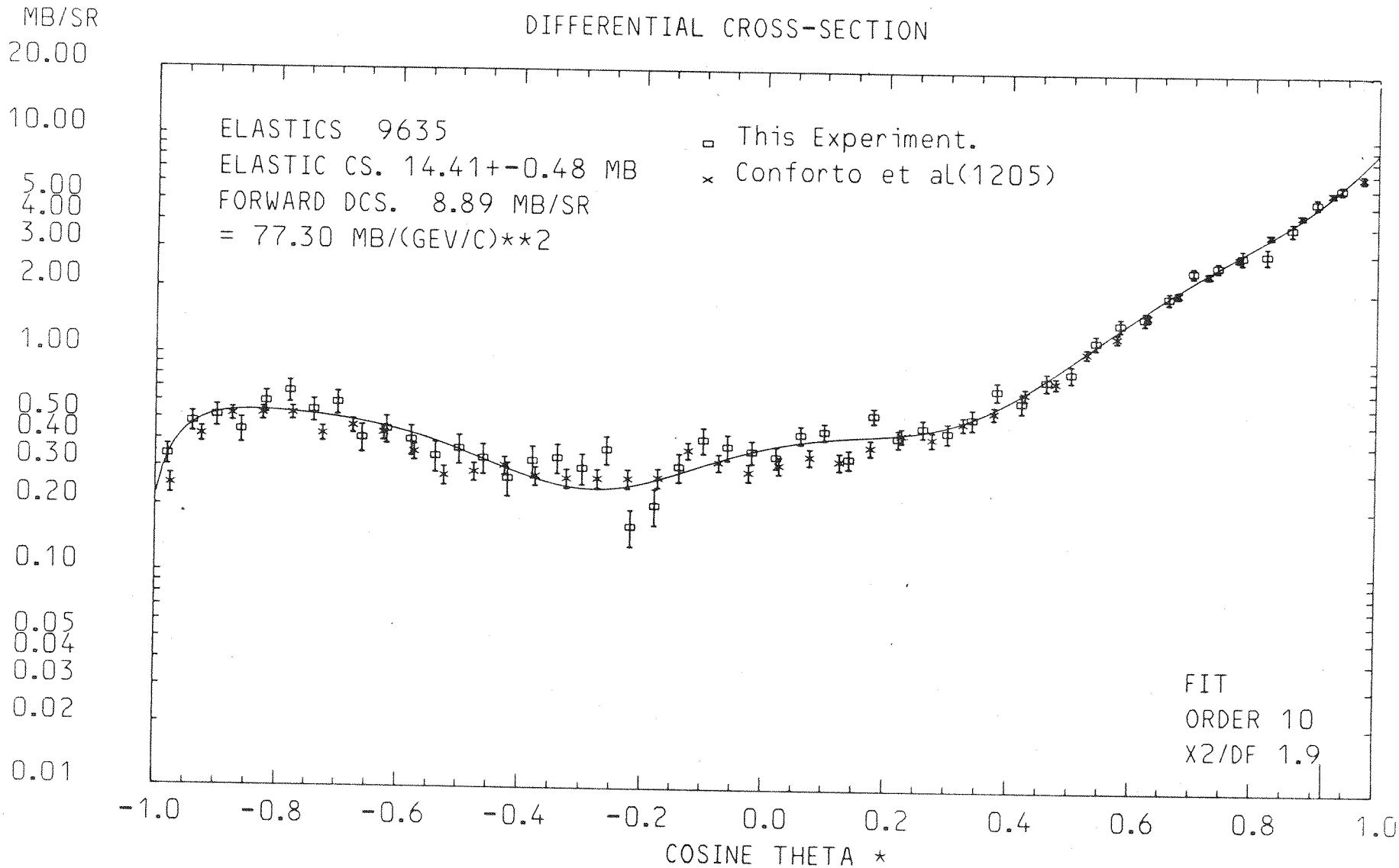

FIG 8.12 1.212 GEV/C. K- P ELASTIC K15A.

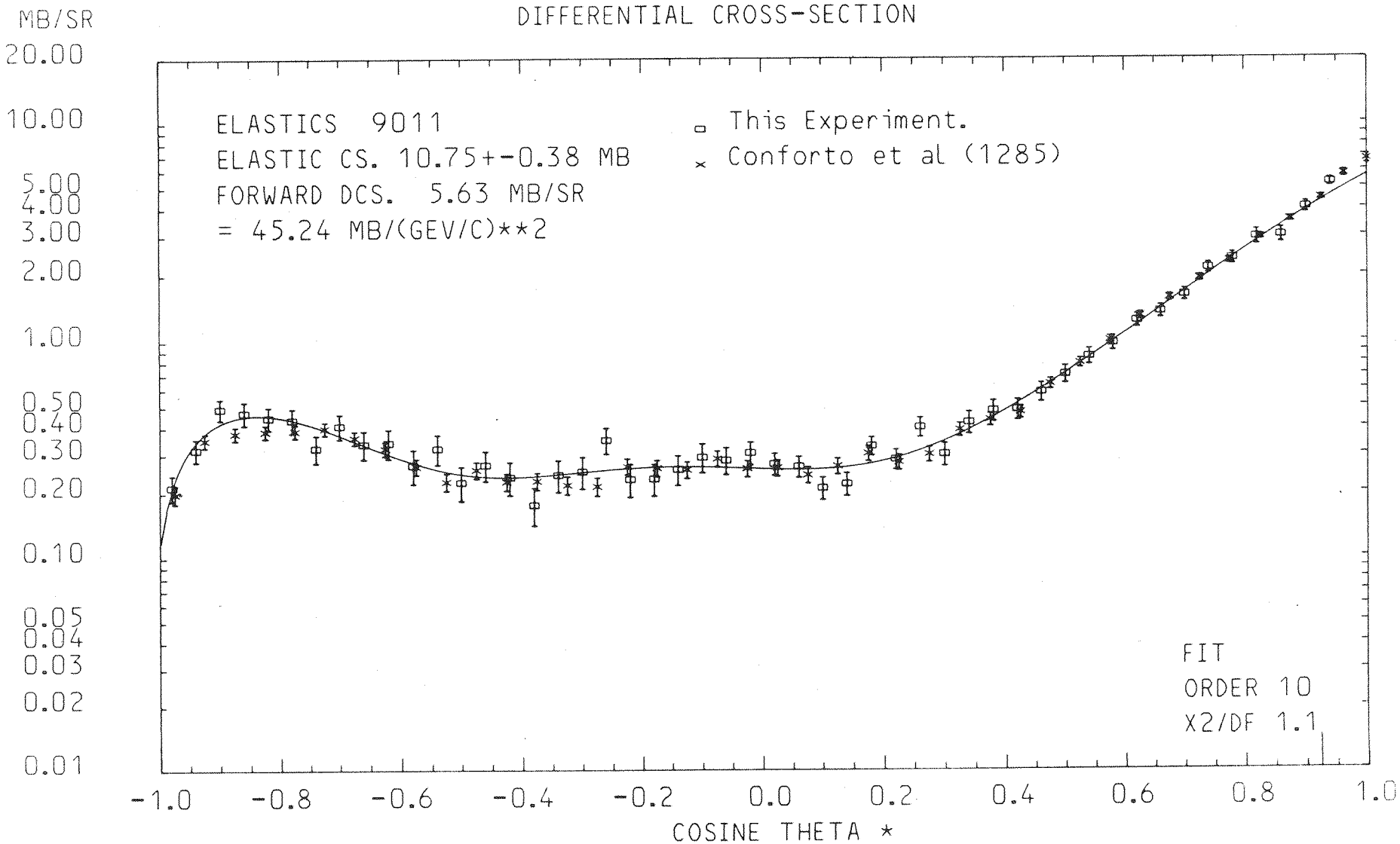

FIG 8.13 1.283 GEV/C. K- P ELASTIC K15A.

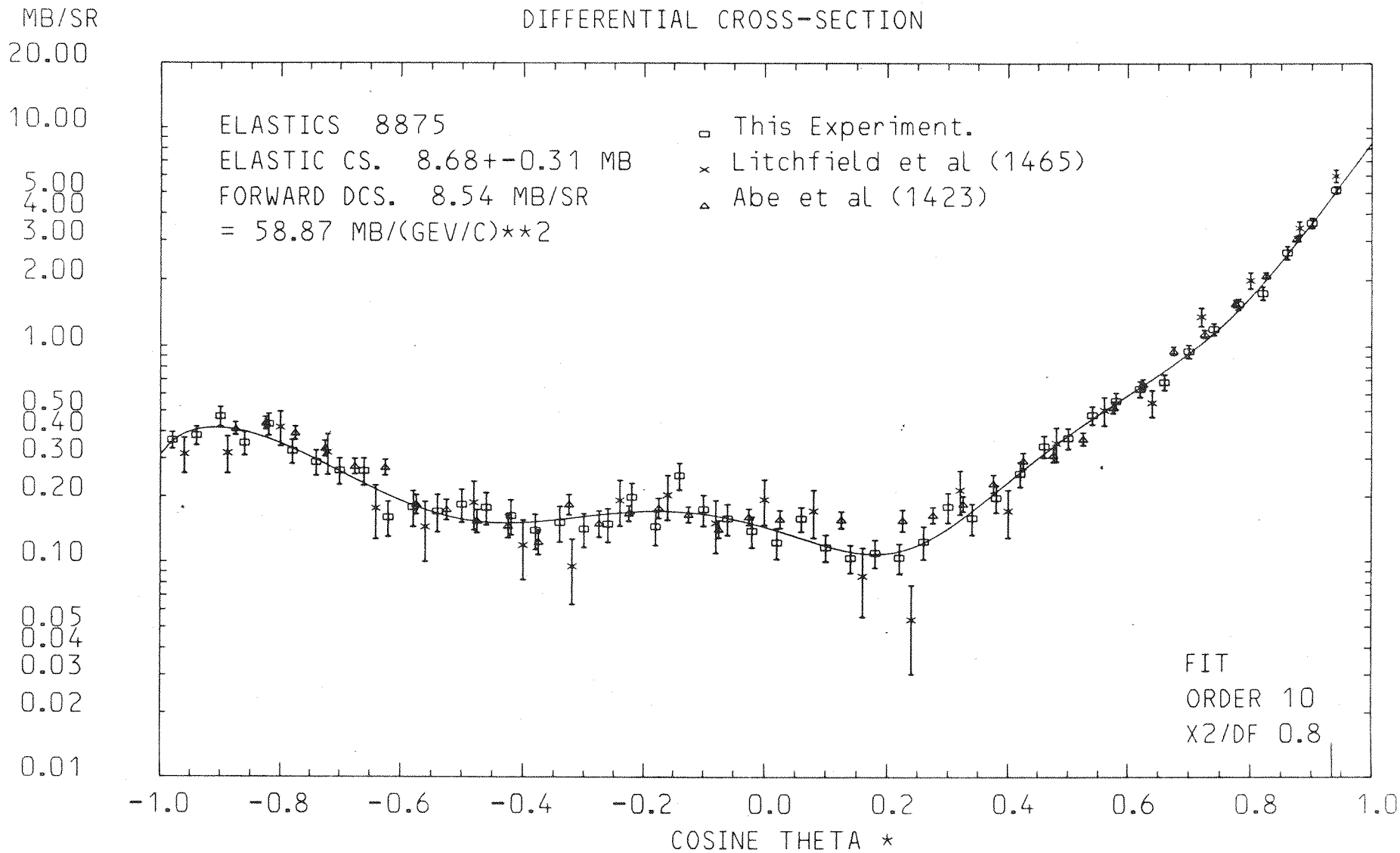

FIG 8.14 1.433 GEV/C. K- P ELASTIC K15A.

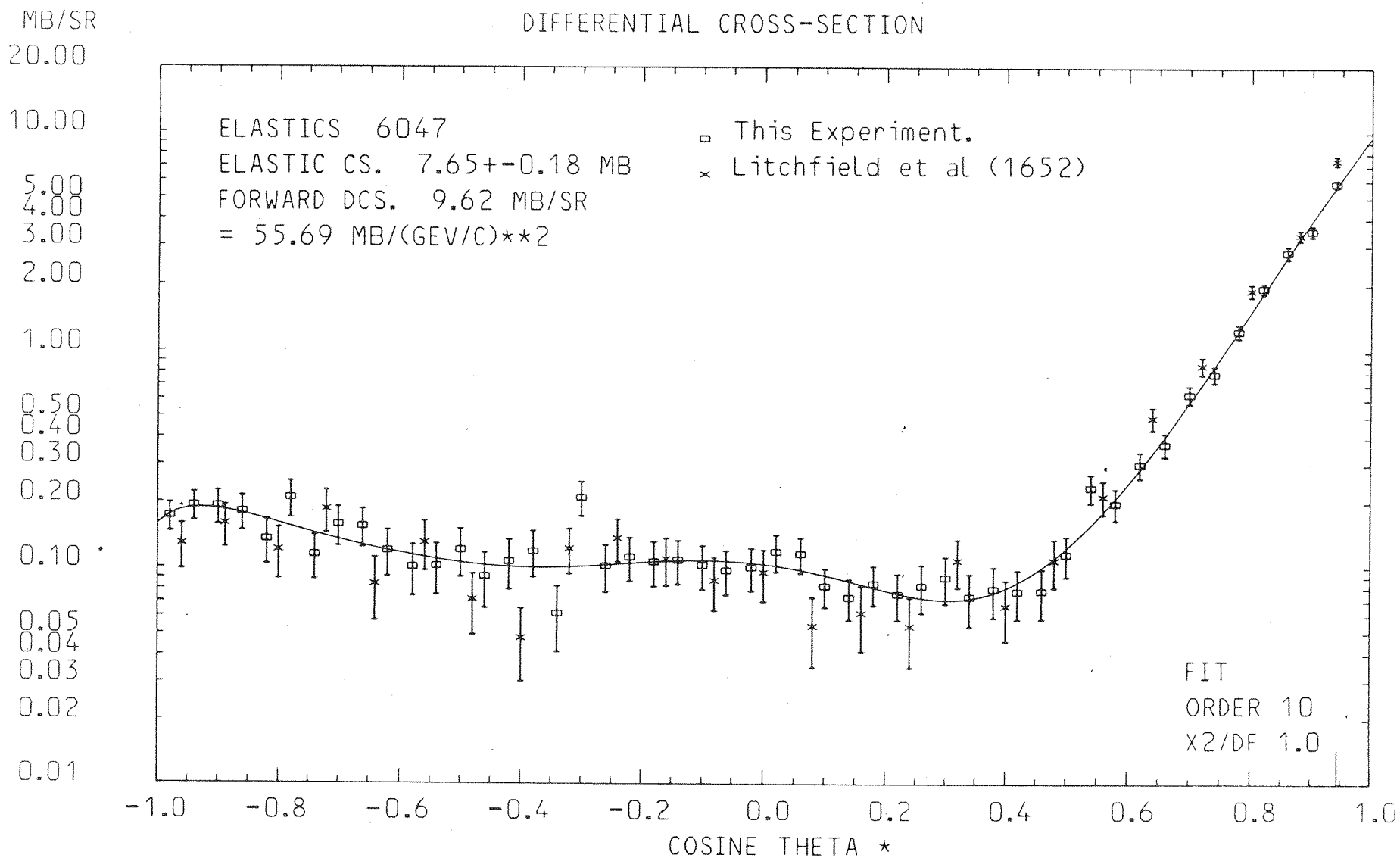

FIG 8.15 1.633 GEV/C. K- P ELASTIC K15A.

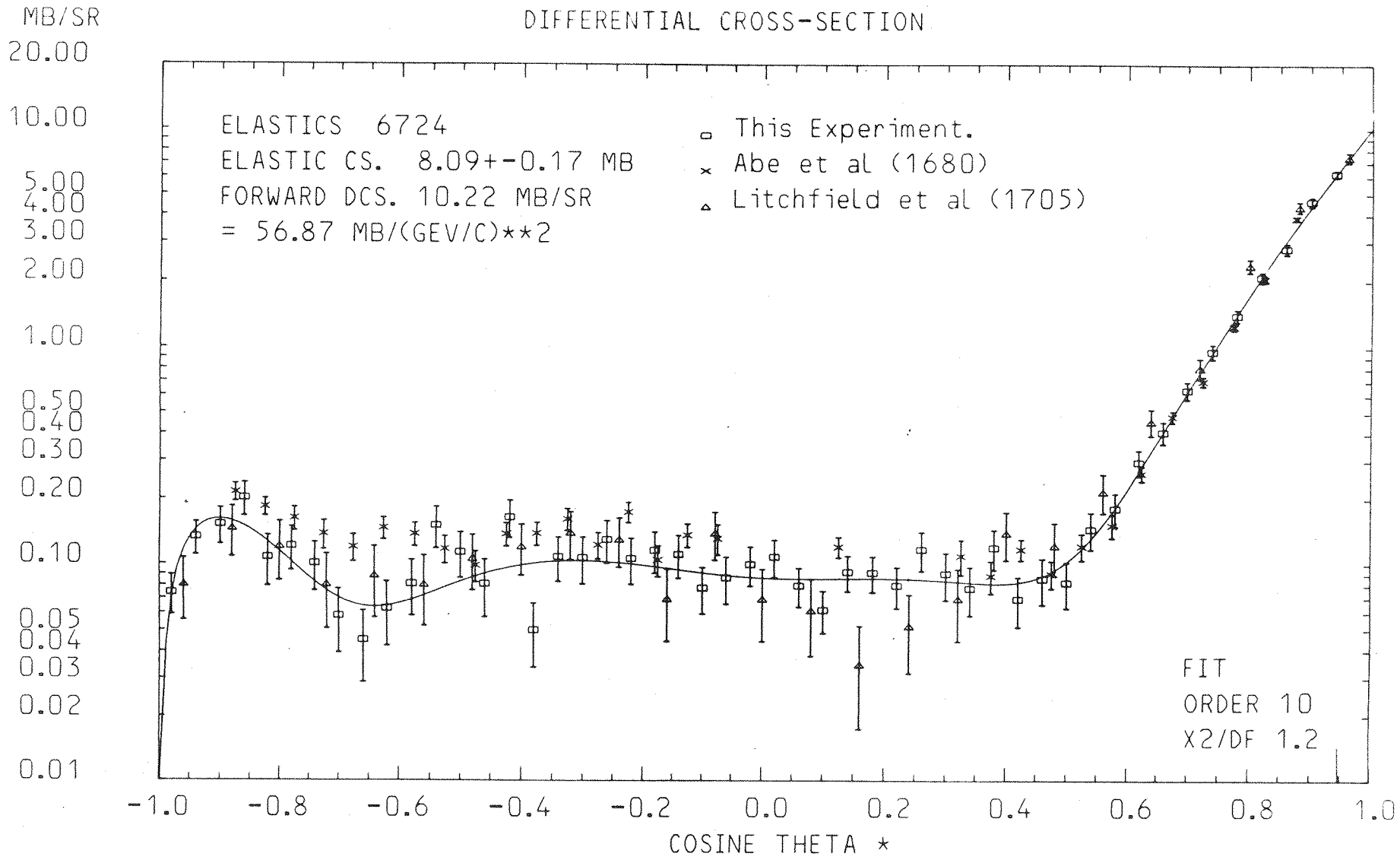

FIG 8.16 1.683 GEV/C. K- P ELASTIC K15A.

kaon pathlength at selected momenta. Thus agreement with this experiment gives confidence in our results at the higher momenta.

At 1433 MeV/c there is now good agreement with Abe et. al., whereas at 1683 MeV/c the data points from the present experiment are consistently low over the central region of the angular range. However the forward diffraction peaks are compatible and this produces close agreement between the elastic cross sections (Table8.2). Again the experiment of Abe et. al. did not have an external check on the normalisation; their results were renormalised by extrapolating the efficiency of their detectors to 100%.

A further check on the data was made by comparing the forward point with predictions from forward dispersion relations[33] (F.D.R.). In addition to extrapolation of the Legendre fit, a least squares exponential fit was made to the forward diffraction peak:

$$\frac{d\sigma}{d\Omega} = A \exp(Bt) \qquad \text{for } t>-0.36 \text{ (GeV/c)}^2$$

where t is the momentum transfer.

A comparison between the fitted and predicted values is made in Table8.3. Agreement with the

exponential fit is significantly improved by the renormalisation factors, whereas results from the Legendre fit are inconclusive. However the Legendre fit is less reliable since the forward point is influenced by the differential cross section over the complete angular region.

Table 8.3 Comparison between the forward point and forward dispersion relations, in units of mb/(GeV/c)^2.

Momentum MeV/c	Exponential Fit $\frac{d\sigma}{d\Omega}(\theta)$	Exponential Fit $\frac{d\sigma}{d\Omega}(\theta)\times R$	Legendre Fit $\frac{d\sigma}{d\Omega}(\theta)$	Legendre Fit $\frac{d\sigma}{d\Omega}(\theta)\times R$	F.D.R.
1212	54.42	63.06	66.71	77.30	62.7
1283	44.67	48.72	41.49	45.24	52.0
1433	38.04	44.54	50.28	58.87	52.5
1633	54.71	58.34	52.22	55.69	59.9
1683	58.18	62.36	53.06	56.88	58.8

In conclusion, the combination of high statistics and wide angular coverage for this experiment represents a significant improvement on the existing data. To date effort has been concentrated on resolving a discrepancy in the normalisation. It is hoped that this discrepancy will be resolved before completion of the analysis. Analysis of all data will enable this experiment to extend the precise measurements of Conforto et. al. to

1933 MeV/c in approximately 50 MeV/c intervals thus making a significant contribution to the existing $K^- p$ elastic scattering results.

Addendum

The normalisation discrepancy was subsequently reduced by modifications to the track-finding algorithm, as indicated on page 102. At the time of writing only a small data sample at three of the momenta presented in this thesis have been reanalysed. The renormalisation factors corresponding to those given in Table 8.1 are :

MOMENTUM (MeV/c)	R
1212	1.04 ± 0.03
1433	1.05 ± 0.03
1633	0.98 ± 0.03

Appendix 1

The Differential Cross Section

For elastic scattering into a small solid angle $d\Omega$ at an angle θ^* with respect to the incident beam in the centre of mass, the elastic differential cross section is defined by:

$$\sigma(\theta^*) = \frac{d\sigma(\theta^*)}{d\Omega}$$

The beam counters measure a flux of kaons, N_c, as being potential candidates for elastic scattering in the liquid hydrogen target. The total number of these, dN_s, scattered into $d\Omega$ at an angle θ^* is related to the differential cross section by:

$$dN_s(\theta^*) = N_c \rho \sigma(\theta^*) d\Omega \, dl$$

where ρ is the density of scattering centres (protons) per unit volume and dl is an element of target length from l to $l+dl$ where the scatters originate.

The total number of events observed by the experiment, dN_{obs}, is a function of the detection efficiency of the apparatus, which varies with the azimuth ϕ. If $P(\theta^*,\phi,l)$ represents the probability that events defined by θ^*,ϕ and l are detected then:

$$dN_{obs}(\theta^*,\phi,l) = dN_s(\theta^*) \, P(\theta^*,\phi,l)$$

The total number of events counted as a function of θ^* only is found by integrating this expression over ϕ and l. Thus:

$$N_{obs}(\theta^*) = N_c \rho \sigma(\theta^*) \int_{l_1}^{l_2} \int_0^{2\pi} P(\theta, \phi, l) \, d\phi \, dl \, d\cos\theta^*$$

where $d\Omega = d\phi \, d\cos\theta^*$ has been used

l_1 and l_2 define the limits of the liquid hydrogen vessel.

The acceptance of the detectors is therefore given by an expression of the form:

$$A(\theta^*) = \int_{l_1}^{l_2} \int_0^{2\pi} \frac{P(\theta^*, \phi, l)}{2\pi L_t} \, d\phi \, dl$$

where $L_t = l_1 - l_2$, the length of the liquid hydrogen vessel. A has been normalised to lie between 0 and 1.

In terms of A the differential cross section becomes:

$$\sigma(\theta^*) = \frac{d\sigma}{d\Omega}(\theta^*) = \frac{N_{obs}(\theta^*)}{N_c \rho \, 2\pi \, L_t \, A(\theta^*) \, d\cos\theta^*} \quad \text{----A1.1}$$

Since the results are presented in histogram form this equation must be integrated over each bin:

$$\sigma_i = \int_{bin\,i} \sigma(\theta^*) \, d\cos\theta^*$$

Integration of the acceptance over each bin leads to a series of weighting factors:

$$W_i = \int_{bin\,i} A(\theta^*) \, d\cos\theta^*$$

$$\text{or} \quad W_i = \overline{A}_i(\theta^*)\ \Delta\cos\theta^*$$

where $\overline{A}_i(\theta^*)$ is the mean acceptance over the bin i, which is of width $\Delta\cos\theta^*$.

Appendix 2

Efficiency of the DISC Cerenkov

Since kaons were not completely separated by the beam elements the efficiency of the DISC was deduced from its efficiency for identifying protons.

Each photomultiplier had only a certain probability of detecting the Cerenkov light because of the focusing properties of the detector and the quantum efficiency of the photocathode. The inefficiencies for each tube were shown to be uncorrelated by measuring rates rates individually and in coincidence.

The number of photoelectrons produced in a phototube by each light shower follows the Poisson distribution. If n is the average number of photoelectrons produced then the probability of producing r photoelectrons is given by:

$$\frac{n^r}{r!} \exp(-n)$$

However the discriminator threshold is normally adjusted such that only one photoelectron is required to produce a trigger. The phototube inefficiency can therefore be determined by setting r=0 in the above equation. Hence the efficiency per tube is given by:

$$1 - \exp(-n)$$

and for a nine-fold coincidence by:

$$(1 - \exp(-n))^9 \quad \ldots\ldots\ldots \text{A2.1}$$

For protons the efficiency was measured to be 56.6%, which corresponds to 2.8 photoelectrons.

The intensity of Cerenkov radiation is proportional to $\sin^2$(Cerenkov angle). Hence the number of photons produced by kaons at the same momentum was determined by scaling the number of photoelectrons with the factor $\sin^2(\theta_{kaon})/\sin^2(\theta_{proton})$.

Equation A2.1 then gives a kaon detection efficiency of 63.6%.

Appendix 3

The Range Measurement

Protons traversing an absorber suffer energy degredation and eventually stop providing the absorber is sufficiently long. Their initial momentum can be accurately determined from their total path length (range) in the absorber using the theory of stopping power.[34] Comparison with measurements made by the proportional chambers were expected to show up any systematic errors in the beam momentum determination.

The absorber used was high purity copper, machined into blocks (10cm.x10cm. in cross section) such that the total thickness could be varied from 0 to 190mm in 0.5mm intervals. Proton transmission was measured by two specially prepared scintillation counters, R1 (1cm.x1cm.) and R2 (10cm.x10cm.). R1 was positioned to select protons incident on the centre of the entrance face of the absorber, whereas R2 was placed after the absorber and covered any dispersion of the protons due to multiple scattering in the copper.

The hydrogen target was moved to one side and the arrangement of absorbers and counters supported at beam height behind D2 (Fig.A3.1a). A 1 Gev/c proton beam was selected, with the DISC counter removed from the beamline. A preliminary measurement was made to obtain

the transmission, defined by D1.D2.R1.R2./D1.D2.R1, as a function of absorber thickness (Fig.A3.1b). Three discernable regions were apparent from the results, namely:-

(a)A steady decrease in the transmission attributed to nuclear absorption.

(b)A sharp decrease in transmission due to "stopping" in the absorber.

(c)A low background not attributed to the protons but associated with contamination of the proton beam.

Further measurements were made to record proportional chamber data with a constant absorber thickness, selected from region (b) of the transmision curve. D1. D2. R1 was used as a trigger and signals from R2 were recorded to identify those protons penetrating the copper. Momenta were determined from the track fitting routines which were slightly modified, to take advantage of the absence of the DISC, by combining sections 2 and 3. This approach enabled a measurement of the transmission as a function of momentum.

The above procedure was repeated for three absorber thicknesses and the results are presented in Figure A3.2. The differentiated curves approximate well to gaussians, whose width is in agreement with that expected from a combination of range straggling and

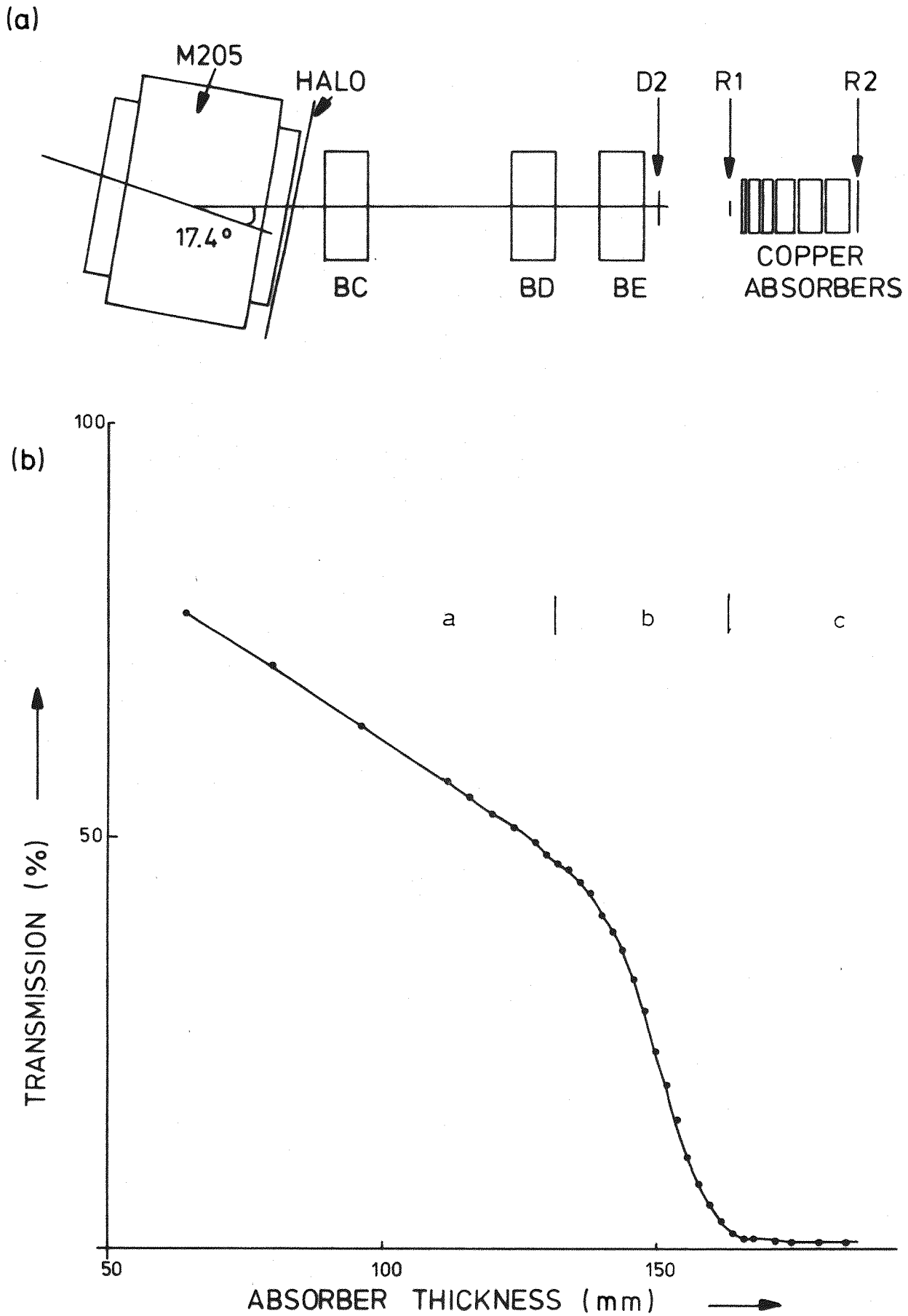

FIG. A3.1 (a) ARRANGEMENT OF ABSORBERS
(b) TYPICAL RANGE CURVE

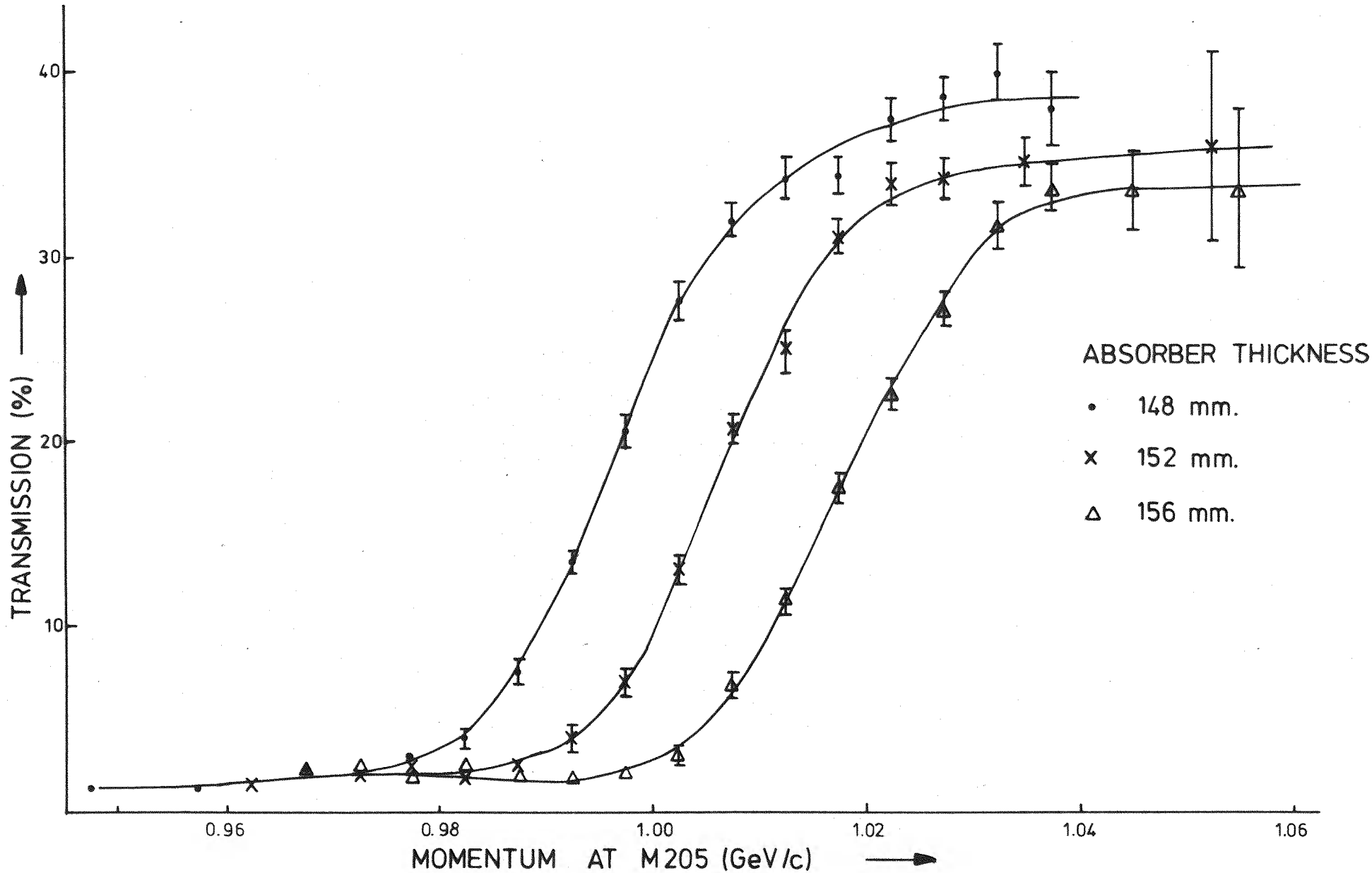

FIG. A3.2 PROTON TRANSMISSION IN COPPER ABSORBER

imprecision in the momentum measurement. The momentum corresponding to a mean range equal to the absorber thickness was obtained as the momentum at which half the protons were transmitted, having first subtracted the low background and renormalised for the nuclear absorption. These values were corrected for the energy loss of the protons between M205 and D2.

Before the results could be compared with theory a correction had to be made for multiple scattering, which makes the path length in the absorber greater than the absorber thickness. This correction amounts to 0.5% in the range for 1 Gev/c protons.[35]

The final results (TableA3.1) showed the two methods to be consistent within the estimated errors. It was concluded that the systematic error in the momentum determination of Equation 6.1 was less than 0.5%.

Table A3.1 Results of the Proton Range Measurement

Copper Thickness	Momentum From Range-Energy Relations[34]	Momentum From Transmission Curves
148mm.	989 ± 4 MeV/c	991 ± 2 MeV/c
152mm.	999 ± 4 MeV/c	1001 ± 2 MeV/c
156mm.	1010 ± 4 MeV/c	1013 ± 2 MeV/c

Appendix 4

Preliminary differential cross sections are presented in graphical form at five momenta: 1212,1283,1433,1633,1683 (MeV/c). The solid curve represents a Legendre Polynomial fit to the data points. The elastic cross section and forward point were determined from the fit, as discussed in section 8.1.

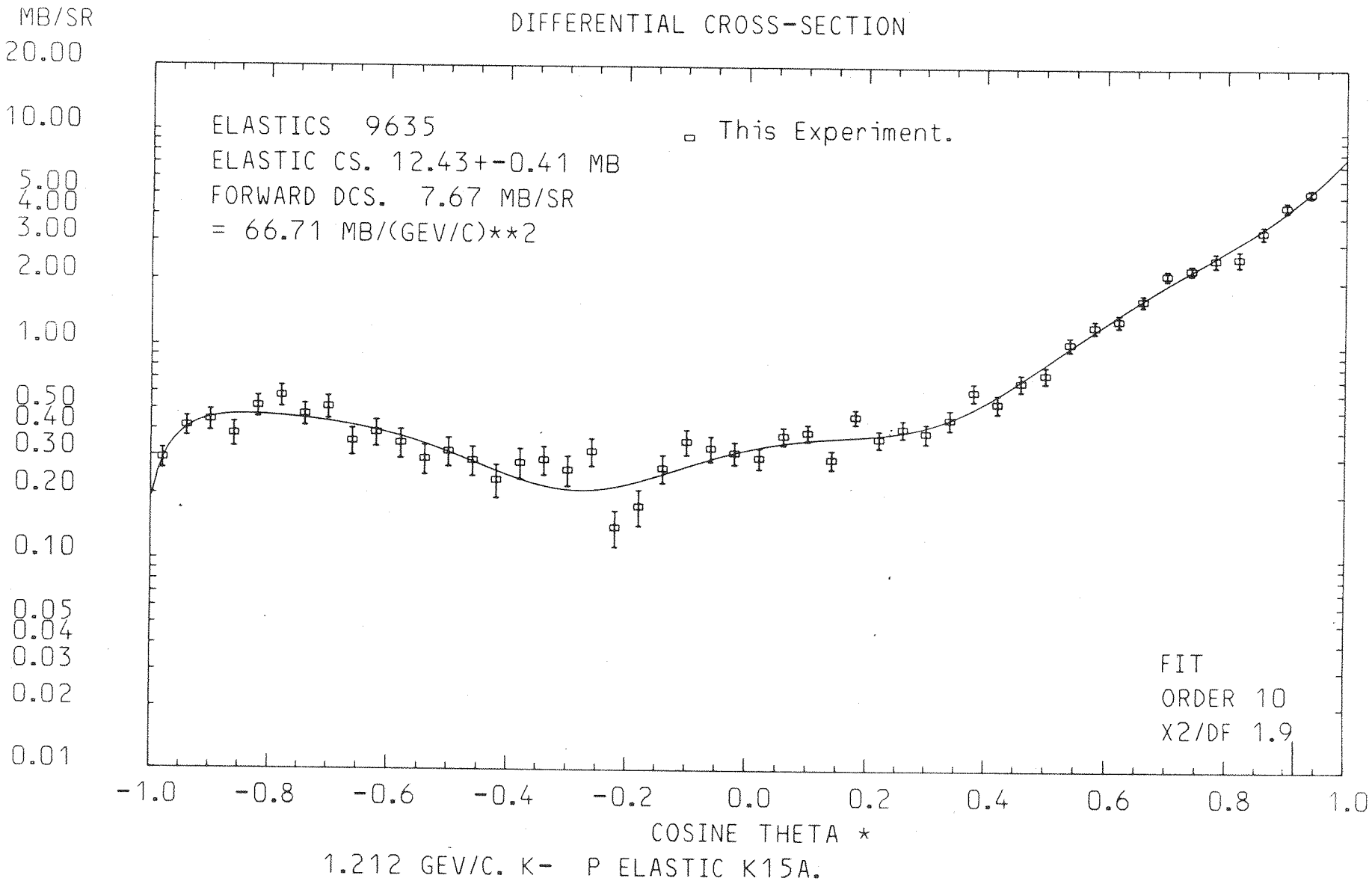
MB/SR
DIFFERENTIAL CROSS-SECTION
20.00
10.00
5.00
4.00
3.00
2.00
1.00
0.50
0.40
0.30
0.20
0.10
0.05
0.04
0.03
0.02
0.01
ELASTICS 9635
ELASTIC CS. 12.43+-0.41 MB
FORWARD DCS. 7.67 MB/SR
= 66.71 MB/(GEV/C)**2
This Experiment.
FIT
ORDER 10
X2/DF 1.9
-1.0
-0.8
-0.6
-0.4
-0.2
0.0
0.2
0.4
0.6
0.8
1.0
COSINE THETA *
1.212 GEV/C. K- P ELASTIC K15A.

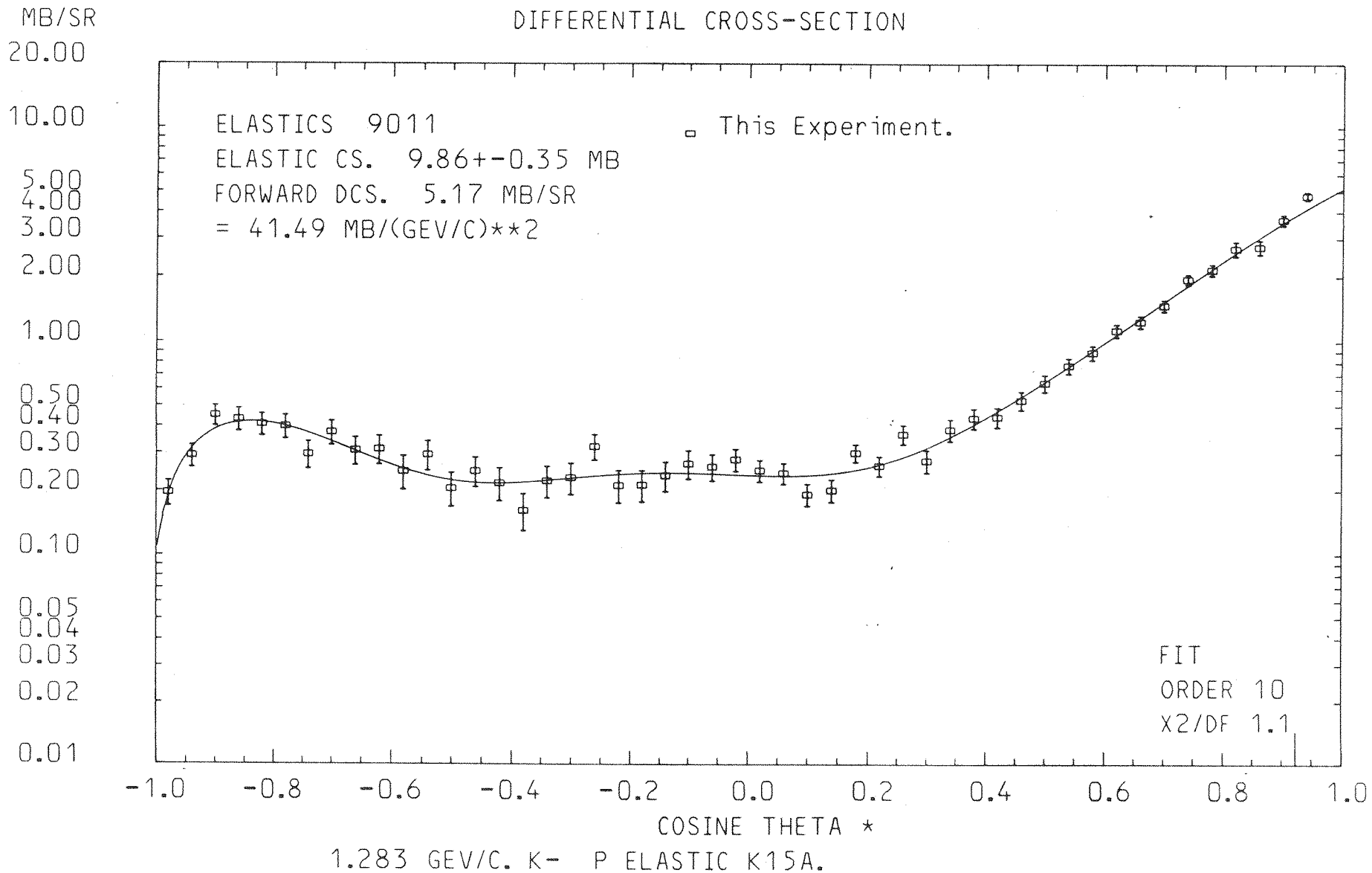
MB/SR
DIFFERENTIAL CROSS-SECTION
20.00
10.00
5.00
4.00
3.00
2.00
1.00
0.50
0.40
0.30
0.20
0.10
0.05
0.04
0.03
0.02
0.01
ELASTICS 9011
ELASTIC CS. 9.86+-0.35 MB
FORWARD DCS. 5.17 MB/SR
= 41.49 MB/(GEV/C)**2
This Experiment.
FIT
ORDER 10
X2/DF 1.1
-1.0
-0.8
-0.6
-0.4
-0.2
0.0
0.2
0.4
0.6
0.8
1.0
COSINE THETA *
1.283 GEV/C. K- P ELASTIC K15A.

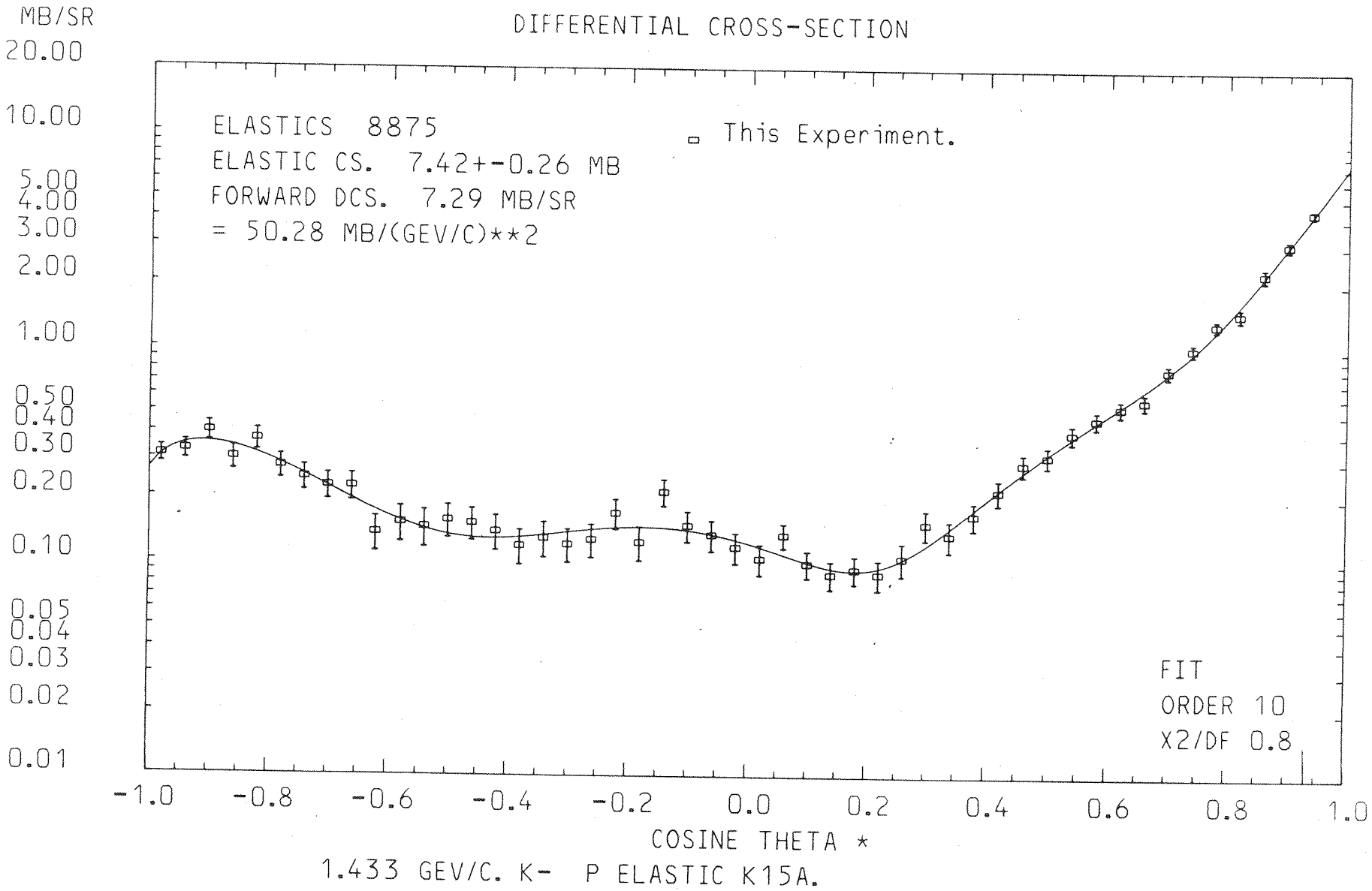
MB/SR
DIFFERENTIAL CROSS-SECTION
20.00
10.00
5.00
4.00
3.00
2.00
1.00
0.50
0.40
0.30
0.20
0.10
0.05
0.04
0.03
0.02
0.01
ELASTICS 8875
ELASTIC CS. 7.42+-0.26 MB
FORWARD DCS. 7.29 MB/SR
= 50.28 MB/(GEV/C)**2
This Experiment.
FIT
ORDER 10
X2/DF 0.8
-1.0
-0.8
-0.6
-0.4
-0.2
0.0
0.2
0.4
0.6
0.8
1.0
COSINE THETA *
1.433 GEV/C. K- P ELASTIC K15A.

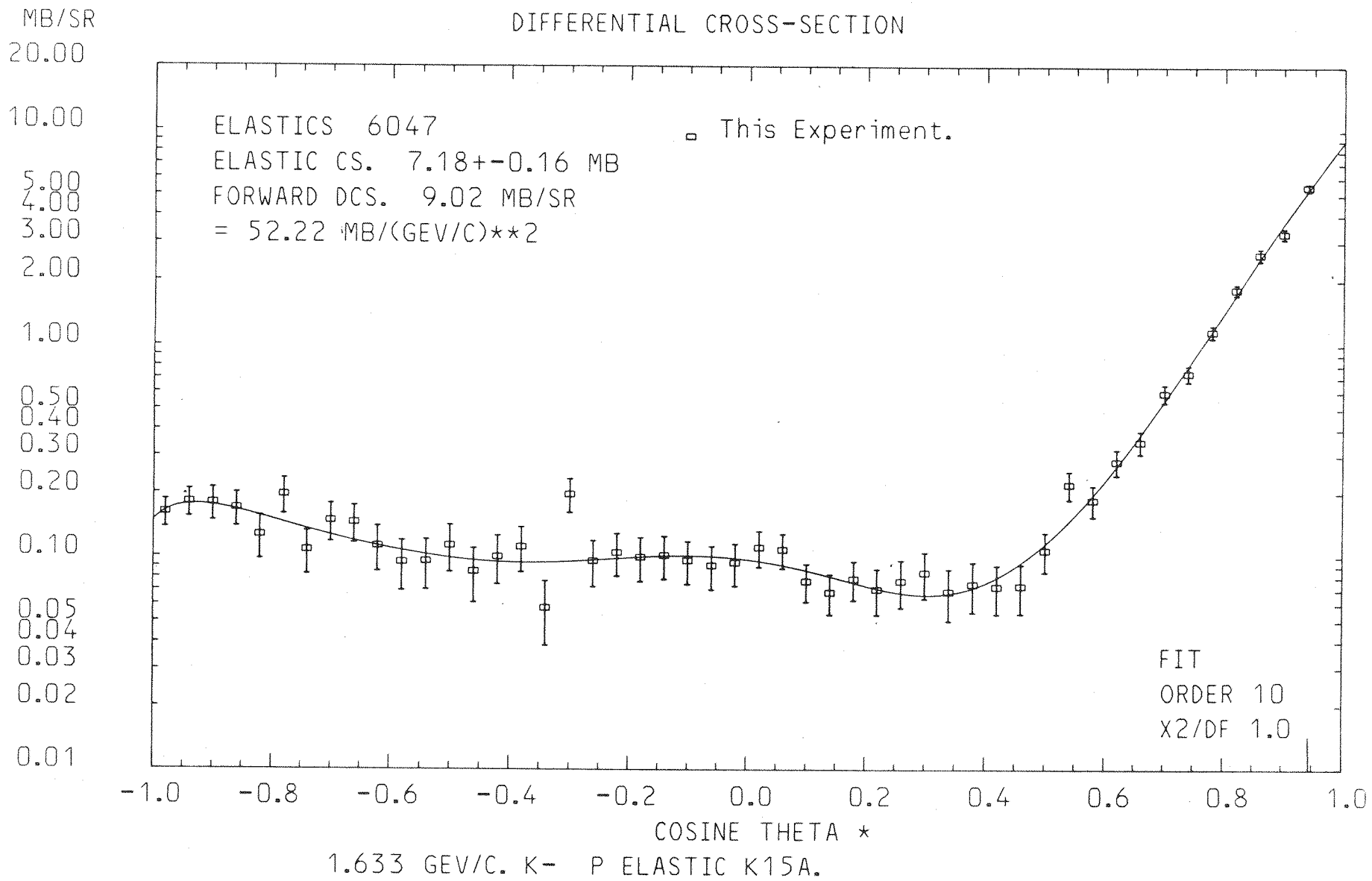
MB/SR
DIFFERENTIAL CROSS-SECTION
20.00
10.00
5.00
4.00
3.00
2.00
1.00
0.50
0.40
0.30
0.20
0.10
0.05
0.04
0.03
0.02
0.01
ELASTICS 6047
ELASTIC CS. 7.18+-0.16 MB
FORWARD DCS. 9.02 MB/SR
= 52.22 MB/(GEV/C)**2
This Experiment.
FIT
ORDER 10
X2/DF 1.0
-1.0
-0.8
-0.6
-0.4
-0.2
0.0
0.2
0.4
0.6
0.8
1.0
COSINE THETA *
1.633 GEV/C. K- P ELASTIC K15A.

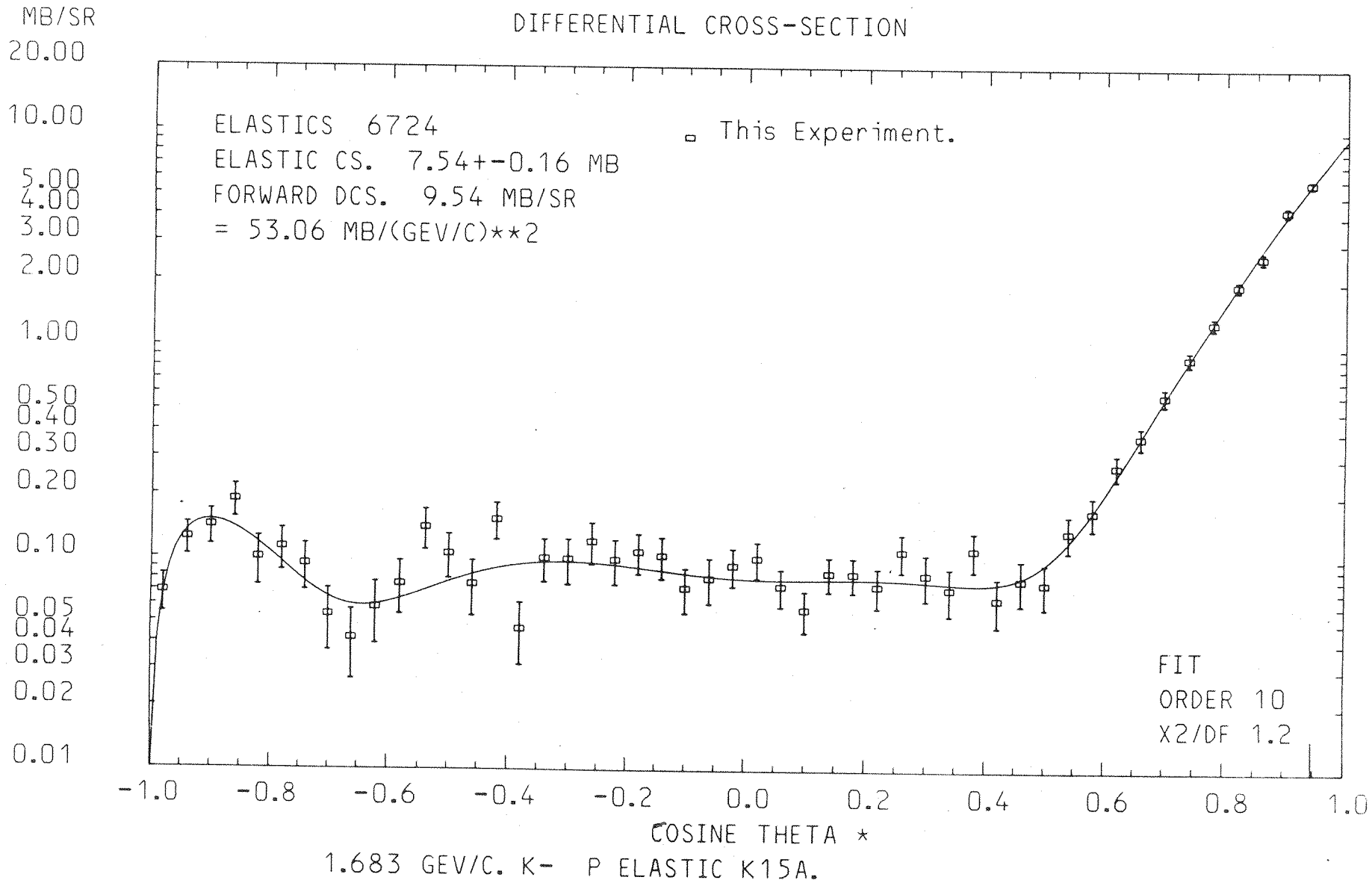
MB/SR
DIFFERENTIAL CROSS-SECTION
20.00
10.00
5.00
4.00
3.00
2.00
1.00
0.50
0.40
0.30
0.20
0.10
0.05
0.04
0.03
0.02
0.01
ELASTICS 6724
ELASTIC CS. 7.54+-0.16 MB
FORWARD DCS. 9.54 MB/SR
= 53.06 MB/(GEV/C)**2
This Experiment.
FIT
ORDER 10
X2/DF 1.2
-1.0
-0.8
-0.6
-0.4
-0.2
0.0
0.2
0.4
0.6
0.8
1.0
COSINE THETA *
1.683 GEV/C. K- P ELASTIC K15A.

References

The following abbreviations have been used when referring to journals.

Phys. Rev.	Physical Review
N.P.	Nuclear Physics
P.R.L.	Physical Review Letters
N.C.	Nuovo Cimento
A.R.N.S.	Annual Review of Nuclear Science
N.I.M.	Nuclear Instruments and Methods
J.E.T.P.	Soviet Physics : Journal of Experimental and Theoretical Physics

1 D.V.Bugg et.al. Phys.Rev. 168 Number 5 1466 (1968)

R.L.Cool et.al. Phys. Rev. 1D Number 7 1917 (1970)

2 R.Armenteros et.al. N.P. B21 15 (1970)

3 R.Armenteros et.al. N.P. B8 233 (1968)

B.Conforto et.al. N.P. B8 265 (1968)

B.Conforto et.al. N.P. B34 41 (1971)

4 C.Daum et.al. N.P. B6 273 (1968)

S.Andersson-Almehed et.al. N.P. B21 515 (1970)

M.G.Albrow et.al. N.P. B29 413 (1971)

5 J.K.Kim P.R.L. 27 356 (1971)

W.Langbein et.al. N.P. B47 477 (1972)

A.T.Lea et.al. N.P. B56 77 (1973)

6 P.J.Litchfield et.al. N.P. B30 125 (1971)

7 J.Griselin et.al. N.P. B93 189 (1975)

8 R.J.Hemingway et.al. N.P. B91 12 (1975)

9 C.J.Adams et.al. N.P. B96 54 (1975)

10 C.J.S.Damerell et.al. N.P. B129 397 (1977)

11 P.C.Barber et.al. N.P. B92 391 (1975)

12 P.C.Barber et.al. N.P. B61 125 (1973)

13 K.Abe et.al. Phys. Rev. D12 12 (1975)

14 B.Conforto et.al. N.P. B105 189 (1976)

15 L.Bertanza et.al. N.P. B110 1 (1976)

16 G.P.Gopal et.al. N.P. B119 362 (1977)

17 A.De.Bellefon et.al. N.C. 42A 403 (1977)

18 Declais et.al. CERN Report 77-16 (1977)

19 P.J.Litchfield et.al. Paper presented to the
Topical Conference on Baryon Resonances
Oxford, July 1976

20 J.D.Davies et.al. N.C. 54 608 (1968)

21 F.Atchison NIMROD(PD) 70-18 June 1970
Rutherford Laboratory Report

22 G.Charpak A.R.N.S. 195 (1970)

23 G.Charpak N.I.M. 80 13 (1970)

24 Rose et. al. Phys. Rev. 59 850 (1941)

25 T.Trippe CERN Report NP 69-18 (1969)

26 E.Quercigh N.I.M. 41 355 (1966)

27 B.Friend N.I.M. 65 311 (1968)

28 H.I.Pizer N.I.M. 93 249 (1971)

29 J.A.G. Morris Ph.D. Thesis University of Bristol (1978)

D.J.Bardsley Ph.D. Thesis University of Bristol (1978)

30 F.James CERN Report 68-15 (1968)

31 J.D.Jackson Classical Electrodynamics
John Wiley & Sons,New York,1975

32 H.Bichsel
Passage of Charged Particles Through Matter,
American Institute of Physics Handbook
McGraw-Hill (1972)

33 O.Dumbrajs Preprint Number HU-TFT-78-15
Research Institute for Theoretical Physics,
University of Helsinki

34 W.H.Barkas et.al.

Tables of Energy Losses and Ranges of Heavy Charged Particles N.A.S.A. Report SP-3013 (1964)

35 V.P.Zrelov et.al. J.E.T.P. 36 Number 2 (1959)

Acknowledgements

I would like to give my sincere thanks to all members of the collaboration for their efforts in bringing the experiment to a successful conclusion. Those people involved were:

D.J.Bardsley, R.A.Burnham, R.S.Gilmore,F.A.Lovett, I.C.McArthur, J.Malos, J.P.Melot, V.J.Smith, R.J.Tapper, (Bristol University)

D.I.Giddings, J.A.G.Morris, P.H.Sharp, P.D.Wroath (Rutherford Laboratory)

G.A.Beck, S.G.F.Frank and myself (Southampton University).

I am particularly grateful to my supervisor, Dr. S.G.F.Frank, for his guidance and encouragement throughout my research studentship. In addition I am indebted to Dr. P.H.Sharp for explaining to me many aspects of the experiment and to Dr. G.A.Beck for many illuminating discussions concerning the analysis of the experiment.

I would also like to thank the Physics Department of the University of Southampton for the facilities made available to me during the period of this research and to the NIMROD operating crew, the computer staff and

many other technical support staff at the Rutherford Laboratory who all contributed to the experiment.

Above all, I wish to thank my wife for her patience and encouragement during the last four years and for her efforts in the preparation of this manuscript.